UNIVERSITY OF CALIFORNIA SAN DIEGO

Individually Addressable Nanowire Arrays for Probing Neuronal Culture and Tissue

A dissertation submitted in partial satisfaction of the requirements for the degree

Doctor of Philosophy

in

Electrical Engineering (Nanoscale Devices and Systems)

by

Ren Liu

Committee in charge:

Professor Shadi A. Dayeh, Chair
Professor Yu-hwa Lo
Professor Ying Shirley Meng
Professor Yuan Taur
Professor Sheng Xu

2019

The Dissertation of Ren Liu is approved, and it is acceptable in quality and form for publication on microfilm and electronically:

_____

_____

_____

_____

_____

Chair

University of California San Diego

2019

DEDICATION

To my parents

TABLE OF CONTENTS

LIST OF FIGURES

LIST OF TABLES

ACKNOWLEDGEMENTS

The five and half years of my Ph.D. study have been the most significant experience in my life. Without the tremendous support and help from many people around me, it would have been impossible to finish my Ph.D. research excellently. I would like to express my sincere gratitude and appreciation to all these great people.

First of all, I would like to express my greatest gratitude to my advisor Prof. Shadi A. Dayeh for his enormous amount of support, tremendous guidance, and continuous encouragement over all of my Ph.D. researches. I cannot believe how many difficulties we have met during my Ph.D. researches, from experiment design, devices fabrication, cell recording, nanowire-neuron interface characterization, failure analysis, solution development, and all other aspects of my research. However, with Prof. Dayeh's abundant guidance and encouragement, we have solved them all one by one. Prof. Dayeh not only contributed a lot to my projects, he also contributed exceptionally to all the research projects of all our group members. With him being such a distinguished role model, our hardworking led to many exciting achievements, and the pressures transformed to abundant awards and splendid honors. His fulfilling research plan, rigorous research attitude and magnificent research goals influence me a lot and shape me to be an exceptional researcher. No words can express my greatest appreciation and gratitude to Prof. Dayeh. It is my greatest honor to have him as my advisor.

I am highly grateful to my thesis committee members Prof. Yu-hwa Lo, Prof. Ying Shirley Meng, Prof. Yuan Taur and Prof. Sheng Xu. Thanks so much to Prof. Lo for teaching me the course "Solid State Electronics" and Prof. Taur for teaching me the course "Solid-State Electronic Devices", which helped me to successfully pass the preliminary exam. Prof. Lo's course of "Biophysics" helped me a lot on my research by developing my understanding of the mechanism

of how excitable cells work. I really appreciate the precious feedbacks from Prof. Meng and Prof. Xu during my qualifying exam and final defense; their valuable suggestions helped the completion of this thesis. I would like to express my greatest gratitude to Prof. Xu for his tremendous support for my postdoc applications, which helped me to get the postdoc offer from Harvard University! Thanks so much all my committee members for their great efforts on my Ph.D. study over the past five and half years. I would like to express my special thanks to Prof. S. S. Lau for many valuable inputs and discussions during my Ph.D. research. I would also like to express my especial thanks to Dr. Jen Martinez for her great help on the application of UC-National Laboratory In-Residence Graduate Fellowship.

Moreover, I have performed my research for four years at the Center for Integrated Nanotechnologies (CINT) under the CINT user proposals, which provided me the world-class research facilities, such as FEI transmission electron microscopes, Titan environmental transmission electron microscope, JEOL e-beam writer, etc. I'm very grateful to Dr. John Nogan for the training and support with the cleanroom facilities, discussions on all the fabrication process which eventually led to great results. I very appreciate Dr. Katie Jungjohann so much for continuous support on my research, discussions about TEM and my postdoc applications, and helping me to get the postdoc offer from Harvard University. I also would like to express many thanks to Tony James for his support on JEOL e-beam writer, to Doug Pete for his support on scanning electron microscope and focused ion beam. I'm very grateful to Denise Webb for sharing experiences of cleanroom and life. Many special thanks to all the staff members from CINT: Dr. Sean Hearne, Dr. Heather D. Brown, Dr. Bill Mook, Dr. Jinkyoung Yoo, Dr. Nan Li, Corey J. Parsons, Will Ross and Joseph Lucero. All your stupendous efforts and contributions make CINT such an extraordinary place for doing world-class research.

I am so delighted to have many excellent labmates at the Integrated Electronics and Biointerfaces Laboratory (IEBL). Dr. Renjie Chen and I worked together at CINT for three years. He gave me lots of training and guidance at the first year of my Ph.D. research and provided great support and help on my research and life at CINT. It is my fortune to have him as a labmate and a friend. I also would like to express many thanks to Yun Goo Ro and Dr. Atsunori Tanaka for their help on many devices for nanowire etching and packaging, to Sang Heon for his help on the cell recording, and to Ahmed Youssef and Andrew Bourhis for helping with modeling. Because of my projects being super tough, especially for the complicated the fabrication process and long-term cell culture and recording processes, I have traveled between UCSD and CINT back and forth many times to finish batches of devices' fabrication and recording. Renjie and Yun Goo often sent me to airport and picked up me from airport because of my research at both UCSD and CINT. I really appreciate it so much. I am also grateful for Woojin Choi for providing me accommodation for my short trip for research at UCSD once I was living at CINT. Without all of their help and support with my research, I would not have been able to achieve my PhD. Moreover, other group members, Dr. Youngbin Tchoe, Dr. Mehran Ganji, Lorraine Hossain, Po Chun Chen, Jihwan Lee, Samantha Russman, Ritwik Vastyayan, Keundong Lee, Dr. Hongseok Oh, Dr. Namseok Park, Dr. Supanee Sukrittanon have given me great support both in experiment and daily life. I sincerely bless all the IEBLers to achieve success in their graduate studies and careers.

Outside of IEBL, I have a lot of brilliant collaborators. It is so great experience to work together with them. Dr. Sandy Hinckley and Deborah Pre helped us with neuron culture and recording. I really appreciate their professional knowledge and biological experiments skills in neuroscience, which helped us achieve our first nanowire-neuron publication in Nano Letters. Thanks Dr. Gaelle Robin for always discussing with me and giving me a lot of feedback, which

helped us to get the exciting achievement on stable recording with neuronal spike trains of action potentials. I am also grateful to Dr. Agnieszka D'Antonio-Chronowska for her great help on the cardiomyocyte culture, where we recorded pacemaker action potential of cardiac tissue. I really appreciate Dr. Jun Wang's enormous efforts on the project of the integration of CMOS chip and nanowire and I admire his knowledge in CMOS design and his academic ambitions. Without their tremendous contribution on the collaborative projects, we would not have this thesis and my Ph.D. achievements. I appreciate their support very deeply in my heart.

It was such a long and challenging academic road. However, it is my great fortune to have so many teachers and friends share their experiences and encouragement to me. My master supervisors Prof. Zhimin Liao and Prof. Dapeng Yu always act as my role models and continuously encourage me to be an excellent researcher. I really appreciate that Prof. Liao provided a lot of suggestions and support on my postdoc applications. Thanks Dr. Xuewen Fu and Dr. Yaqing Bie for sharing their research experience with me and their support of my research goals. I also would like to express my gratitude to Prof. Qing Gu from the University of Texas at Dallas (UTD). We have worked together at UCSD cleanroom at the first year of my Ph.D., and I was witnessing her outstanding achievements and journey from a UCSD student to an extraordinary professor at UTD. I am so delighted to hear from her about each of her accomplishment from research and life. Thanks so much for the encouragement to insist on the academic dream from Dr. Chun-Chieh Chang. I am appreciative for Dr. Jun Wang's tremendous support to my research and my research dream. I am so grateful to have all of them in my life and act as light on the road to academic success.

I also would like to express thanks to many friends at UCSD or CINT for their friendship and support for my research and daily life, including Jie Chen, Wenlong Yu, Erdong Song, Sheng

Liu, Enzhi Xu, Peter Liu, Yuanmu Yang, Miller Li, Zhu Wang and Rong Zhong. I would like to acknowledge Kathy and Hud for they gave me the warmest place to live in Albuquerque, treated me as a daughter and acted as my parents abroad.

Part of my work was done at UCSD cleanroom of Nano3. Thanks so much to Nano3 staffs for maintaining the cleanroom in great and being very flexible upon my request, especially when I travelled back from CINT for short and compact experiment schedule, Larry Grissom and Dr. Xuekun Lu always helped me arrange the equipment time, which is so helpful and I appreciate them so much for it. I would like to acknowledge many other Nano3 staffs members: Dr. Bernd Fruhberger, Dr. Ryan Anderson, Dr. Jeff Wu, Sean Parks, Dr. Maribel Montero and all others. I would like to also thank ECE Department staffs, Cheryle Wills, Cecilia Palacios, Chay Mendoza, Mo Latimer and Julie Mortiz. Without their assistance, I would not have been able to conduct our research in the convenient way.

I would like also to acknowledge financial support from the UC-National Laboratory In-Residence Graduate Fellow program for two years' fellowship during 2017-2019, ECE department especially for one year's department fellowship during 2014-2015 and teaching assistant opportunity of "Linear Electronic Systems" from Prof. Daniel Sievenpiper in 2019 fall quarter, and all the research assistant projects from Prof. Shadi Dayeh's funding by National Science Foundation.

Last but not the least, I would like to express my deepest appreciation and thankfulness to my parents, Wenjie Liu and Xueqin Chen, my brother Song Liu, and to my grandparents, Jiuhua Gao, late Yonglun Chen, late Shijun Liu and late Jilan Tang. I have lost my grandfather late Shijun Liu after I came to US and I am so sorry that I could not attend his funeral. However, I am sure they keep watching me from heaven now and in the future. I remembered my grandmother late

Jilan Tang often told me she always prayed for me after I went to school out of town. I remembered my grandfather late Yonglun Chen always encouraged me to be a brave girl. Their profound love, endless support, unconditional trust, warmest care, enormous sacrifice, and continuous encouragement have enabled me to sustain the pressures and challenges in the last five and half years of my Ph.D. and have made me persevere and strive in the most difficult situations through my Ph.D. program.

The list is not thorough and I would like to thank all other people who have helped and encouraged me, but are not mentioned above.

Part of chapter 1 is currently being prepared for submission for publication as an invited review paper. Y. Tchoe, R. Liu, A. M. Bourhis, J. Lee, and S. A. Dayeh, “Considerations and Recent Advances in Nanowire-Neuron Interfaces”. The dissertation author is author of this paper.

Chapter 2, in full, is a reprint of material as it appears in the following publication: R. Liu, R. Chen, A. T. Elthakeb, S. H. Lee, S. Hinckley, M. L. Khraiche, J. Scott, D. Pre, Y. Hwang, A. Tanaka, Y. G. Ro, A. K. Matsushita, X. Dai, C. Soci, S. Biesmans, A. James, J. Nogan, K. L. Jungjohann, D. V. Pete, D. B. Webb, Y. Zou, A. G. Bang and S. A. Dayeh, “High Density Individually Addressable Nanowire Arrays Record Intracellular Activity from Primary Rodent and Human Stem Cell Derived Neurons” Nano Lett. 17 (5), 2757-2764 (2017). The dissertation author is the first author of this paper.

Most of chapter 3 is currently being prepared for submission for publication. R. Liu, A. Bourhis, G. Robin, A. D'Antonio-Chronowska, Y. Tchoe, K. Frazer, A. G. Bang and S. A. Dayeh. The dissertation author will be the first author of this paper.

VITA

2011	Bachelor of Science, Physics and Material Science
	Anhui University, China
2014	Master of Science, Condensed Matter Physics
	Peking University, China
2019	Doctor of Philosophy
	Electrical Engineering (Nanoscale Devices and Systems)
	University of California San Diego, US

PUBLICATIONS

Journal papers

1. **R. Liu**, R. Chen, A. T. Elthakeb, S. H. Lee, S. Hinckley, M. L. Khraiche, J. Scott, D. Pre, Y. Hwang, A. Tanaka, Y. G. Ro, A. K. Matsushita, X. Dai, C. Soci, S. Biesmans, A. James, J. Nogan, K. L. Jungjohann, D. V. Pete, D. B. Webb, Y. Zou, A. G. Bang and S. A. Dayeh, "High Density Individually Addressable Nanowire Arrays Record Intracellular Activity from Primary Rodent and Human Stem Cell Derived Neurons" *Nano Lett.* 17 (5), 2757-2764 (2017).

2. S. Sukrittanon, * **R. Liu**, * Y. G. Ro, J. L. Pan, K. L. Jungjohann, C. W. Tu, and S. A. Dayeh "Enhanced conversion efficiency in wide-bandgap GaNP solar cells", *Appl. Phys. Lett.* 107, 153901 (2015). (* Equal Contribution).

3. **R. Liu**, A. Bourhis, G. Robin, A. D'Antonio-Chronowska, Y. Tchoe, D. Pre, K. Frazer, A. G. Bang and S. A. Dayeh, "High Yield, Ultra Sharp Vertically Aligned Nanowire Arrays to Probe Large Neuron Network and Cardiomyocytes Tissue", manuscript in preparation.

4. J. Wang, * **R. Liu**, *Y. Tchoe, D. Pre, A. G. Bang, G. Cauwenberghs, and S. A. Dayeh, "CMOS nanowire array for electrophysiological imaging and stimulation", manuscript in preparation. (* Equal Contribution).

5. J. Wang, **R. Liu**, Y. Tchoe, A. P. Buccino, A. Paul, C. Kim, S. A. Dayeh, and G. Cauwenberghs. "Low-Power 256-Channel Nanowire Electrode-on-Chip Neural Interface for Intracellular Electrophysiology" submitted to *IEEE Custom Integrated Circuits Conference* (2019).

6. M. Ganji, A. C. Paulk, J. C. Yang, N. W. Vahidi, S. H. Lee, **R. Liu**, L. Hossain, E. M. Arneodo, M. Thunemann, M. Shigyo, A. Tanaka, S. B. Ryu, S. W. Lee, M. Marsala, A. Devor, D. R. Cleary, J. R. Martin, H. Oh, V. Gilja, T. Q. Gentner, S. I. Fried, E. Halgren, S. S. Cash, and S. A. Dayeh, "Selective Formation of Porous Pt Nanorods for Highly Electrochemically Efficient Neural Electrode Interfaces", *Nano Lett.* 2019, 19, 9, 6244-6254.

7. W. Choi, R. Chen, C. Levy, A. Tanaka, **R. Liu**, P. M. Asbeck, S. A. Dayeh, "An Intrinsically Linear Transistor for Millimeter-Wave Amplifiers", submitted to *Nat. Electron.*

8. A. Tanaka, W. Choi, R. Chen, **R. Liu**, W. M. Mook, K. L. Jungjohann, P. K. L. Yu, and S. A. Dayeh "Structural and Electrical Characterization of Thick GaN layers on Si, GaN, and Thermally Matched QST Substrates" *J. Appl. Phys*. 125, 082517, 2019

9. Y. G. Ro, R. Chen, **R. Liu**, N. Li, T. Williamson, J. Yoo, S. Sim, R. P. Prasankumar, and S. A. Dayeh "Surface Passivation and Carrier Collection in {110}, {100} and Circular Si Microwire Solar Cells" *Adv. Energy Mater.* 2018, 1802154

10. R. La, **R. Liu**, W. Yao, R. Chen, M. Jansson, J. L Pan, I. A. Buyanova, J. Xiang, S. A Dayeh, C. W. Tu "Self-catalyzed core-shell GaAs/GaNAs nanowires grown on patterned Si (111) by gas-source molecular beam epitaxy" *Appl. Phys. Lett.* 111 (7), 072106 (2017)

11. S. Sukrittanon, **R. Liu**, J. L Pan, K. L Jungjohann, S. A Dayeh, and C. W Tu "Dilute-Nitride GaNP Planar and Core/Shell Microwire Solar Cells" *Compound Semiconductor Week (CSW)* MoP-ISCS-LN-7, 2016

12. S. Sukrittanon, **R. Liu**, M. C. Breeden, J. L. Pan, K. L. Jungjohann, C. W. Tu, and S. A. Dayeh "Radial direct bandgap p-i-n GaNP microwire solar cells with enhanced short circuit current" *J. Appl. Phys.* 120, 055702 (2016)

Patents

1. S. A. Dayeh, **R. Liu**, "High Yield Fabrication of Sharp Vertically Aligned Nanowire Arrays for Intracellular Recordings and Applications Thereof", US Patent, submitted, Application #62669639.

2. S. A. Dayeh, W. Choi, R. Chen, A. Tanaka, **R. Liu**, "Intrinsically Tunable and Ultra-Linear Multi-Fin GaN MOS-HEMT Devices", US Patent, submitted, Application #62579677.

3. S. A. Dayeh, R. Chen, S. Lee, **R. Liu**, Y. Ro, A. Tanaka, Y. Hwang, "ADDRESSABLE VERTICAL NANOWIRE PROBE ARRAYS AND FABRICATION METHODS", **US Patent** App. 16/069,783 (2019).

CONFERENCES

1. "Individually Addressable Nanowire Arrays for Probing Neuronal Networks" (Poster Presentation), WECEDHA, Santa Cruz, CA, USA, **Nov. 2019**

2. "Ultra Sharp Individually Addressable Nanowire Arrays Record Intracellular Activity from Rat Primary Neurons" (Poster Presentation), Research Expo, San Diego, CA, USA, **Apr. 2019**

3. "Ultra-Sharp Individually Addressable Nanowire Arrays Record Intracellular Activity from Rat Primary Neurons" (Poster Presentation), CINT Annual Meeting, Santa Fe, NM, USA, **Sept. 2018**

4. "High-Yield, Ultra Sharp Nanowire Arrays for Intracellular Recordings of Excitable Cells" (Oral Presentation), 60th Electronic Materials Conference, Santa Barbara, CA, USA, **Jun. 2018**

5. "High Density/Ultra Sharp Individually Addressable Nanowire Arrays Record Intracellular Activity from Primary Rodent, hiPSC-Derived Neurons and Cardiomyocytes" (Poster Presentation), Research Expo, San Diego, CA, USA, **Apr. 2018**

6. "Multi-Modal Nanoscale Cellular Probes" (Oral Presentation), UC-NL Lab Fees Symposium, Oakland, CA, USA, **Sept. 2017**

7. "Interfacing with Human Neurons: From Single Cell to Intact Brains" (Poster Presentation), CINT Annual Meeting, Santa Fe, NM, USA, **Sept. 2017**

8. "High Density Individually Addressable Nanowire Arrays Record Intracellular Neurons Potentials" (Oral Presentation), Neuroscience, San Diego, CA, USA, **Nov. 2016**

9. "High Density Intra-Cellular Neural Probes for Mapping the Brain" Conference (Oral Presentation), TechConnect World Innovation, National Innovation Summit and National SBIR/STTR, Washington, DC, USA, **Jun. 2015**

ABSTRACT OF THE DISSERTATION

Individually Addressable Nanowire Arrays for Probing Neuronal Culture and Tissue

by

Ren Liu

Doctor of Philosophy in Electrical Engineering (Nanoscale Devices and Systems)

University of California San Diego, 2019

Professor Shadi A. Dayeh, Chair

Nanowire electrode arrays are widely used to probe neuronal and cardiomyocyte's activities and are promising to bridge the gap between the standard gold technology of patch clamp and commercial microelectrode array to realize the large-scale intracellular recording with high signal-to-noise ratio. It is challenging to fabricate nanowire array to maintain both penetration ability for less invasiveness to the cell and biomechanical stability at the cell-nanowire interface

for long term recording. In addition to the challenge of obtaining an ultra-sharp nanowire tip, current nanowire arrays are constrained with their height and the presence of a number of extracellular nanowires, which limit their intracellular ability. Additionally, the intracellular recording mechanisms rely on electroporation which damages the cell membrane, leads to instability in the recording and prevents achieving long term recording ability. The objectives of this thesis, described in five chapters, are to develop individually addressable, ultra-sharp tip, high density, high-yield nanowire arrays to probe large neuronal network and cardiac tissues. Our platform will pave the way for longitudinal electrophysiological experiments on synaptic activity in human iPSC-based disease models of neuronal networks, critical for understanding the mechanisms of neurological diseases and for developing drugs to treat them.

In the second chapter, we created an individually electrically addressable, scalable, non-destructive, highly doped Si nanowire array for probing primary rodent and human stem cell derived neurons. The nanowire array has superior spatial resolution down to submicrometer site-to-site spacing and permits natural penetration into neuronal membranes. We developed an electrical model and deconvoluted the recorded potentials that resulted in millisecond wide action potentials that had similar properties to those measured by patch clamp. We validated the intracellular nature of nanowire-neuron interface by cross-sectional FIB/TEM. The neurons on nanowires were pharmacologically responsive: the activity increased with adding KCl and inhibited once adding TTX.

In the third chapter, we developed a high yield (100%) method for fabrication of nanowires array with ultra-sharp tip (a few tens of nanometer) based on Si substrate. The height, diameter, and pitch of nanowires are adjustable. The tip materials are flexible to change to any bio-materials, such as Au, Pt, Ag/AgCl, PEDOT-PSS. Surface roughness and materials are adjustable for better

cell-attachment and neurite growth. Electrophysiological recordings from mouse primary neurons revealed high signal to noise ratios with clear excitatory postsynaptic potential (EPSP) detection preceding action potentials. We recorded spike trains of action potentials from large neuronal network. Our ultra-shape nanowire array recorded neurons' clear responses to electrical stimulation and pharmacological drugs. The interfaces of neurons and nanowires were characterized by SEM/FIB demonstrating that the nanowires penetrated the neuronal membranes. Cardiac tissue activity was also recorded and showed pacemaker action potentials.

In the fourth chapter, we integrated Pt nanowires with bidirectional CMOS integrated circuits. Two methods were optimized for Pt nanowire integration by Focus Ion Beam. Rat cortical neurons were cultured and recorded. It was pharmacologically responsive to KCl and TTX, which indicated the stable nanowire-neuron interface.

In the fifth chapter, ongoing projects are introduced with regarding to the scalability to 1024 channel arrays, high density depth probe devices, large scale integration of nanowires with CMOS chip and electrofluidic neuronal interfaces.

Chapter 1

Motivation and Challenges for Interfacing Nanowires with Neurons and Cardiomyocyte Cells

1.1 Introduction

Neurodegenerative diseases and cardiovascular diseases influence the health for millions of people and impede their lives all over the world. In order to develop the effective medicines to treat them, drug screening is becoming more and more urgent. While we can today interrogate neuronal activity in intact brains, the first step for drug and toxicology screening is carried out on in-vitro tissue models. The cellular building blocks for the brain and the heart are neurons and cardiomyocytes, respectively. Both types of these excitable cells have all kinds of voltage-gated ion channels and receptors on the cell membrane (**Figure 1.1**). The electrochemical activity of voltage-gated ion channels forms these cells depict special function of health and disease states. Probing the minute electrochemical potentials, the subthreshold potentials, of the voltage-gated ion channels is an effective way for drug screening.

The patch-clamp is the gold standard procedure for measuring neuronal activity with high sensitivity but is generally restricted to single or few cells and is destructive. [1-5] To mimic the neuronal behavior in our body, we need to develop a platform that enables measuring neuronal activity from large neuronal networks. Microelectrode arrays enable recordings from networks of neurons, but they lack the sensitivity to subthreshold potentials that are critical

electrophysiological features for drug screening. [6] Nanowires offer potential for: intracellular recordings and sensitivity to subthreshold potentials, less-destructive interaction, scalability to interface with neuronal networks. [7-10]

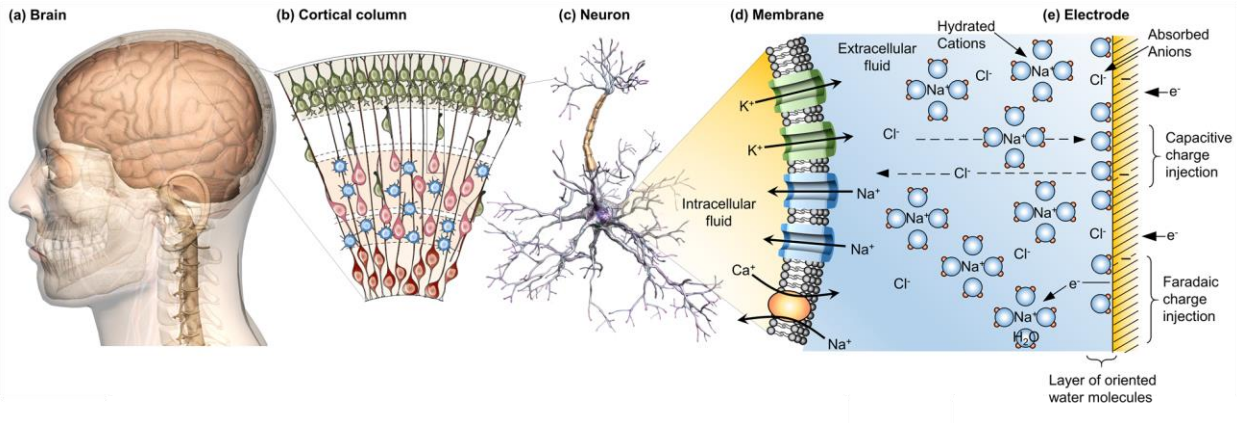

Figure 1.1 The human brain at multiple length scales interact electrochemically with interrogating electrophysiological probes. Schematic illustrations of (a) Human brain, (b) cortical column, (c) neuron, (d) neuronal membrane with channel proteins and lipid bilayers, and (e) interrogating electrode surface.

1.2 Current Status and Challenges for Interfacing Nanowires with Neurons and Cardiomyocyte Cells

Over the last decade, the nanowire interface with neurons emerged as a scalable and less-destructive technology which allows permeation to neuronal cell membranes for recording at high spatiotemporal resolution. [6, 18, 19] Some of these studies demonstrated that intracellular nanowire electrodes can measure intracellular potentials with magnitudes over 70 mV, [20-22] which are comparable to that of patch clamp. Despite its advantages, nanowire technology for probing intracellular potentials have some limitations particularly as to maintaining a reliable

nanowire-neuron interface over time. This challenge arises from the fact that the plasma membrane of the cells tends to reject (push out) the foreign material and reconstruct a continuous layer of cell/plasma membrane, which eventually isolates the nanowire from the cell body. [13] Once the nanowire is outside the neuron, the recording would just be extracellular. [23]

The endeavor in nanowire-neuron interfaces is to scale up stable intracellular electrode arrays for neural recording purposes. In order to record intracellular potentials while simultaneously achieving massive scaling and parallelization, current state of the art devices have focused on vertical nanowire electrode arrays and devices to interface with neuronal cells. [19] Nanowire electrodes have allowed ease of integration with micro and nanopatterning techniques, millisecond temporal resolution, and promising physical interaction and minimal invasiveness with cells based on the electrodes' geometry and shapes. [18, 24, 25] Dimensions of such nanowire electrodes range from sub-10nm [26] to μm-scale, [23] they achieve intracellular measurements through combinations of membrane penetration, electroporation (the application of electric fields above breakdown fields of the cellular membrane), and/or proper cellular engulfment. [11, 13, 22 23] One of the most prominent μm-scale vertical electrodes are the gold mushroom-shaped micro-electrode (gMμE) pillar arrays with individually addressable electrodes, developed by Hai et al.. [27, 28] Standard photolithography and electroplating methods are used to fabricate gMμE arrays (60 electrodes). The gMμEs are non-invasive, extracellular microelectrodes, but through proper engulfment of the electrodes by the cell membrane, "in-cell" recordings of intracellular potentials were demonstrated with cultured neurons, primary cardiomyocytes, striated muscle fibers, and non-excitable cells (NIH/3T3, CHO, PC-12, H9C2). The unique shape of the gMμEs essentially mimics the shape, structure, and dimension of neuron dendrite spines to self-force a cell to naturally engulf an electrode. [23] With additional chemical functionalization by RGD repeat

peptide or laminin, phagocytic engulfment was further improved. Similar to other state of the art electrode devices, a short electroporation pulse via gMμE allowed similar in-cell recordings for contracting cardiomyocytes and striated muscle fiber cells under in vitro conditions; the action potential signal amplitude varied from 5 mV to 10 mV. While earlier studies used μm-scale gMμE electrodes that recorded electrophysiological activity from relatively larger cells, such as Aplysia neurons and cardiomyocytes, recent gMμE have interrogated primary rat hippocampal neuronal cell cultures with excellent recording results that showed more than 90% monophasic positive action potentials with recorded potential amplitudes of up to 5mV. [29]

Xie et al. [13] have also utilized electroporation to achieve intracellular recording of action potentials. They specifically used 4 × 4 platinum pad arrays and each pad contained nanopillar structures with sub-100 nm tips. The nanopillars were fabricated using focused ion beam (FIB)-assisted platinum deposition and approximately 1-10 electrodes were formed on the platinum pads; the electrodes were thus not individually addressable. With nanoscale electrode tips and nanoscale electroporation, a large electric field temporarily breaks the membrane to permeate or provide access of the intracellular medium to the nanowires and facilitates measurements of intracellular action potentials of HL-1 cardiomyocyte cell cultures. The electroporation essentially allowed manual switching from extracellular to intracellular recordings; after the nanopillar electrodes deliver electroporation pulses, the intracellular signal amplitude increased to 11.8 mV compared to immediately prior measured extracellular signals with amplitudes of 100 to 200 μV. However, 120 seconds after the electroporation pulse, the signal amplitude decayed to 30% and the signal returned to extracellular characteristics after 10 minutes. The intracellular measurements were demonstrated on relatively larger cells (cardiomyocyte), similar to initial studies with gMμE.

Abbott et al. [30, 31] have utilized CMOS technology to achieve massive parallelization of 4096 simultaneous recording sites: the system was named CMOS neuroelectronic interface (CNEI). The CNEI system's vertical electrodes, or nanoneedles in this case, are not individually addressable, similar to the nanopillars by Xie et al. [13] Each of the 4096 recording sites (array of 64 by 64 aluminum pads) contains 9 platinum-black electrodes, which were fabricated precisely to have approximately 300 kΩ impedance. By coating platinum-black with characteristic surface roughness on platinum nanoneedles via electrodeposition, not only the surface area of the electrode was increased but also its characteristic electrochemical activity so much so that the CIC also increased. With a greater CIC, water hydrolysis was prohibited and micrometer-scale gas bubble formations were eliminated providing more reliable electroporation for intracellular access. During a recording session on in-vitro rat neurons (combined from cortex, hippocampus, and ventricular regions), 1837 sites showed parallel intracellular recording; in a separate 19 minutes recording/stimulation session, 1728 sites were observed to be recording in parallel and up to 982 sites showed simultaneous intracellular coupling. The CNEI demonstrated a platform to allow simultaneous measurements of subthreshold membrane potentials from many different neurons and facilitated characterization of neuron signal pathways and synaptic connections. However, intracellular coupling lasted only a relatively short time of only for around 8 minutes.

Zhao et al. [21] have focused on the structure and geometry of their nanowire devices and additional chemical modifications to gain minimally invasive access to the cell membrane. Most recently, Zhao et al. developed ultra-small nanowire probes for intracellular interrogation. With an appropriate nanoscale curvature on the cell membrane, they recorded intracellular potentials from primary rat dorsal root ganglion neurons and human cardiomyocyte cultures. The device is essentially a U-shaped Si nanowire field-effect transistor (FET) with a specific radius of curvature

made from 15-nm-diameter Si nanowire; with subsequent phospholipid chemical modification, nearly full amplitude intracellular recordings ranging from 60-100 mV was achieved. The conductance of the Si layer located at the tip of the device can be modulated by ionic potential fluctuations which in a biased transistor can lead to amplified sensitivity to these electrophysiological potentials. Immediately adjacent to the nanoscale Si region of the inserted nanowire device is a locally formed silicide alloy (NiSi) that established the source and drain contacts to the Si nanowire and was accomplished with Ni diffusion into the Si nanowire via rapid thermal annealing. The authors reported that these electrodes have potential to multiplex 168 channels. Similar to the other nanowire technologies described above, a decrease in the peak amplitude of the action potential amplitude was observed approximately 20 seconds after intracellular recording was established.

Despite the promise of nanowire electrode arrays for large-scale intracellular recording with high signal-to-noise ratio [11-17], there are several accompanying challenges. Their fabrication and the maintenance of both an intracellular and a biomechanically stable interface for long term recording continue to impede their widescale adoption. In addition to the challenge of obtaining a sharp nanowire tip, present nanowire arrays are constrained to the height of the nanowire and the number of extracellular nanowires, which limit their intracellular ability and rely on electroporation which causes damages the cell and deems the interface to be unstable for long term recording ability.

1.3 Overview of the Dissertation

The objectives of this thesis, described in four chapters, are to develop individually addressable, ultra-sharp tip, high density, high-yield nanowire arrays to probe large neuronal network and cardiac tissues. Our platform will pave the way for longitudinal electrophysiological

experiments on synaptic activity in human iPSC-based disease models of neuronal networks, critical for understanding the mechanisms of neurological diseases and for developing drugs to treat them.

In the second chapter, we created an individually electrically addressable, scalable, non-destructive, highly doped Si nanowire array for probing primary rodent and human stem cell derived neurons. The nanowire array has superior spatial resolution down to submicrometer site-to-site spacing and permits natural internalization into neurons. We developed an electrical model and deconvoluted the recorded signals resulting in millisecond wide potentials similar to those measured with patch clamp. We validate the intracellular nature of nanowire-neuron interface by cross-sectional FIB/TEM. The neurons on nanowires showed good pharmacological response: the activity increased with adding KCl and were inhibited once adding TTX.

In the third chapter, we developed a high yield (100%) method for fabrication of nanowires array with ultra-sharp tip (of the order of a few tens of nanometer) fabricated on a Si substrate. The height, diameter, and pitch of the nanowires were adjustable. The tip materials can be coated with desired bio-materials. The surface roughness and interface materials are adjustable for better cells attachment and nerite growth. Electrophysiological recordings from mouse primary neurons revealed high signal to noise ratios with clear excitatory postsynaptic potential (EPSP) detection preceding action potentials. We recorded spike trains of action potentials from large neuronal network. Our ultra-shape nanowire arrays recorded clear neuronal responses to electrical stimulation and pharmacological interventions. The interfaces of neurons with nanowires were characterized by SEM/FIB. Cardiac tissue activity was recorded and showed pacemaker action potentials.

In the fourth chapter, we integrated nanowires with CMOS chips. Two methods were optimized for Pt nanowire integration by Focus Ion Beam. Rat cortical neurons were cultured, recorded and pharmacologically tested. The pharmacologically responsive signals from rat cortical neurons verified the stable interface of neurons with the nanowire array.

In the fifth chapter, I will introduce the ongoing projects about the scalability to 1024 channel arrays, high density depth probe devices, large scale integration of nanowires and CMOS chip and electrofluidic neuronal interfaces.

This dissertation covers critical aspects of nanowire-neuron interface research from the fabrication, optimization, characterization of nanowire arrays platform, recordings from neuronal and cardiomyocyte cell culture, electrical stimulation, pharmacological interrogation of their activity, modeling of nanowire-neuron interface, validation the superb performance of the nanowire array platform, which collectively pave the way for drug screening.

Part of chapter 1 is currently being prepared for submission for publication as an invited review paper. Y. Tchoe, R. Liu, A. M. Bourhis, J. Lee, and S. A. Dayeh “Considerations and Recent Advances in Nanowire-Neuron Interfaces”. The dissertation author is author of this paper.

1.4 References

1. E. Neher, B. Sakmann, J. H. Steinbach, The extracellular patch clamp: a method for resolving currents through individual open channels in biological membranes. Pfluegers Arch. 1978, 375 (2), 219−228.

2. M. Martina, I. Vida, P. Jonas, Distal initiation and active propagation of action potentials in interneuron dendrites. Science 2000, 287 (5451), 295−300.

3. D. Henze, G. Buzsaki, Action potential threshold of hippocampal pyramidal cells in vivo is increased by recent spiking activity. Neuroscience 2001, 105 (1), 121−130.

4. M. Scanziani, M. Häusser, Electrophysiology in the age of light. Nature 2009, 461 (7266), 930−939.

5. Z. C. Lin, B. Cui, Nanowire transistors: room for manoeuvre. Nat. Nanotechnol. 2014, 9 (2), 94−96.

6. M. E. Spira, A. Hai, Multi-electrode array technologies for neuroscience and cardiology. Nat. Nanotechnol. 2013, 8 (2), 83−94.

7. W. Kim, J. K. Ng, M. E. Kunitake, B. R. Conklin, Yang, P. Interfacing silicon nanowires with mammalian cells. J. Am. Chem. Soc. 2007, 129 (23), 7228−7229.

8. G. Piret, M.-T. Perez, C. N. Prinz, Neurite outgrowth and synaptophysin expression of postnatal CNS neurons on GaP nanowire arrays in long-term retinal cell culture. Biomaterials 2013, 34 (4), 875−887.

9. L. Hanson, Z. C. Lin, C. Xie, Y. Cui, B. Cui, Characterization of the cell−nanopillar interface by transmission electron microscopy. Nano Lett. 2012, 12 (11), 5815−5820.

10. L. Gällentoft, L. M. Pettersson, N. Danielsen, J. Schouenborg, C. N. Prinz, C. E. Linsmeier, Size-dependent long-term tissue response to biostable nanowires in the brain. Biomaterials 2015, 42,172−183.

11. X. Duan, R. Gao, P. Xie, T. Cohen-Karni, Q. Qing, H.S. Choe, B. Tian, X. Jiang, C. M. Lieber, Intracellular recordings of action potentials by an extracellular nanoscale field-effect transistor. Nat. Nanotechnol. 2011, 7 (3), 174−179.

12. B. Tian, T. Cohen-Karni, Q. Qing, X. Duan, P. Xie, C. M. Lieber, Three-dimensional, flexible nanoscale field-effect transistors as localized bioprobes. Science 2010, 329 (5993), 830−834.

13. C. Xie, Z. Lin, L. Hanson, Y. Cui, B. Cui, Intracellular recording of action potentials by nanopillar electroporation. Nat. Nanotechnol. 2012, 7 (3), 185−190.

14. J. T. Robinson, M. Jorgolli, A. K. Shalek, M.-H. Yoon, R. S. Gertner, H. Park, Vertical nanowire electrode arrays as a scalable platform for intracellular interfacing to neuronal circuits.

Nat. Nanotechnol. 2012, 7 (3), 180−184.

15. M. R. Angle, B. Cui, N. A. Melosh, Nanotechnology and neurophysiology. Curr. Opin. Neurobiol. 2015, 32, 132−140.

16. X. Duan, T.-M. Fu, J. Liu, C. M. Lieber, Nanoelectronicsbiology frontier: From nanoscopic probes for action potential recording in live cells to three-dimensional cyborg tissues. Nano Today 2013, 8 (4), 351−373.

17. J. T. Robinson, M. Jorgolli, H. Park, Nanowire electrodes for high-density stimulation and measurement of neural circuits. Front. Neural Circuits 2013, 7, 38.

18. W. Zhou, X. Dai, and C.M. Lieber, Advances in nanowire bioelectronics. Reports Prog. Phys. 80, (2017).

19. J. Abbott, T. Ye, D. Ham, and H. Park, Optimizing Nanoelectrode Arrays for Scalable Intracellular Electrophysiology. Acc. Chem. Res. 51, 600 (2018).

20. Q. Qing, Z. Jiang, L. Xu, R. Gao, L. Mai, and C.M. Lieber, Free-standing kinked nanowire transistor probes for targeted intracellular recording in three dimensions. Nat Nanotechnol. 2014 Feb; 9(2): 142–147.

21. Y. Zhao, S.S. You, A. Zhang, J.H. Lee, J. Huang, and C.M. Lieber, Scalable ultrasmall three-dimensional nanowire transistor probes for intracellular recording. Nat Nanotechnol. 2019 Aug;14(8):783-790.

22. R. Liu, R. Chen, A. T. Elthakeb, S. H. Lee, S. Hinckley, M. L. Khraiche, J. Scott, D. Pre, Y. Hwang, A. Tanaka, Y. G. Ro, A. K. Matsushita, X. Dai, C. Soci, S. Biesmans, A. James, J. Nogan, K. L. Jungjohann, D. V. Pete, D. B. Webb, Y. Zou, A. G. Bang and S. A. Dayeh, "High Density Individually Addressable Nanowire Arrays Record Intracellular Activity from Primary Rodent and Human Stem Cell Derived Neurons" Nano Lett. 17 (5), 2757-2764 (2017).

23. A. Hai, A. Dormann, J. Shappir, S. Yitzchaik, C. Bartic, G. Borghs, J.P.M. Langedijk, and M.E. Spira, Spine-shaped gold protrusions improve the adherence and electrical coupling of neurons with the surface of micro-electronic devices. J R Soc Interface. 2009 Dec 6; 6(41): 1153–1165.

24. C. Chiappini, Nanoneedle-Based Sensing in Biological Systems. ACS Sens. 2017, 2, 8, 1086-1102.

25. A.F. McGuire, F. Santoro, and B. Cui, Interfacing Cells with Vertical Nanoscale Devices: Applications and Characterization. Annu Rev Anal Chem. 2018 Jun 12;11(1):101-126.

26. R. Liu and S.A. Dayeh, To Be Publ. (2020).

27. A. Hai and M.E. Spira, On-chip electroporation, membrane repair dynamics and transient in-cell recordings by arrays of gold mushroom-shaped microelectrodes. Lab Chip, 2012, 12, 2865–2873.

28. M. E. Spira, N. Shmoel, S. H. M. Huang, and H. Erez, Multisite Attenuated Intracellular Recordings by Extracellular Multielectrode Arrays, a Perspective. Front. Neurosci. 12, 1 (2018).

29. N. Shmoel, N. Rabieh, S.M. Ojovan, H. Erez, E. Maydan, and M.E. Spira, Multisite electrophysiological recordings by self-assembled loose-patch-like junctions between cultured hippocampal neurons and mushroom-shaped microelectrodes. Sci. Rep. 6, 1 (2016).

30. J. Abbott, T. Ye, K. Krenek, R.S. Gertner, S. Ban, Y. Kim, L. Qin, W. Wu, H. Park, and D.Ham, A nanoelectrode array for obtaining intracellular recordings from thousands of connected neurons. Nat. Biomed. Eng. (2019).

31. J. Abbott, T. Ye, L. Qin, M. Jorgolli, R.S. Gertner, D. Ham, and H. Park, CMOS nanoelectrode array for all-electrical intracellular electrophysiological imaging. Nat Nanotechnol. 2017 May;12(5):460-466.

Chapter 2

High Density Individually Addressable Nanowire Arrays Record Intracellular Activity from Primary Rodent and Human Stem Cell Derived Neurons

2.1 Introduction

Nanowire geometries are ideal for interfacing with cells and measuring intracellular potentials of neurons with minimal invasiveness. [1-6] Prior research efforts have demonstrated single nanowire devices [7-8] or devices encompassing ensembles of several nanowires [9-13] but individual electrical addressability of a single nanowire in a vertically standing array of nanowires, which is important for localizing the origin of action potentials, has not been accomplished before. Additionally, interfacing with human neurons, important for drug screening, is yet to be demonstrated. Here, we report a new hybrid integration scheme that offers for the first time a nanowire-on-lead approach which enables independent electrical addressability, is scalable, has a high spatial resolution and a sensitivity that allows the detection of subthreshold postsynaptic

potentials (PSPs). The fabrication of these nanowire arrays is demonstrated to be scalable down to submicrometer site-to-site spacing, and can be combined with standard integrated circuit fabrication technologies. Physiological recordings from rodent primary neurons and human induced pluripotent stem cell (hiPSC)-derived neurons revealed high signal to noise ratios for both positive and negative measured potentials. We measured electrical activity from rodent neurons from DIV 8 to DIV 14, and from hiPSC-derived neurons at 6 weeks in-vitro post culture and found intimate nanowire/neuron interaction validated by transmission electron microscopy. The technique contrasts to the standard patch-clamp, [14-17] which is destructive and unscalable to large neuronal densities and to long recording times, [18] or to planar multielectrode arrays that enable long-term recordings, but can just measure extracellular potentials and lack the sensitivity to subthreshold potentials. [19]

2.2 Fabrication Details

2.2.1 Solid-State Wafer Bonding Between Thin Si Substrates and Ni Electrodes on Sapphire Wafers

The 50 μm thick 4" Si substrates were obtained from Virginia Semiconductor Inc. and were carefully handled with plastic tweezers. The samples were diced into 5 mm × 5 mm pieces that were then gently cleaned in piranha solution (H_2SO_4:H_2O_2=3:1). Before the wafer bonding, the cleaned Si samples were dipped in buffered oxide etchant (BOE) to strip the surface oxide layer. On a separate sapphire substrate, photo and e-beam lithography were used to pattern the electrode leads followed by electron beam evaporation of Ti/Ni/Ti/Ni (30nm/200nm/50nm/200nm), and the sample was then washed with diluted NH_4OH (1:5 in DI) to remove the native NiOx surface layer.

After rinsing with DI wafer and a N_2 gun dry, these two samples are brought together and sandwiched by another two handling sapphire wafers.

A binder clip then clamps on these two handling wafers to apply enough compressive pressure (around 10 MPa) during the bonding. The wafer bonding is performed at 400 °C in a vacuum chamber with forming gas (3-3.8% H_2 in N_2) flow for 15 minutes. We used a similar procedure for the reliable integration of planar compound semiconductor layers (InGaAs) to SiO_2/Si substrates. [20]

Figure 2.1 shows initial bonding tests of Si to sapphire and SiO_2/Si using NiSi formation. The nature of the solid-state reaction permits the realization of isolated NiSi leads underneath the bonded Si substrate (**Figure 2.1 (d)**). The ohmic contact characteristics of the Ni_xSi_y contact with Si was studied on a relatively moderate/high resistivity Si substrate (ρ=0.01 Ω.cm) where the annealing temperature in forming gas was varied from room temperature to 800 °C. As expected, we found that NiSi formed at 400 – 600 °C resulted in the lowest contact interface resistance for the test structures and the $NiSi_2$ phase at 800 °C results in higher contact resistances. [21] Therefore, the low temperature anneal has also the advantage of obtaining low ohmic contact resistances and therefore used in out integration schemes.

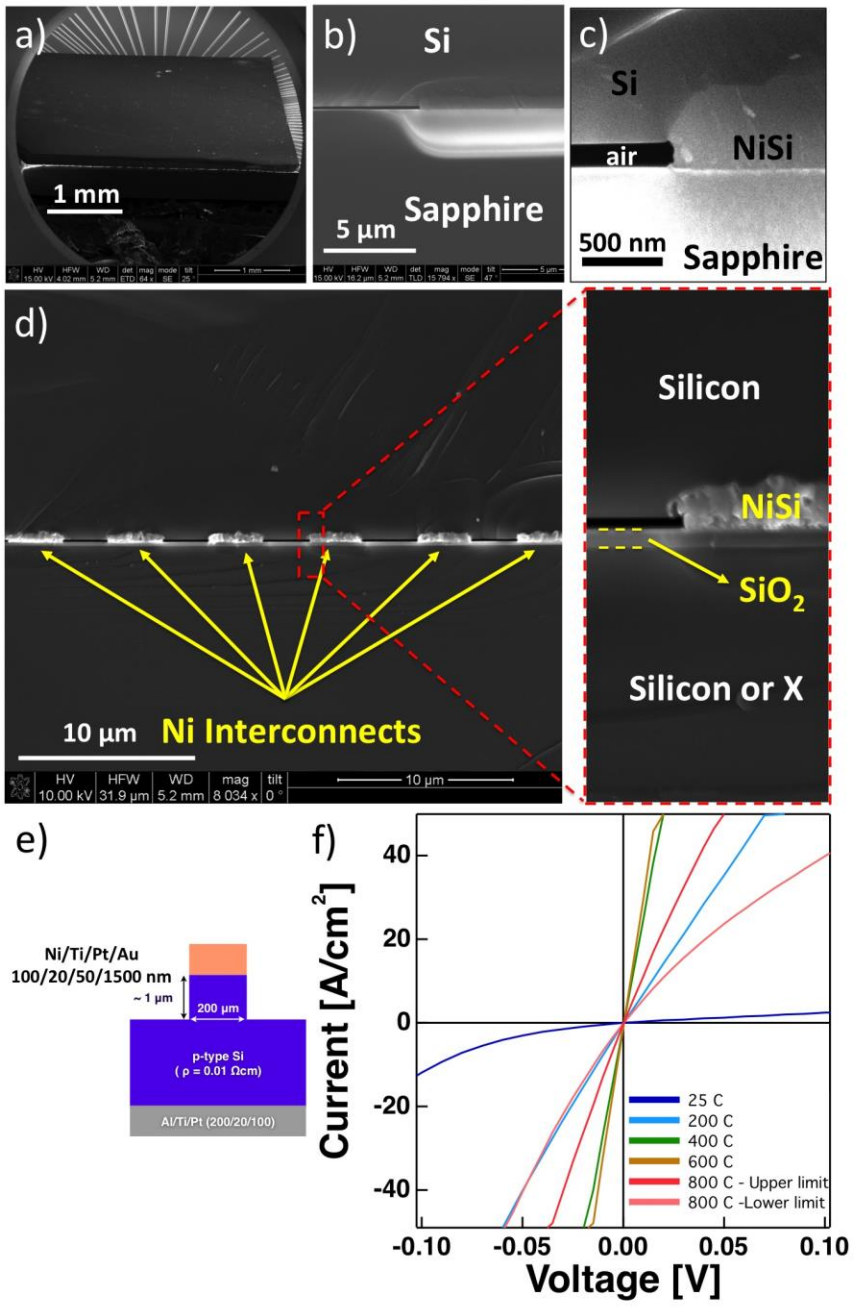

Figure 2.1 (a) Cross-section SEM image of a 5 mm × 5 mm Si substrate bonded to a sapphire substrate. (b) Close-up SEM image near one NiSi reacted electrode lead and (c) higher magnification SEM showing intrusion of the NiSi into the Si substrate and recession of the Si substrate reducing the air gap between Si and the sapphire substrate. (d) NiSi bonding performed on patterned Ni leads on a SiO_2/Si substrate with a zoom-in to the interface at one electrode site (right panel in (d)). e) Test structure for current-voltage characteristics as a function of annealing temperature with Ni being in contact with Si, and d) results showing rectifying behavior at room temperature followed by linear ohmic-like current-voltage characteristics or all annealing temperatures with lowest resistance/highest currents for the 400 – 600 °C annealing reaction temperature. Courtesy of Dr. Yoontae Hwang.

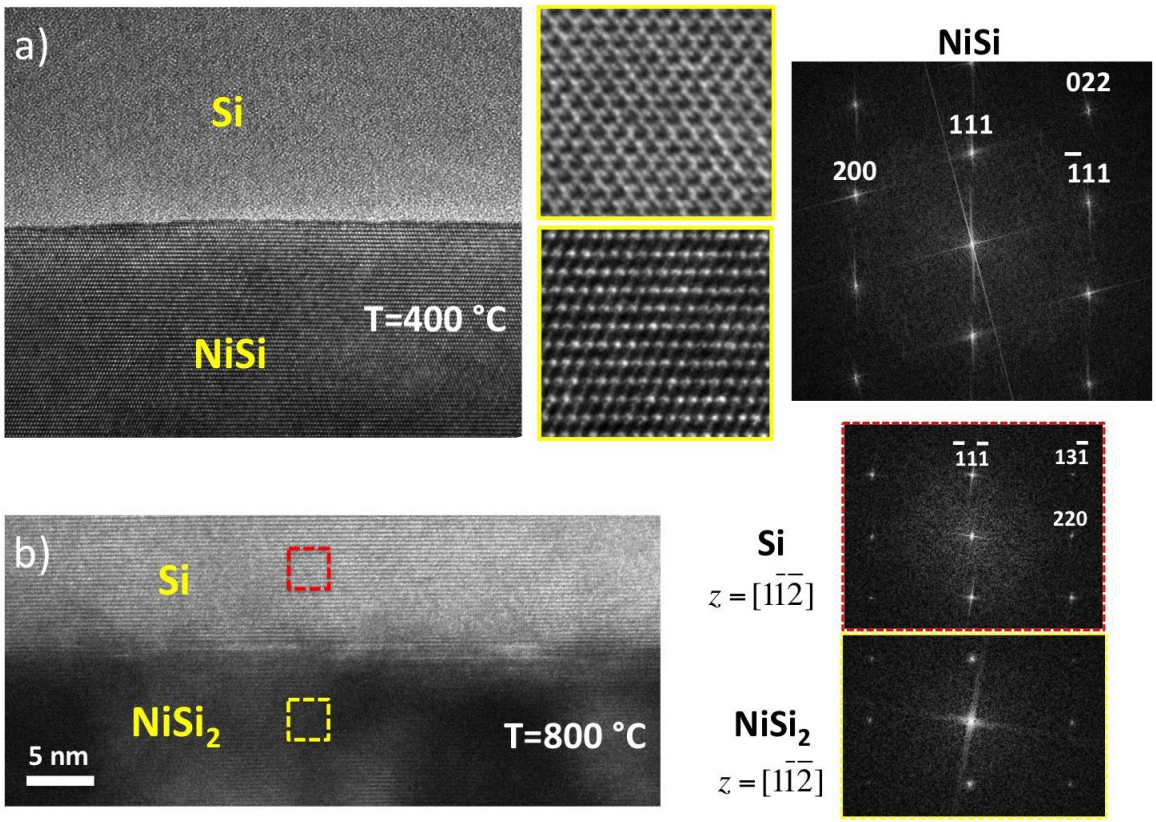

Figure 2.2 Transmission electron microscopy of the NixSiy/Si(111) interface for two annealing temperatures. a) At 400 °C, a NiSi orthorhombic phase is formed. At 800 °C, a cubic $NiSi_2$ phase is formed that is nearly lattice matched to Si. Courtesy of Dr. Wei Tang.

2.2.2 RIE/ICP Dry Etching Processes for Si Thinning and Si Nanowire Etching

After the wafer bonding, the 50 μm thick Si chip was thinned down to ~ 10 μm utilizing the RIE/ICP dry etching tool (Oxford Plasmalab 100). SF_6 gas of 80 sccm with RIE/ICP powers of 200 W/1500 W were used for the rapid thinning process (~ 4.2 um/min). During the Si nanowire etching step, following the Ni etching masks, a combination of SF_6 18 sccm and C_4F_8 56 sccm gases were introduced for etching nanowires with smooth sidewalls. An RIE/ICP powers of 30 W/1200 W were optimized to control the nanowire etch profile. The Si nanowire etching is

concluded when all the surrounding Si was removed and an O_2 plasma etch followed to remove polymers that were built up during the etching process.

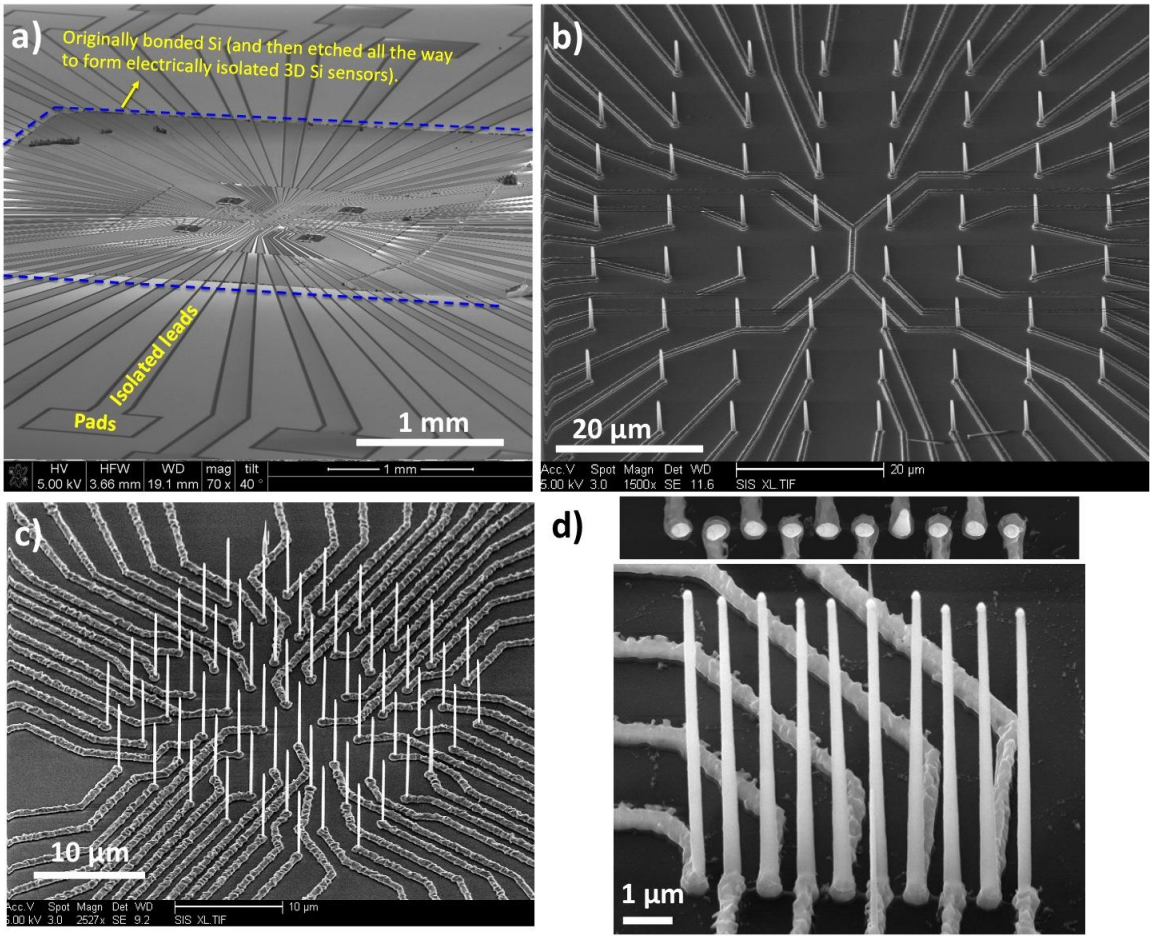

Figure 2.3 SEM images of etched nanowire arrays on sapphire substrate. (a) Angle view SEM image of the overall platform after Si nanowire etching. The width of the platform is 1.5 cm. (b) SEM image of Si nanowires etched at a pitch of 10µm site-to-site spacing. (c) SEM image of Si nanowires etched at a pitch of 4 µm site-to-site spacing. (d) SEM image of a linear array of Si nanowires etched at a pitch of 750 nm site-to-site spacing.

2.2.3 SiO_2 Layer Passivation

The whole device, except the big pads for electrical connections, was coated with 400 nm SiO_2 (Oxford Plasmalab PECVD), resulting ~ 200 nm thick SiO_2 on Si nanowire sidewalls. Then,

a thin PMMA layer (PMMA 950 A4, ~ 200 nm) was applied to the entire device by spin-coating (4000 rpm, 150 rpm/s, 60s), followed by baking at 170 °C for 10 mins. A short O_2 plasma treatment (PE-100 Benchtop Plasma System, 200W, 12s) can expose the PMMA at the tip of Si nanowires. After that, a short BOE dip (70s) can remove the SiO_2 only at the tip of Si nanowires. Finally, this PMMA layer can be stripped by O_2 plasma cleaning (PE-100 Benchtop Plasma System, 200W, 12 mins).

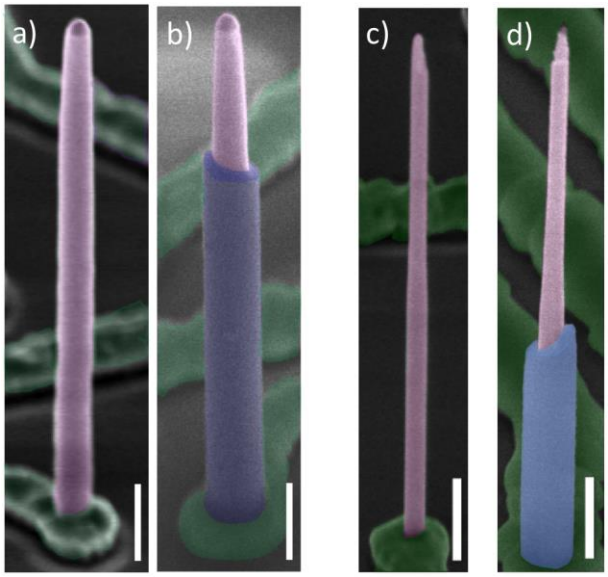

Figure 2.4 The human brain at multiple length scales interact electrochemically with interrogating electrophysiological probes. Schematic illustrations of (a) Human brain, (b) cortical column, (c) neuron, (d) neuronal membrane with channel proteins and lipid bilayers, and (e) interrogating electrode surface. Scale bar 500nm.

2.2.4 Extension to Other Array Geometries and Overall Passivation with SU8

The integration scheme can be used to tailor the array geometry and to the inclusion of microfluidic/neurite growth channels. It has been demonstrated that hexagonal patterns in SU8 layers provide optimal geometry for neuronal growth to promote axonal growth between neurons

plated at the vortices of the hexagonal pattern. [22] We demonstrated that our integration technology is suitable to define patterned nanowire arrays as shown in **Figure 2.5** and correspondingly microchannels in 10 μm thick SU8 resist as shown in **Figure 2.5 (c)** and **(d)**.

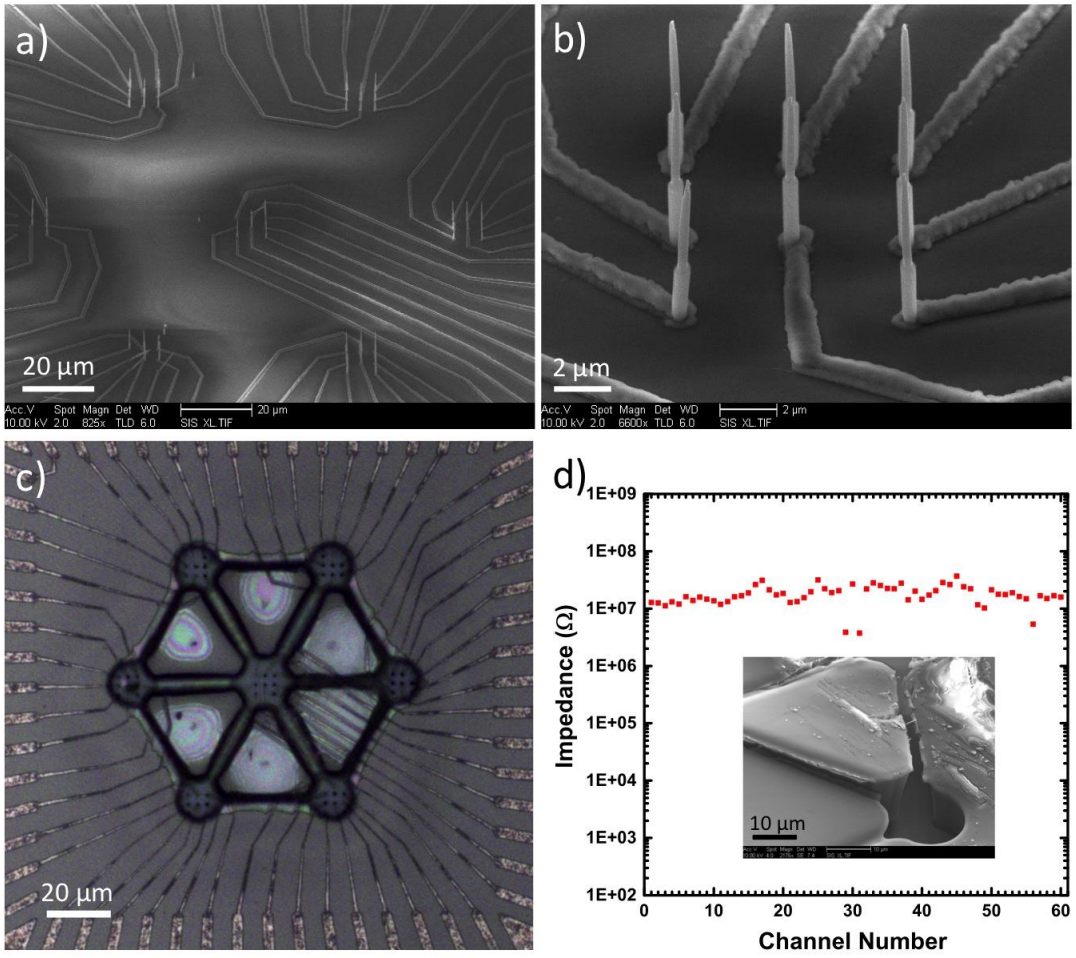

Figure 2.5 SEM images of Si nanowires arrays arranged in a hexagonal pattern with 7 vortices (a) and zoom-in to a single vortex with 8 nanowires (b). (c) Definition of neuron plating regions with SU8 with optimized processing conditions to seal a microfluidic channel in SU8 that connects the vortices of the hexagon and yet maintains a sealed top to prevent neuron plating in these microfluidic channels. (d) Electrochemical impedance spectroscopy was conducted on all 56 channels which displayed a consistent 1kHz impedance magnitude of ~ 20MΩ as discussed in **Figure 2.8**. Inset of panel (d) is a mechanically displaced SU8 region surrounding a microfluidic channel demonstrating that the sealed channel is indeed well developed and free of SU8 potentially permitting neurite growth between the hexagonal vortices.

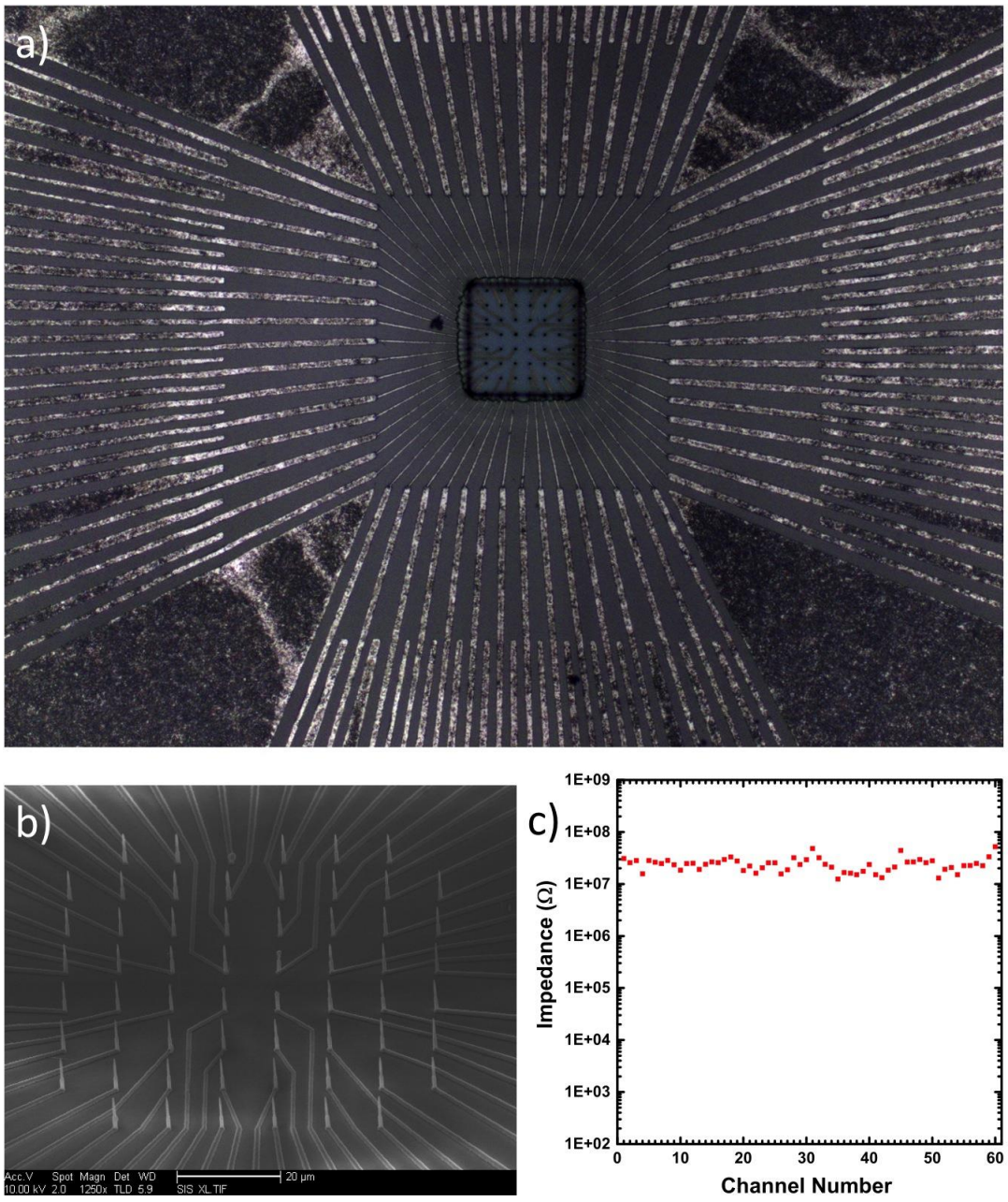

Figure 2.6 (a) Optical microscope image of a patterned SU8 layer on a square array (b) to confine neuron cell plating and electrochemical interactions with the exposed nanowires. The electrochemical impedance of the array nanowires is shown in panel (c).

The same passivation procedure has also been applied to the square array pattern. **Figure 2.6** shows a square array of Si microwires with 10µm pitch that was patterned to allow neural cell

plating in the square array region. The electrochemical impedance was also consistent among the 56 channels and with that of the hexagonal patterns (~20MΩ at 1kHz).

2.2.5 Packaging

After device fabrication, the samples were bonded via conductive epoxy (EpoxySet EO-21M-5) to commercially available Ayanda Biosystems printed circuit boards that are compatible with conventional neurophysiology stations. Bonding was performed at 80 °C for 3 hours in ambient). Quartz tubes were then bonded with Polydimethylsiloxane (PDMS) to localize the neuron culture chamber. (**Figure 2.7**). Either PDMS or SU8 were then used to tight seal the inner portion of the nanowire array chip and the bottom of the PCB (**Figure 2.7**) against fluid leakage. Both of these seals were found to be leak-proof over several weeks of neuron culture (up to 8 weeks in our experiments before disassembling the sample for imaging).

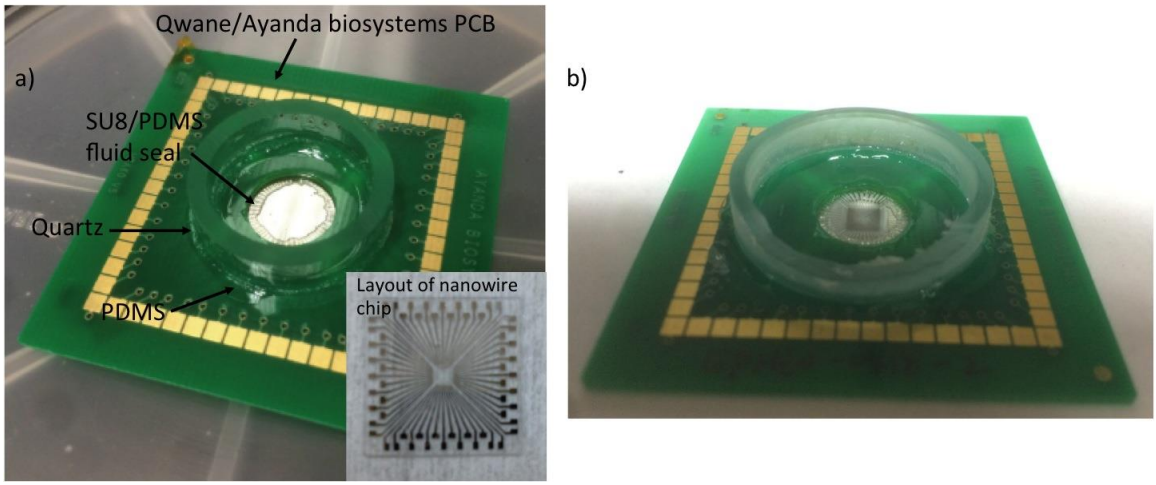

Figure 2.7 (a) Picture of packaged nanowire array chip (lower right inset) with details of the different used layers except for the conductive epoxy between the pads on the back of the PCB and the top of the nanowire chip. (b) picture of a different device showing a dark region in the center which is the same size of the bonded 5mm × 5mm starting Si substrate.

2.3 Device Characterization

2.3.1 Electrochemical Impedance Spectroscopy

Si nanowire arrays with SiO_2 passivation and exposed tips with and without the SU8 patterned layers were subject to 3-terminal electrochemical impedance spectroscopy using a Gamry Instruments potentiostat. The measurements were conducted in phosphate buffered saline solution (ThermoFisher Scientific) with a Pt counter electrode (CH129, Chin Instruments) and Ag/AgCl reference electrode (CH111, Chin Instruments). **Figure 2.8** shows a sample measurement for impedance magnitude and phase indicating a mostly capacitive coupling to alternating charge density in the saline solution. The electrodes are therefore referred as capacitive in nature.

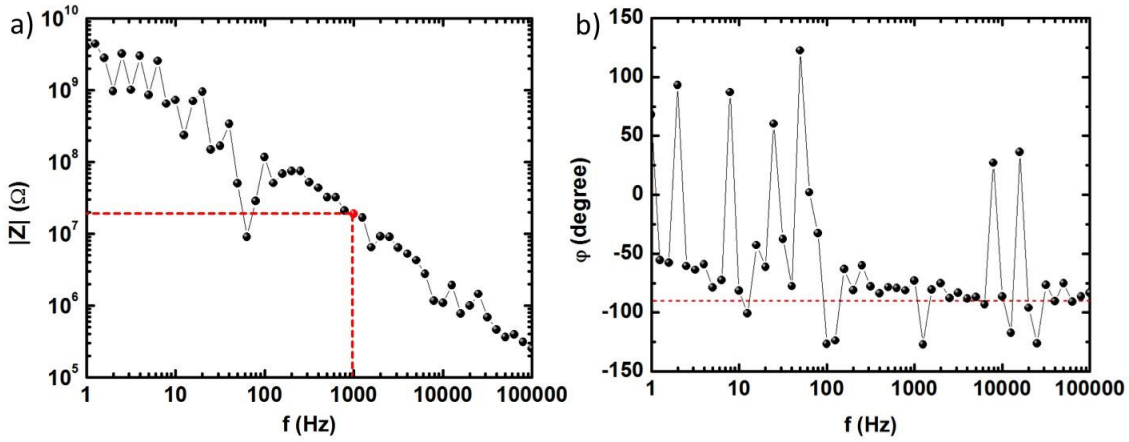

Figure 2.8 Electrochemical impedance spectra for a single Si nanowire. (a) Magnitude and (b) phase.

Using a parallel RC model (solution resistance can be safely neglected), we approximated the faradaic component to have a 65MΩ resistance, and the capacitive branch to have 8pF

capacitance. This is large given that the exposed tip of the Si nanowire is 1-3μm long. However, given that the SU8 covered leads or non SU8 covered leads resulted in similar impedances, the stray capacitance is less likely to play a role in these measurements and it is likely that the electric field intensification at the nanowire tips contributes to the enhanced capacitance.

2.3.2 Transmission Electron Microscopy (TEM) Samples Preparation with Focused Ion Beam (FIB) Milling

2.3.2.1 Sample Preparation for Focused Ion Beam Milling

To prevent the sample from the damage by ion beam during the FIB milling process, the fabricated device is deposited with 1μm SiN_x by Trion Orion III chemical vapor deposition (CVD) system. This SiN_x layer also provides better contrast to the passivating SiO_2 dielectric layer on Si nanowire probes for elemental mapping. After that, the sample was coated with a 30nm Pt layer by e-beam evaporation to reduce the charging under electron and ion beams.

2.3.2.2 Focused Ion Beam Milling and In-situ Lift-out (INLO)

The TEM sample lamellae was prepared with FIB (FEI Nova 600). The FIB and INLO process utilized here follow conventional procedures, in which a 30keV Ga beam was used for rough milling and reduced voltage (10keV) was used for fine milling. The slice of cross-section sample was transferred to the TEM grid first and was thinned down to 50 nm (thickness of slice).

2.3.2.3 Transmission Electron Microscopy Characterizations

TEM characterization was carried out using a FEI Tecnai G(2) F30 S-Twin 300kV transmission electron microscope, equipped with Fischione Instruments high angle annular dark field (HAADF) and EDAX ECON energy-dispersion x-ray (EDX) detectors under scanning TEM

(STEM) mode. Those experiments were performed at the Center for Integrated Nanotechnologies at Sandia National Laboratories.

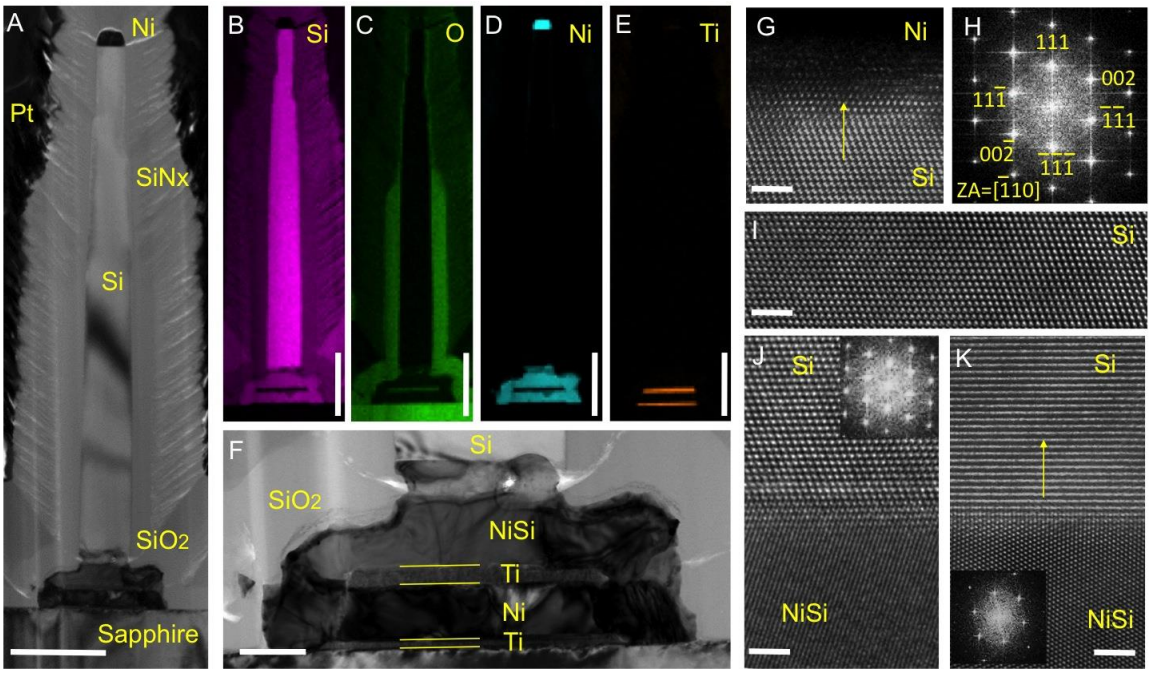

Figure 2.9 TEM characterization and elemental mapping of a single Si nanowire on sapphire substrate. (A) Low magnification TEM image of a single Si nanowire bonding with Ni/Ti/Ni/Ti electrode on sapphire substrate. The sample is coated with additional SiNx and Pt for the purpose of cross-sectioning for TEM studies. Scale bar is 1 μm. EDX element mapping of Si (B), O (C), Ni (D) and Ti (E), respectively. Scale bars are 1 μm. (F) Higher magnification TEM image of the Ni/Ti/Ni/Ti electrode, and the interface of Si and NiSi. Scale bar is 200nm. (G) HRTEM image of the interface between Si and Ni at the Si nanowire tip and its Fast Fourier Transform (FFT) pattern in (F). HRTEM images at the center area of Si nanowire (I), and at the interface between Si and NiSi with electron beam axis aligned in the Si $[1\bar{1}0]$ (J), and the NiSi $[1\bar{1}0]$ Zone axis in (K). Scale bars in G, I, J, K are 2nm.

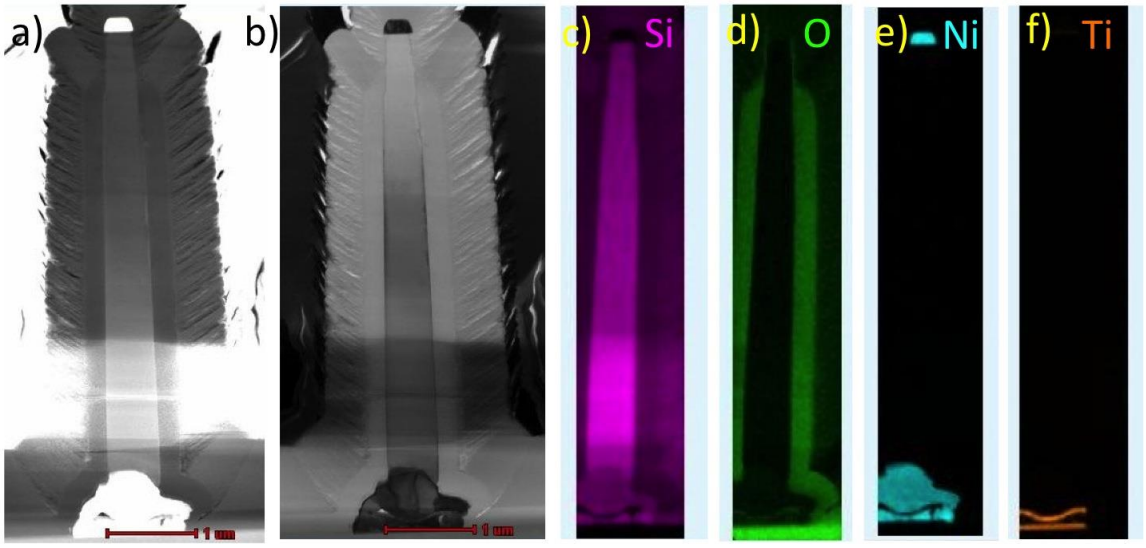

Figure 2.10 TEM characterization and elemental mapping of another Si nanowire on sapphire substrate (a) HAADF STEM image of a Si nanowire on sapphire substrate. (b) Bright-field (BF) image of same nanowire in (a). (c-f) elemental mapping showing Si (c), O (d), Ni (e) and Ti (f) composition of the nanowire structure. These characteristics are generally consistent with that in **Figure 2.10** and other wires characterized on sapphire and SiO_2/Si substrates.

2.3.3 Transmission Electron Microscopy Characterization on Electrophysiologically Measured Devices with Cells

2.3.3.1 Sample Preparation of Electrophysiologically Measured Devices with Cells

To prepare the electrophysiologically measured devices with cells for SEM/FIB/TEM, cells were fixed, dehydrated, critical point dried and coated with IrO_x. Cell's fixative mediums were the mixes of distilled water, sodium cacodylate buffer (0.2 molor, pH 7.4) and Glutaraldehyde solution (G58882-10X1ML, Grade I, 25% in H_2O) with the ratio of 4 : 5 : 1. We first melted Glutaraldehyde solution at 37 deg C water bath, then mix these mediums together by using spinner of VORTEX-GENIE 2 for 3 mins. Firstly, the growth media was rinsed with PBS for three times. Subsequently, the samples had undergone a cell fixation protocol, in which a solution containing 2.5 % glutaraldehyde in 0.1 M cacodylate buffer at pH = 7.4 was added. The

sample was let sit for 1 hour at room temperature and was the washed three times in PBS with leaving the sample in PBS solution for 5 min after each rinse. The samples were then rinsed off buffer salts with three times wash in distilled water, 5 min for each rinse. The samples were then subjected to a dehydration procedure in which they were serially dehydrated in 30, 50, 70, and 90% (10 min each) and three times with 100% ethanol. Following the dehydration procedure, the samples were dried in critical point dry (CPD) by using Autosamdri-815 for ~10-15 minutes. Finally, a 10nm IrOx was sputtered on the surface of the sample for SEM and 100+ nm of Ti was deposited on sample for FIB.

2.3.3.2 Focused Ion Beam Milling and Transmission Electron Microscopy Characterizations

The transmission electron microscopy on electrophysiologically measured devices and their preparation and imaging procedures are similar to those presented in section **2.3.2** without SiO_2 or SiN_x deposition to avoid heating during the PECVD. We show below sequences of images in the preparation of the sample characterized and presented in **Figure 2.11** and the corresponding TEM images from the back-side.

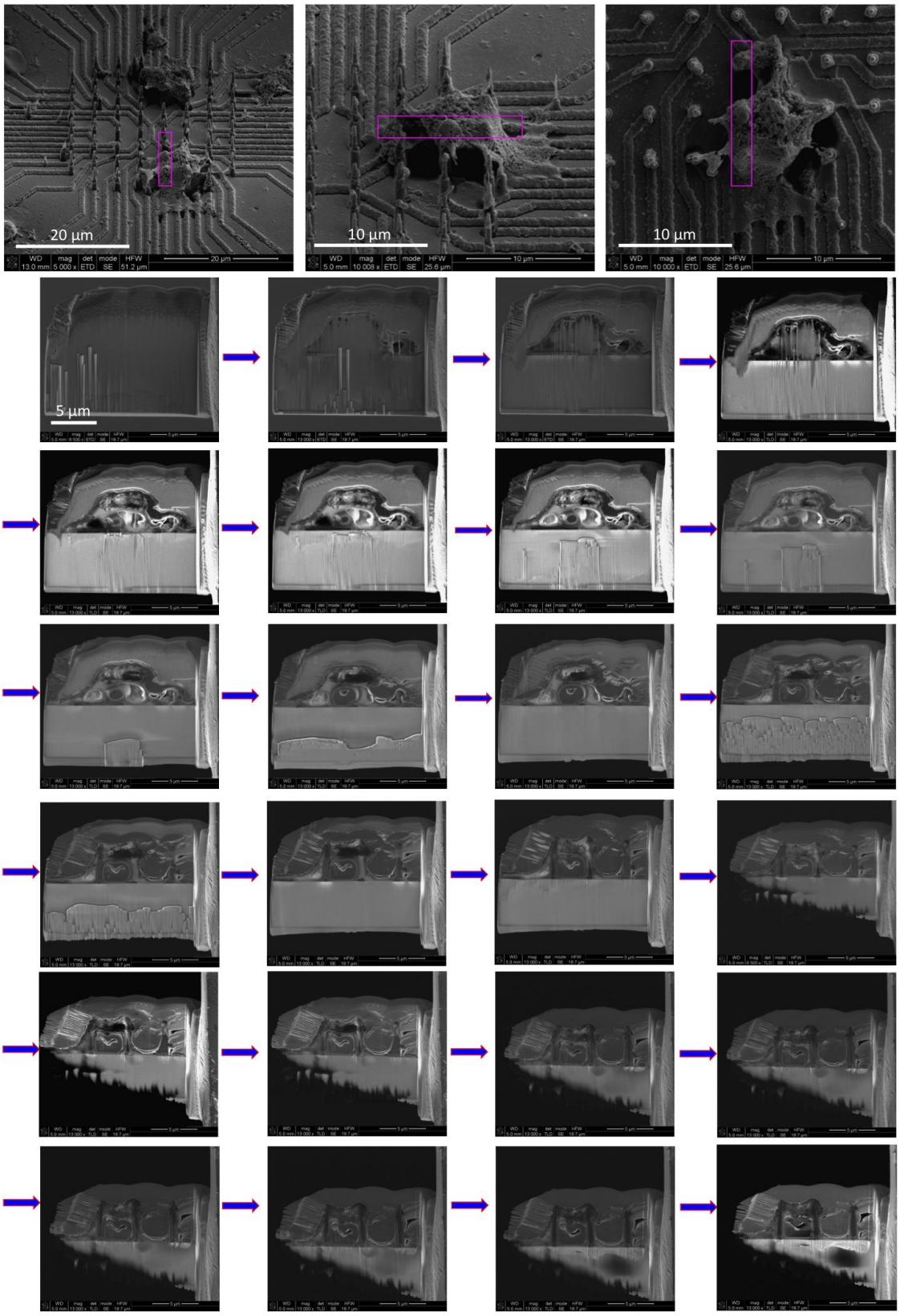

Figure 2.11 Sequential SEM imaging before (top row) and during (rest of SEM images) the FIB thinning of wires 6, 7 & 8 marked with a rectangular box in the top SEM images.

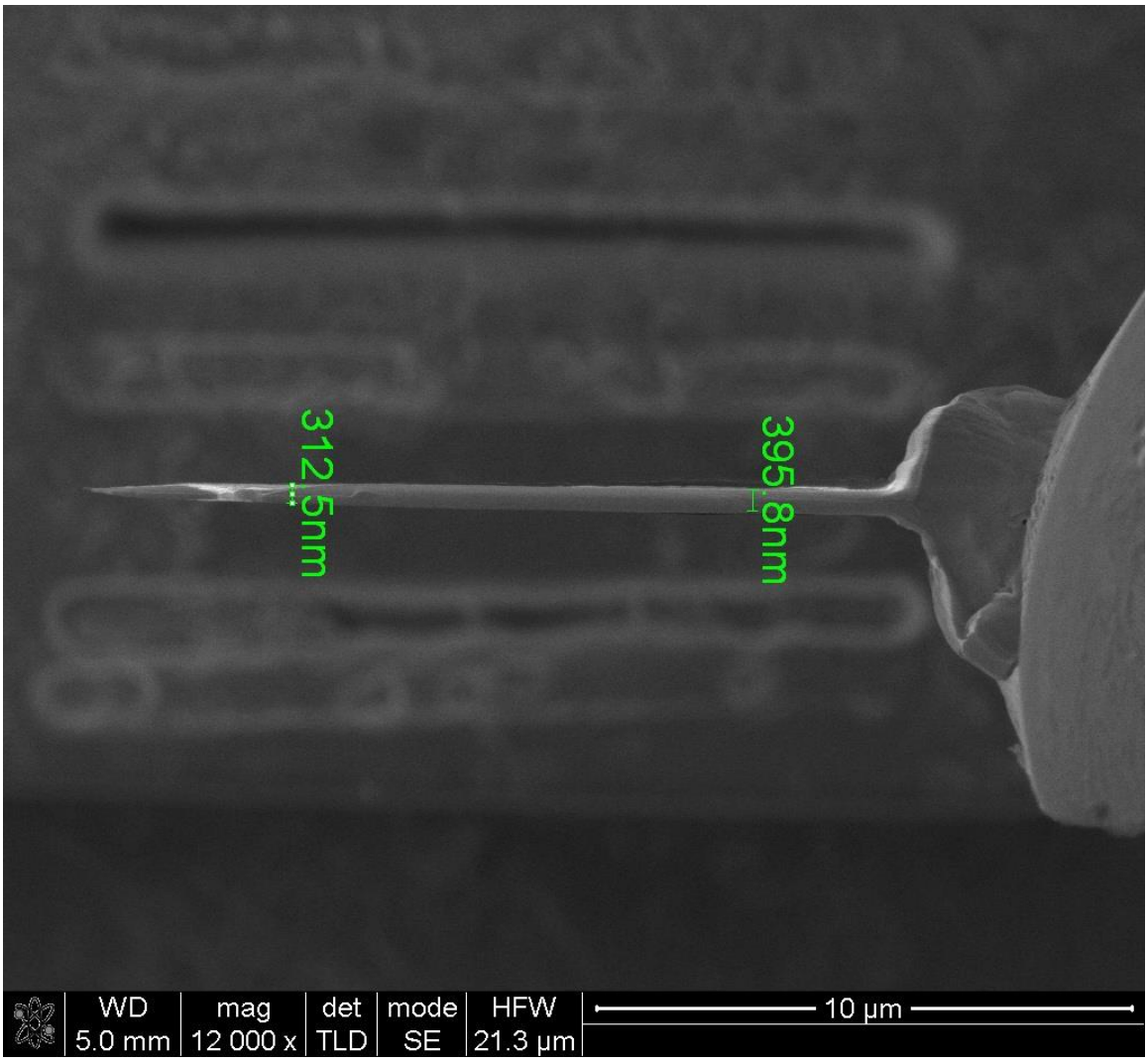

Figure 2.12 Top view SEM image of the FIB thinned sample prepared for TEM characterization.

2.4 Cell Culture and Pharmacological Stimulation and Inhibition

2.4.1 CA1-CA3 Mouse Hippocampus Neurons

In preparation for plating of mouse hippocampal neurons, plates were incubated over night at room temperature with Poly-D-Lysine (80mg/mL; Millipore) in Phosphate-buffered saline (Cellgro). The following day, plates were washed and incubated with Poly-D-Lysine (40 mg/mL) and Laminin (2.5mg/mL; Invitrogen) in Phosphate-buffered saline for 3 hours at 37 ℃. Culture

media was prepared from Neurobasal Medium (Gibco) supplemented with 5% Fetal Bovine Serum (Gibco), 2% B27 supplement (Gibco), 1% Glutamax (Gibco), and 1% Penicillin/Streptomycin (Cellgro).

Hippocampi were isolated from E18 mouse embryos from pregnant CD1-IGS mice (Charles River Laboratories). Cells were dissociated by incubation at 37 ℃ in a 0.25% Trypsin/ 2.21 mM EDTA solution (Corning) and triturated by pipetting. After pelleting heavy debris, the cell solution was diluted to a density of 1 x 106 cells/mL and 200μL of the resulting solution was plated directly onto the coated nanowire array. Additional culture media was added to bring the total volume to 1.5-2 mL. Cultures were maintained at 37 °C in an atmosphere containing 5% CO_2. Half of the culture media was exchanged every 3 days. Cytosine arabinoside (AraC; working concentration 4μM) was added from the 6th day of culture to suppress the proliferation of glial cells.

2.4.2 Human Induced Pluripotent Stem Cell (hiPSC) Derived Neurons

All human stem cell culture was performed under approval from the Stem Cell Research Oversight (SCRO) panel at Sanford Burnham Prebys Medical Discovery Institute. Undifferentiated human pluripotent stem cells (generous gift from Dr. April Pyle, UCLA), were cultured on irradiated mouse embryonic fibroblasts in hESC media (DMEM/F12, 20% Knockout Serum Replacement, 1X non-essential amino acids, 110 μM beta-mercaptoethanol, penicillin-streptomycin, and 10ng/ml bFGF). Cortical neurons were differentiated from hiPSC with an established protocol as previously described. [23, 24] HiPSC-derived cortical neurons were treated with 5 μM cytosine arabinoside and passaged onto the nanowire device or multielectrode array plate (Axion Biosytems). HiPSC-derived dopaminergic neurons (iDopa neurons, Cellular Dynamics International) were thawed according to manufacturer's instructions and plated directly

onto the nanowire device. Human astrocytes were added to the hiPSC-derived dopaminergic neurons one week prior to recording (ScienCell Research Laboratories). The nanowires or multielectrode arrays (MEA) were pre-coated with 0.1% polyethylenimine (PEI) and hiPSC-derived cortical or dopaminergic neurons plated in Neurobasal A, 10% Knockout Serum Replacement and 10 μg/ml Laminin. Neuronal cultures were maintained in Brainphys media (Stemcell Technologies) optimized for electrophysiological recordings [25] in a humidified 37 °C incubator with 5% CO_2. 60% media were exchanged every other day.

2.4.3 Primary Rat Cortical Neurons

The nanowire array devices have been coated with 0.1% PEI for 1h at room temperature, followed by several washes in PBS and left overnight in the hood for drying. The following day 1:50 laminin solution in PBS have been added for 1h at 37 °C, and then removed right before the plating. Commercially available primary rat cortex neurons (Gibco) were plated on the nanowire array at a density of 200000 cells each device following manufacturer's instruction, and they were kept in Neurobasal medium (Gibco) with 1:100 Glutamax-I (Gibco), 1:50 B27 (Gibco) and 1:100 Penicillin/Streptomicyn (Mirus). Half of the medium was changed every three days for the duration of the experiment.

2.4.3.1 Neurophysiology Recording with Nanowires

Measurements were conducted on a Tucker Davis Technologies (TDT) RZ2 neurophysiology system equipped with a PZ5-64 channel neuro-digitizing preamplifier, RS4 data streamer, and an MZ60 multielectrode array headstage and amplifier. Mouse hippocampal neurons were recorded in aCSF (NaCl 119mM, KCl 2.5 mM, NaH_2PO_4 1mM, $NaHCO_3$ 26.2 mM, Glucose 11mM, $MgCl_2(7H_2O)$ 1.3mM, $CaCl_2(2H_2O)$ 2.5 mM) and for some recording sessions, the solution was bubbled with 95% O_2 + 5% CO_2 gas for at least 30 minutes prior to recording and

also during the recording session. HiPSC-derived neurons were maintained in Brainphys media as the recording solution. 2-3 minutes of baseline measurement was conducted to observe spontaneous neural activity. Then 13mM KCl was added to the device chamber and recorded for 2-3 minutes to observe pharmacologically stimulated neural activity. To prove the physiological potentiation of the electrophysiological activity of the cells, we added 197 μM of Glutamate to the recording solution/medium. Lastly, 1 μM tetrodotoxin (TTX) was added to the solution to inhibit neural activity.

For some experiments, after the first 2-3 minutes of baseline recording, the glutamatergic and the GABAergic receptors have been blocked by adding 50 μM D-APV (Abcam), 10 μM CNQX (Sigma) and 1 mM Picrotoxin (Tocris) in the medium. The cells have then been recorded in the presence of the blockers. Afterwards the cells have been washed by changing the medium 5 times, 5 minutes each wash, and then recorded again post-washout.

After recording, neurons grown on nanowires devices were processed for immunocytochemistry and/or SEM and/or TEM imaging.

2.4.3.2 Neurophysiology Recording with Reference Multielectrode Array

hiPSC-derived cortical neurons were plated on MEA plates composed of 48-wells with 16 electrodes per well (Axion Biosystems). Recordings were acquired with the Maestro and Axion Integrated Studio. A Butterworth band-pass (10-2500Hz) filter and adaptive threshold spike detector set to 5.5X standard deviations were applied to the raw data. Raster plots of neuronal spiking activity were generated using Axion Neural Metrics Tool. Neurons were grown and recorded in Brainphys media. Spontaneous activity was measured as baseline, followed by pharmacological treatment with 2 mM KCl and then 1 μM TTX (**Figure 2.13**).

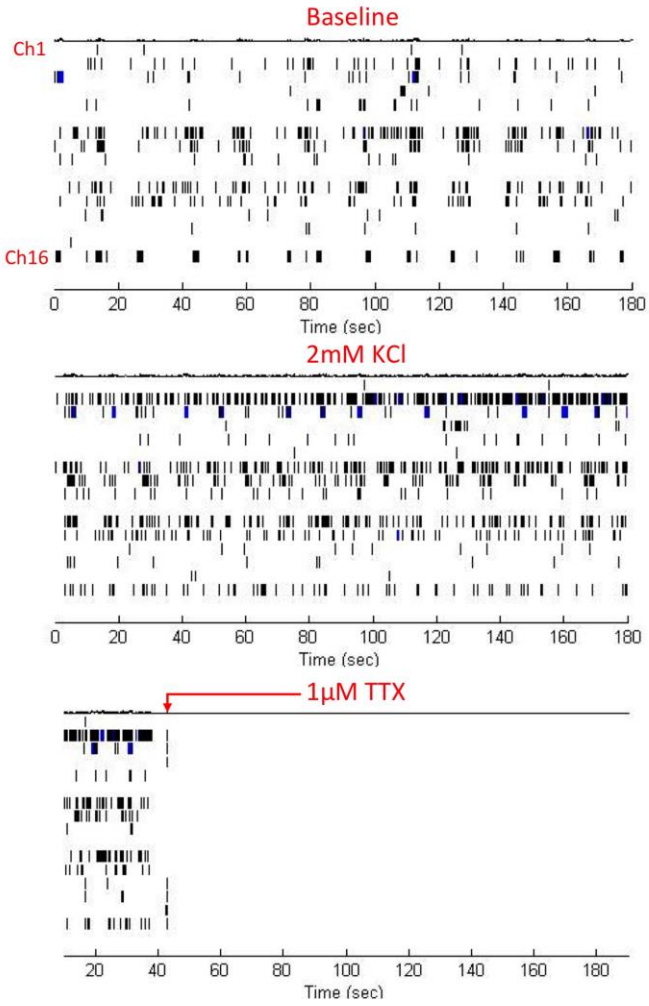

Figure 2.13 Reference measurements using commercial planar Axion electrodes/neurophysiology system. Similar patterns of firing in baseline, KCl stimulation, and TTX inhibition to those measured using the Si nanowire array platform were observed.

2.4.4 Immunocytochemistry

After recording, the cells have been fixed in paraformaldehyde 4% for 12 minutes at room temperature. After washing the PFA three times with PBS, the cells have been blocked in 5% Donkey Serum and permeabilzed in 0.1% Triton-X. They have been stained with mouse Neuronal Class III β-Tubulin (Tuj1) (Covance, 1:250 in blocking buffer) overnight at 4°C. The following day the primary antibody was washed off several times in PBS, and the secondary antibody (mouse

Alexa Fluor 488) was added 1:500 in blocking buffer for 2 hours at room temperature. The secondary antibody was then washed several times in PBS and the DAPI (Thermofisher, 1:2000 in PBS) was added for 30 minutes at room temperature. The samples have been imaged with an Inverted IX81 Olympus Compound Fluorescence Microscope.

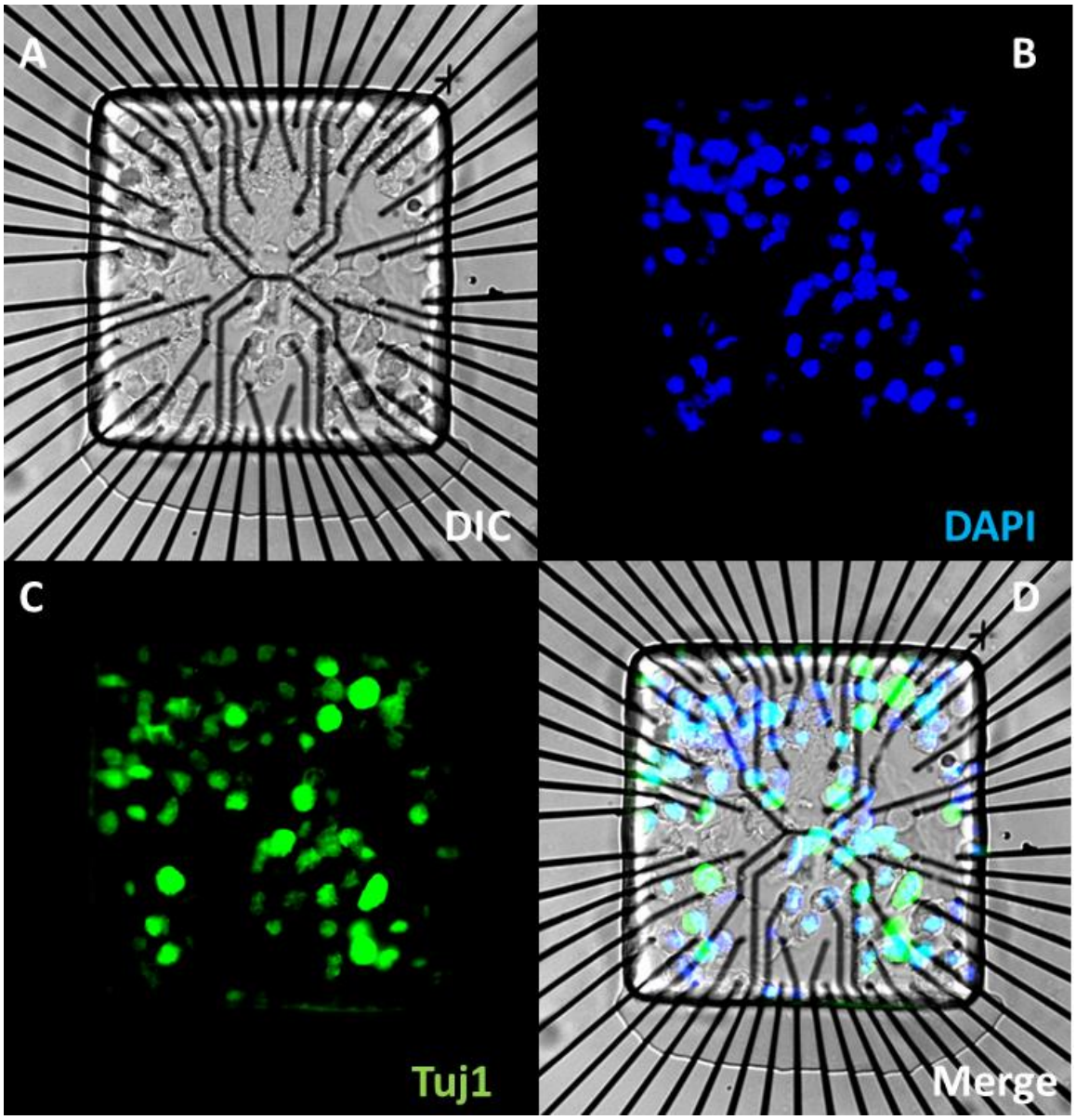

Figure 2.14 Images from immunocytochemistry analyses of rat cortical neurons fixed at DIV 15. The images have been taken with an Inverted IX81 Olympus Compound Fluorescence Microscope and a 60x objective. (A) Differential interference contrast (DIC) image. (B) DAPI nuclear staining. (C) The cells have been stained for Tuj1, a marker specific for neurons. (D) Merged image.

2.5 Modeling of the Electro-Neural Interface

Following the electro-physiological measurements, further analysis is required to retrieve the actual amplitude and time-scale of the recorded signals by removing signal degradation effects of the measurement device and system, particularly when the sensors themselves are capacitive. This procedure entails a) electrical modeling of the overall system in terms of electrical components - mainly resistors (R) and capacitors (C) - starting with the neuron cell membrane, the electrolyte/electrode interface, the electrode's parasitic components, and reaching the read-out electronics (**Figure 2.15**); b) signal processing by applying a deconvolution method to reverse the undesired filtration effects quantified by equivalent transfer function (TF) that is derived in the first step.

Starting with the neuron cell, the basic functional properties for the neuron's membrane during firing an AP, the signal of interest, can be modeled by resistors (R_{Na} and R_K representing the Na^+ and K^+ ion channels respectively), current sources (I_{Na} and I_K representing the Na^+ and K^+ ionic currents flow), and capacitor (C_m representing the lipid bilayer of the membrane), where (C_m~1 $\mu F/cm^2$). [26]

Upon culturing the neuron cells on the NW electrode's array, the interface with the recording electrode is formed. The quality of the interface (and essentially its electrical properties) is primarily determined by the specific cell-electrode engulfment configuration, which can be quantified by a seal resistance to ground (R_{seal}). Typically, R_{seal} ranges between 100 MΩ to a few GΩ.

The charge transfer across the interface (between the electrolyte and the electrode) is described by the electrochemical process at the tip of the electrode which boils down to a parallel RC branch.

C_{EC} represents the double layer capacitance, and R_{EC} represents the resistance for the Faradaic charge transfer process or the electrochemical redox reaction at the interface. R_{EC} and C_{EC} were determined from a three-terminal electrochemical impedance spectroscopy measurement of the NW electrode immersed in a saline solution described above (**Figure 2.15**). The values for R_{EC} and C_{EC} were found to be 65 MΩ and 8 pF. A stray capacitance (C_{stray}) representing the equivalent parasitic capacitance of the electrode is estimated to be ~ 80 pF. In addition, the input capacitance of the buffer amplifier (C_{amp}=5.5 pF) is added.

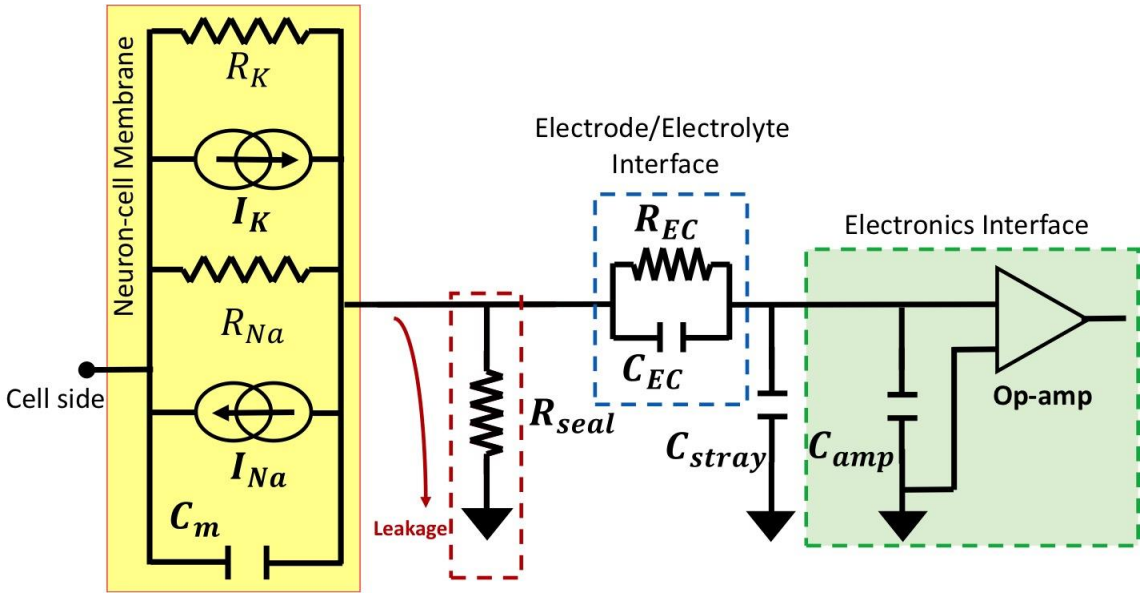

Figure 2.15 Equivalent Electrical Circuit Model for the Neural Recordings System. The circuit schematic starts with the neuron cell membrane showing the ionic currents (I_{Na} & I_K), the Sodium and Potassium ion channels represented by R_{Na} and R_K respectively, and the membrane capacitance C_m. The seal resistance (R_{seal}) defines the quality of the interface between the neuron cell membrane and NW electrode and therefore the amount of leakage/signal loss. The interfacial impedance of the electro-chemical reaction between the electrolyte and the electrode is represented by the parallel RC branch (R_{EC} & C_{EC}). The schematic includes also the parasitic capacitance which consists of the stray capacitance of the electrode (C_{stray}), in addition to the input capacitance of the buffer op-amp (C_{amp}).

First, examining the model qualitatively enables us to build an intuitive understanding for the overall behavior of the network and the main sources of loss in the electrical coupling. Looking

into the model, it can be noticed that the electrical coupling efficiency is impacted in two ways: (a) having a seal resistance creates a current divider in the electrical model, which leads to a significant loss in the measured signal especially in the situations where the cell engulfs the electrode loosely leading to a small R_{seal} values, (b) the parasitic components of the network form an equivalent low pass filter (LPF) with specific time constant (cut-off frequency) that leads to signal spreading. As the values of such parasitic components increase, the effective time constant gets larger and consequently the TF encounters a faster decay associated with higher attenuation (representing the 2nd source of loss in the coupling efficiency) as a result of decreasing the cut-off frequency leading to further spreading in the time scale.

Moving to quantitative analysis, the model is first verified by means of electrical simulations carried out using CADENCE circuit simulator. Typical patch-clamp measured Na^+ and K^+ currents profiles (sampled from similar cells) were used as input sources to the equivalent electrical circuit model (**Figure 2.16**). [27] The quantitative analysis is carried out by providing the specific values of each electrical component in the model based on the respective measurement/calculation. Upon adjusting the values for all the components in the electrical network, the model's accuracy was verified by comparing its output waveform against the measured signals where an excellent matching in both amplitude and time scale were achieved, as shown in **Figure 2.16 (d)** and **(i)**. A slight discrepancy was noticed though for some of the recordings which will be discussed in detail at the end of this section.

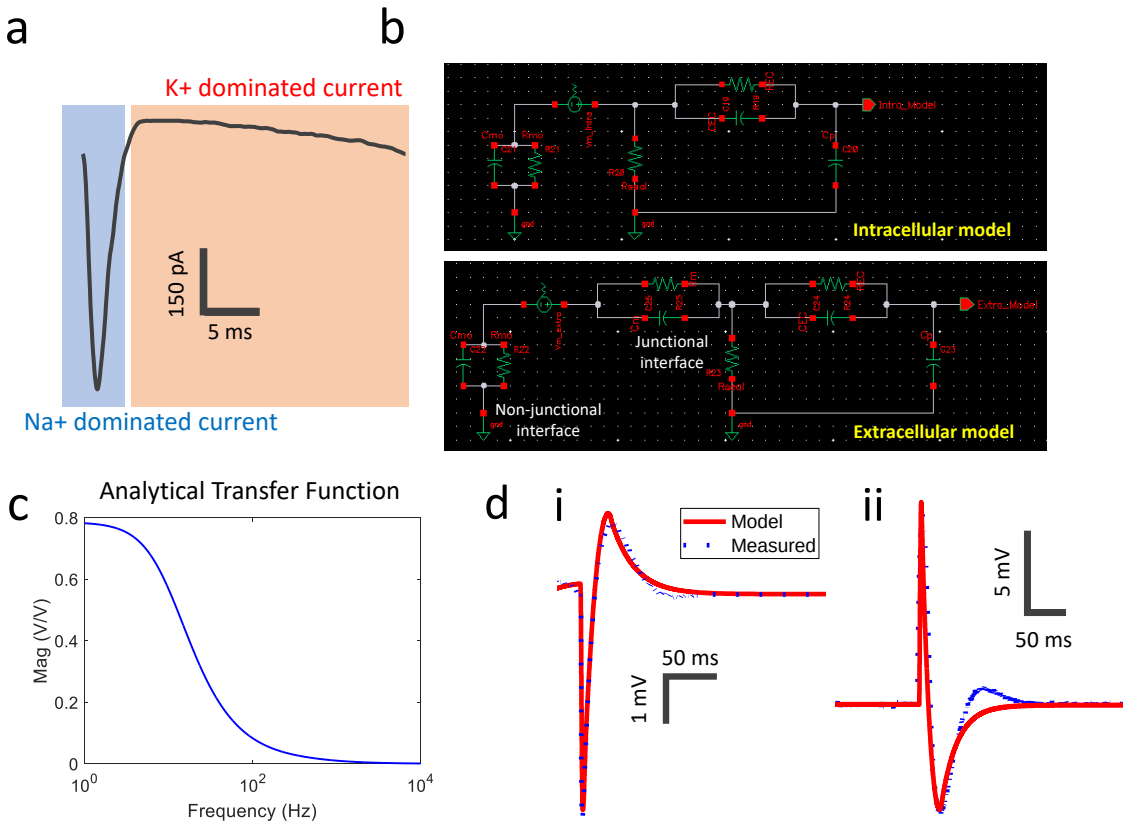

Figure 2.16 CAD Simulation of the Electrical Model on hiPSC-derived cortical neurons. (a) Typical patch-clamp measured Na^+ and K^+ currents samples [ref. 27] were used as input sources to examine the equivalent electrical circuit model in CAD simulation tool (CADENCE), this panel shows the net current assuming inward Na^+ current and outward K+ current. (b) Circuit schematic of the electrical model exported from CADENCE simulation tool (using current source to voltage source transformation) for both the intracellular and extracellular interfaces. (c) Sample intracellular transfer function describing the effect of the model on the measured signals. (d) Comparison between actual recorded APs and the equivalent electrical circuit model output based on typical input ionic currents, i. Extracellular, ii. Intracellular. The measurements were performed 6 weeks post in-vitro culture.

An analytical transfer function is then derived describing the impact of the model on the measured signals. For the intracellular case, using the equivalent model shown in **Figure 2.16**, it can be proved that:

$$TF = \frac{V_o}{V_{m,\ intra}} = H(S) = H_1 + H_2, \qquad (2\text{-}1)$$

$$H_1 = \frac{Z_{Cp}}{Z_{Cp}+Z_{EC}}, \tag{2-2}$$

$$H_2 = \frac{Z_{Cp}}{Z_{Cp}+Z_{EC}}\left[\frac{-1}{(1/Z_m\left(\frac{1}{R_{seal}}+\frac{1}{Z_{Cp}+Z_{EC}}\right)+1)}\right], \tag{2-3}$$

where Z_{Cp} is the impedance of the total parasitic capacitance, Z_{EC} the impedance of the electrochemical branch, and Z_m is the equivalent impedance of the cell membrane. A deconvolution algorithm (**Figure 2.18**) is used to reverse such effects quantified by a transfer function that leads to reliable retrieval of the original signals (**Figure 2.18**). The deconvolution process can be carried out in the frequency domain (FD) or time domain (TD). In FD, the algorithm starts by converting the measured signal into FD by performing Fourier Transform (FFT), then using the derived TF, the deconvoluted signal waveform is estimated. Finally, inverse Fourier Transform (iFFT) is performed to convert the deconvoluted signal into TD.

To account for the suspect variations within the NW electrode array, a transfer function is derived for each electrode capturing its specific interface and the associated parasitic components, and then the deconvolution process uses the corresponding TF for each channel recordings.

To investigate the multi-phase components of the measured action potentials, we remind that for a typical AP, the profile consists of two phases, the first is positive (crossing the equilibrium level upward) as a result of a depolarization due to the inward Na^+ current flow, and then a repolarization starts due the outward K^+ current flow leading to the hyperpolarization forming the second (negative) phase (crossing the equilibrium level downward). After that the potential gradually approaches the resting potential coming from the negative phase driving the cell back to equilibrium. It was noticed in our measurements that some recordings on some channels show a third phase in the measured signal profile where the potential crosses the

equilibrium level one more time upward forming a third (second positive) phase before resting. Using the above shown passive electrical model, such effect was not captured in the output response leaving some discrepancy with respect to those recordings with high peaking effect (**Figure 2.16 (d), ii**).

Careful characterization for the overall recording system including the NW electrodes was carried out. As shown in **Figure 2.17**, a train of square pulses is applied into a saline solution where the NW electrodes are immersed (without the presence of neuron cells) and interfaced with the rest of the measurement system. The system response to the characterization signal is recorded in the same way. Based on the input signal and output response, a transfer function is extracted. An empirical form can be shown as follows:

$$H(S) = \frac{86.02S+1103}{S^2+105.6S+1488} \quad (2\text{-}4)$$

The absolute of H(S) in FD along with the impulse response are shown in **Figure 2.17**. This technique provides a second experimental approach in deducing the system TF that can be used for signal retrieval similarly through the deconvolution algorithm as illustrated in **Figure 2.18**. Looking at the absolute of the experimentally estimated TF with frequency, a clear peaking effect can be noticed.

A potential implication of having such peaking effect is introducing extra oscillations in the response before going to equilibrium, which might justify having a third phase in some of the recorded signals before resting to equilibrium.

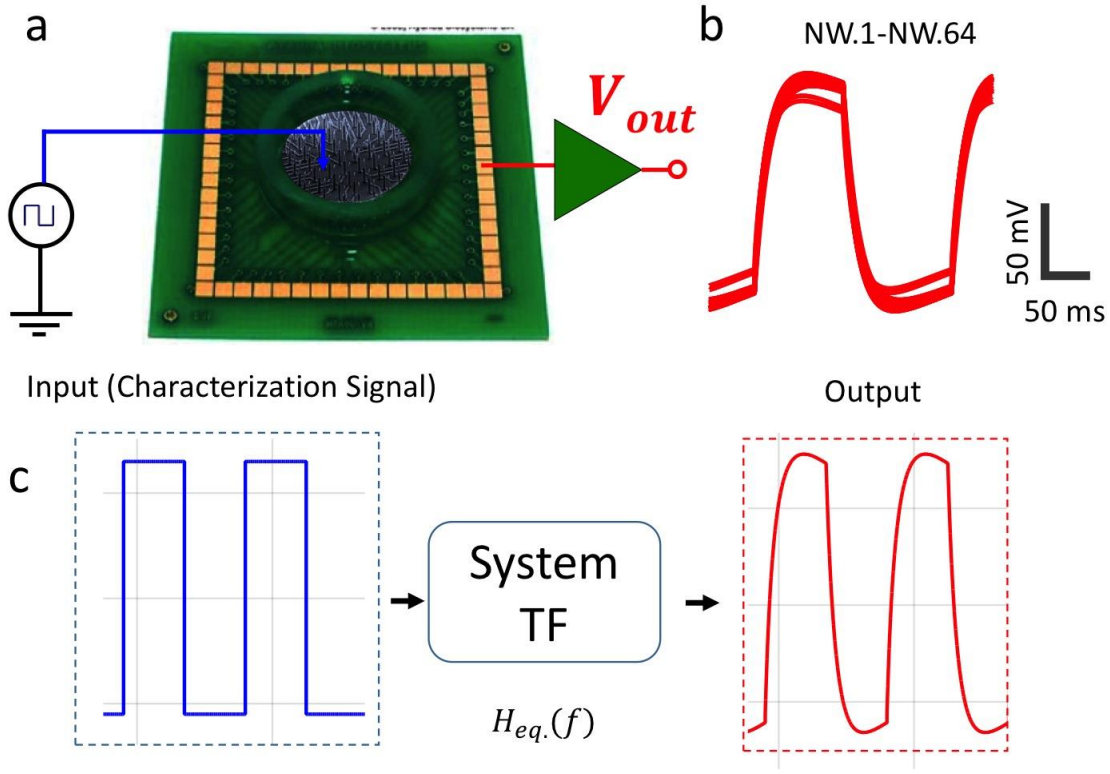

Figure 2.17 Characterization and Signal Processing. (a) Electrical response characterization setup showing the pulse generator is applied to the saline solution where the NW electrode array is immersed and attached to the measurement system from the other side emulating real recording session, (b) Recorded output of the characterization setup for multiple electrodes. (c) Block diagram illustrating the relation between the input characterization signal, the output signal and the desired TF.

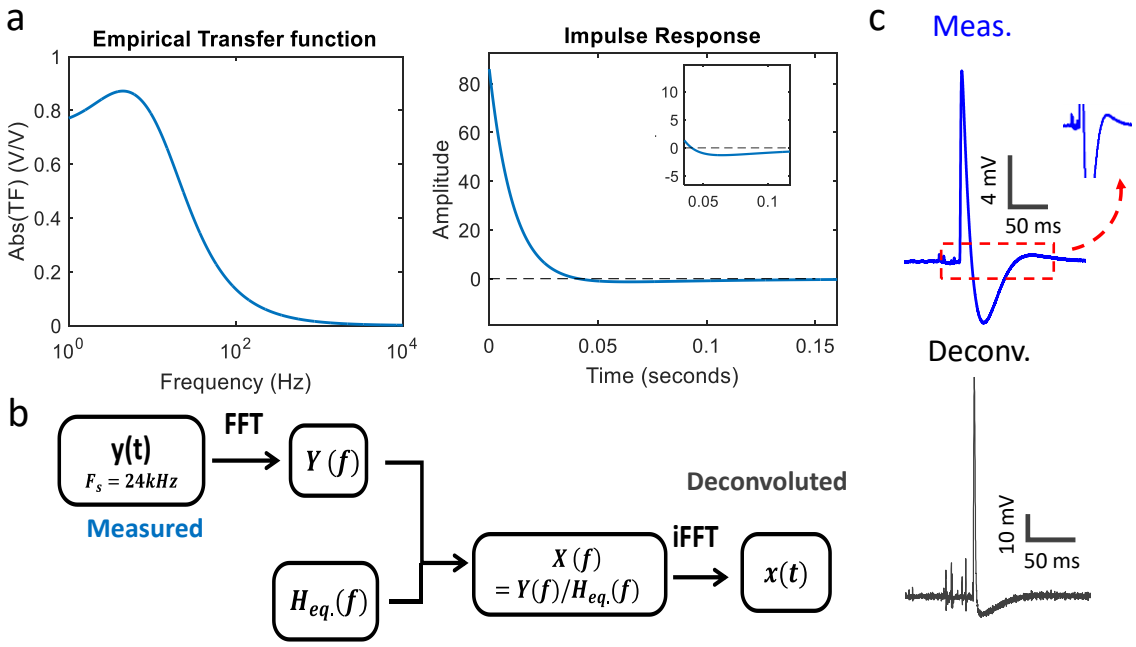

Figure 2.18 Extracted Transfer Function and Deconvolution Algorithm. (a) The absolute of the extracted TF with frequency showing peaking effect, the right panel is the impulse response showing the time domain representation. (b) Block diagram illustrating the general deconvolution algorithm in FD, (c) Sample measured intracellular signal from mouse hippocampal neuron 8 days post in-vitro culture showing extra oscillation prior to resting and deconvoluted result using the extracted TF shown below where we can notice the overshoot effect is disappeared.

2.6 Results and Discussion

To measure minute potential changes in individual cells in neuronal networks, it is important to develop an integration scheme for high-density individually electrically addressable out-of-plane nanowire neuronal probes. To achieve very high densities of individual nanowires that are suitable for mapping individual units in neuronal networks, we devised a novel all solid-state wafer bonding integration scheme on patterned Ni electrical contacts and leads (**Figure 2.19, Figure 2.1** and **Figure 2.2**) [29] leading to a superior high-density nanowire-neuron interface platform. This bonding scheme is essential because conventional low temperature eutectic bonding does not provide the lead-to-lead electrical isolation necessary for individual electrical

addressability of single sites in a high-density nanowire array. [30] Instead, we utilize the thermally-driven solid-state diffusion of Ni into Si at a low temperature (400 °C), traditionally used to make self-aligned contacts for transistors in the semiconductor industry, [31] to bond Si substrates to optically transparent and electrically insulating sapphire substrates that were pre-defined with Ni patterns. By doing so, we achieve two goals with the Ni layer: (1) bonding and fusion of a thin (~50 μm) Si substrate to the underlying host substrate, and (2) embedding electrical leads underneath active or passive Si components in the bonded substrate with low contact resistance (**Figure 2.1**). The integration technique is general to any other substrate that can sustain the NiSi reaction temperature (starts at 300°C), including complementary metal oxide semiconductor (CMOS) integrated circuits and advanced planar [32-33] and out of plane device geometries are attainable through this method. Additionally, the optical transparency of sapphire enables light excitation and transmission imaging degrees of freedom in our platform. Overall, the integration technology developed in this work is the first to enable electrical addressability for individual vertically standing nanowires registered precisely over underlying metal leads. This individual electrical addressability of nanowires has potential to enable precise measurements of activity of individual units in neuronal networks, and to detect miniature release of neurotransmitters, especially important for investigating the synaptic properties of networks of neurons in the context of neurological diseases, as for the characterization of pre- or post- synaptic defects based on amplitude or frequency modifications in the subthreshold postsynaptic potentials.[34-35]

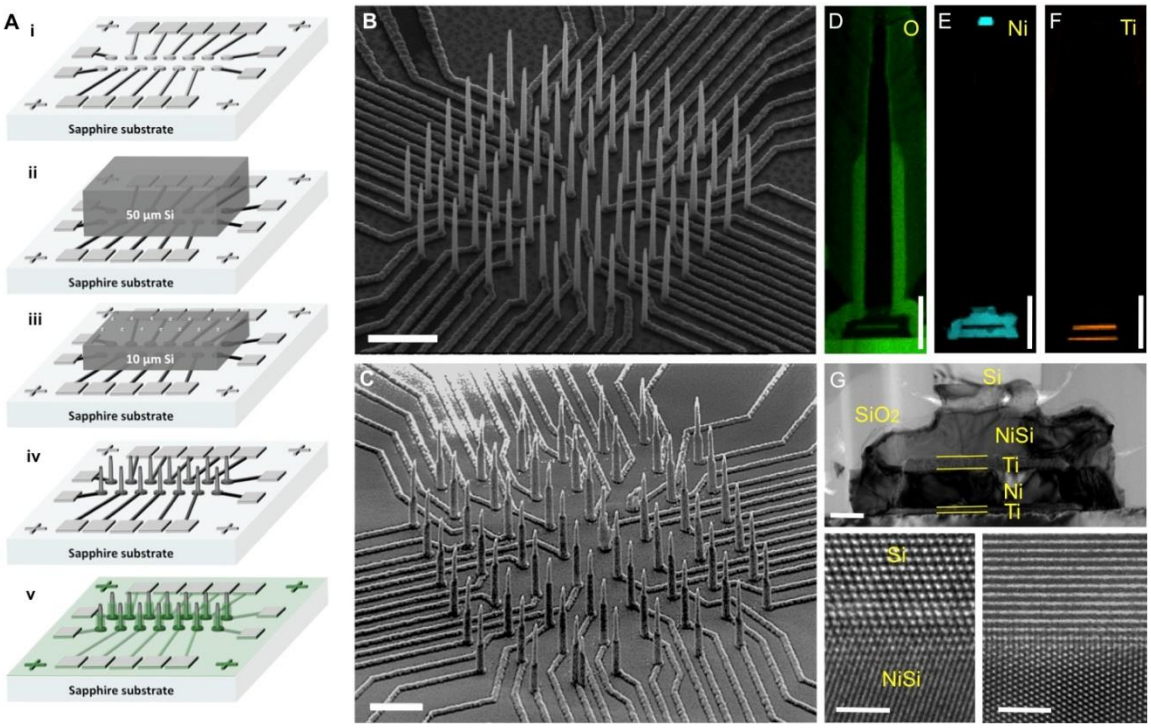

Figure 2.19 (A) Illustration of fabrication procedure for high density electrically isolated nanowire probes by solid-state wafer bonding. i. Metal stack with Ni top-most layer is patterned by a combination of photolithography and electron beam lithography atop an electrically insulating and transparent sapphire substrate. ii. Si is bonded to the substrate in (i) by nickel silicidation. iii. The Si wafer is thinned down to the desired wire height. Ni masks are then defined by electron beam lithography and aligned to the bottom plane Ni pattern. iv Si nanowires are etched by an SF6/C4F8 plasma etch step. v. SiO2 PECVD is then deposited and is selectively etched to expose the tips of the Si nanowires. (B-C) SEM images of an 8 × 8 Si nanowire array after etching (B), and (C) after SiO2 passivation. Scale bar in (B) is 5μm and in (C) is 3μm. (D-E). Energy-dispersive x-ray spectroscopy (EDX) of the oxygen (D) signature of the SiO2 passivation layer, nickel (E) for etching mask (top), NiSi region, and conducting lower most layer, and Ti (F) as the diffusion barrier (top) and adhesion layer (bottom). Scale bars are 1 μm. (G) High magnification TEM image of the NiSi/Ti/Ni/Ti underneath the Si nanowire highlighting the interfacial structure between the bottom conducting lead and the Si nanowire. Scale bar is 200nm. The bottom panels are HRTEM images at the interface between Si and NiSi with electron beam axis aligned in the Si $[1\bar{1}0]$ (left panel), and the NiSi $[1\bar{1}0]$ Zone axis in (right panel) to display the crystalline interface. Scale bars in bottom panels are 2 nm.

Fabrication of our in-vitro platform starts with photolithography and e-beam lithography (EBL) patterning of electrode leads on a sapphire substrate, as shown schematically in **Figure 2.19 (a)-i**. [36] The electrode leads have metal stacking of Ti/Ni/Ti/Ni (30nm/200nm/50nm/200nm) for adhesion/conduction/diffusion-barrier/silicidation purposes, respectively. When a thin Si chip,

5mm×5mm×50μm, is brought into contact with the metal leads on the sapphire substrate, a moderate heat treatment (400 °C) and compressive pressure (around 10 MPa) in a vacuum chamber with forming gas (H_2 3-3.8% in N_2) flow initiates a diffusion reaction between Ni and Si. The formed NiSi alloy fuses the two substrates together (**Figure 2.19 A** -ii). 400 °C was chosen because it led to reacted NiSi leads that formed ohmic-like contacts with the heavily doped Si (**Figure 2.1** and **Figure 2.2**). The height of the desired nanowire array can be adjusted by an SF_6 inductively coupled plasma (ICP) and reactive ion etch (RIE) that thins the Si substrate to around 8 – 10 μm (**Figure 2.19 A**-iii).

Another electron-beam lithography step patterns Ni etch mask dots aligned exactly at the tips of the Ni leads underneath the Si substrate (**Figure 2.19 A** -iii). An SF_6/C_4F_8 based ICP/RIE process is used to etch the Si everywhere except regions masked by the Ni dots, leaving vertically standing Si nanowires on NiSi leads (**Figure 2.19 A** -iv and **Figure 2.19 B**) which have diameters in the range of 100-200nm in this work. To prevent electrochemical reactions anywhere except at the nanowire tips, the entire chip is coated by SiO_2 which is then selectively etched at the contact pads and nanowire tips (**Figure 2.19 A**-v, **Figure 2.19 C**). The scanning electron microscope (SEM) images of the Si nanowire arrays in **Figure 2.19 B** and **Figure 2.19 C** demonstrate a high packing density of 6.25 Million/cm^2 at a pitch of 4 μm. We also demonstrated sub-micrometer pitch at a site-to-site spacing of 750 nm (**Figure 2.3**). The array geometry can be tailored for the optimal growth of neuronal networks [37] that are interconnected with sealed microfluidic channels that can allow growth of neurites and synaptic connections but prevent cell-body plating inside the channels (**Figure 2.5** and **Figure 2.6**). The electrochemical impedance in all of these configurations is relatively uniform (**Figure 2.5** and **Figure 2.6**) and validated a capacitively dominant coupling behavior (phase in **Figure 2.8**) with neuronal activity.

Transmission electron microscopy (TEM) and elemental mapping by energy-dispersive X-ray spectroscopy (EDX) of the Si nanowires demonstrate crystalline structures and interfaces and highlight the usefulness of each layer: Si constitutes the main body of the sensor, SiO_2 constitutes the passivation outermost cylinder around the bottom portion of the nanowire (**Figure 2.19 D**), Ni is used for silicidation bonding and as a current conduction layer (**Figure 2.19 A** top and bottom, respectively), and Ti is used as a Ni diffusion barrier and adhesion layer (**Figure 2.19 F** top and bottom, respectively). A zoomed-in TEM image at the bottom of the wire in **Figure 2.9 G** highlights the interfacial layers crucial for the free standing and individually electrically addressable nature of the Si nanowire. The high-resolution TEM (HRTEM) images in the lower panels of **Figure 2.19 G** illustrate the crystalline nature of the interface between NiSi and Si at the bottom of the wire (see also **Figure 2.9**). Similar bonding structure, morphology, and interfaces were validated on SiO_2/Si substrates illustrating the versatility of our bonding scheme.

We next investigated the biological interfaces established between our Si nanowires and neurons and the resulting recorded electrophysiological activity. We packaged our devices on commercial electrophysiology printed circuit boards (**Figure 2.7**) and tested their feasibility for electrophysiology and pharmacology using rodent hippocampal primary neurons and human iPSC-derived neurons. For both rodent primary and hiPSC-derived neurons, we find strong interaction between neurons and nanowires characterized by cell outgrowth and engulfment to the vertical Si nanowires (**Figure 2.20 A**, primary mouse neurons; **Figure 2.22 C**, hiPSC-derived neurons). The cell-electrode interface is generally established in intracellular and extracellular configurations both of which can provide sufficient coupling between the cell and the electrode to enable high fidelity recordings.

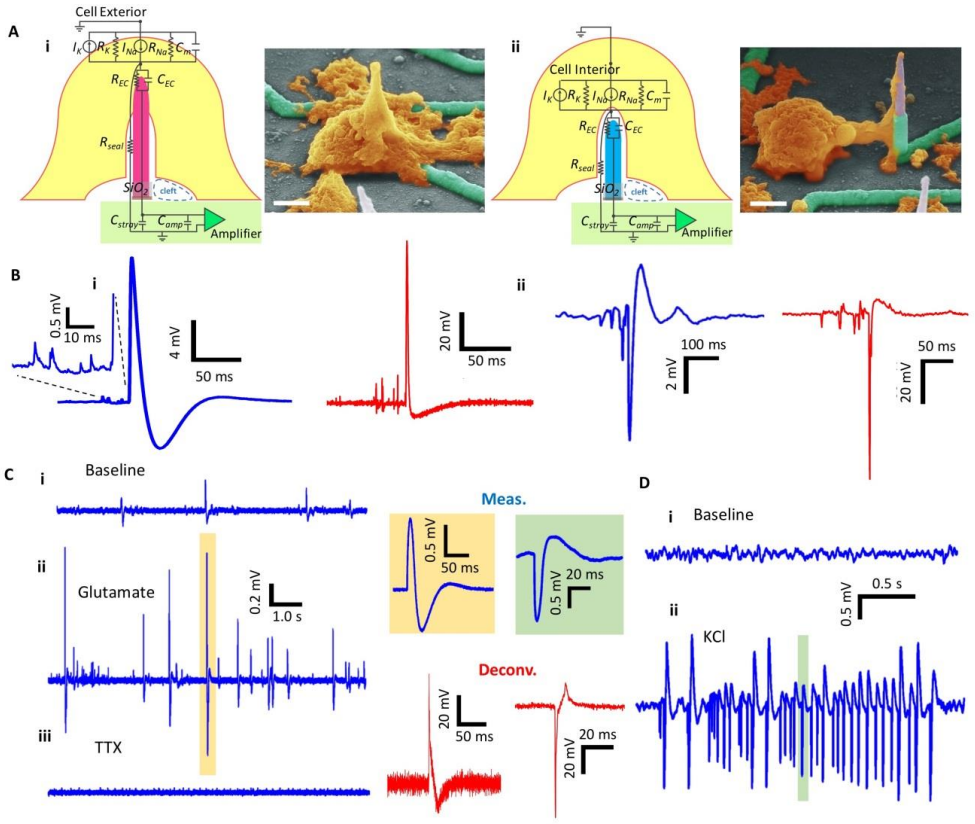

Figure 2.20 Modeling/ Characterization/ Measurement of the electro-neural system on mouse hippocampal neurons. A. The electrical circuit models and corresponding SEM images of the electrode-cell engulfment, i. Intracellular electrode configuration. ii. Extracellular electrode configuration. The electrical circuit model of the electro-neural system starts by the cell culture (yellow) interfacing with the electrode, all the way to the read-out electronics represented by the amplifier block (green). I_{Na} and I_K represents the Na^+ and K^+ ionic currents, and R_{Na} and R_K are the corresponding ion channel resistances. R_{seal} is the seal resistance at the cell-nanowire interface. REC represents the resistance of the electrochemical reaction at the electrode tip, and C_{EC} is the double layer capacitance. C_{stray}, C_{amp} are the bare electrode wire and amplifier's input parasitic capacitances respectively. B. Spontaneous action potentials recorded on mouse hippocampal neurons. i. Recordings showing the positive measured signal (~20 mV p-p) (left in blue) and after deconvolution (right in red). ii. Recordings showing the negative measured signal (~10 mV p-p). Small potential fluctuations were captured in both cases. C. Effect of external application of glutamate/ TTX to the recording solution. i. Baseline recordings showing the normal cell firing activity. ii. After addition of 196µM Glutamate to the recording solution, increased activity is observed. A sample action potential is shown on the right (blue), and its deconvoluted potential is shown below (red). iii. After the application of 1.5µM TTX, the cell activity is blocked. D. Effect of addition of 13.2 mM KCl to the recording solution i. Baseline recording showing very quiet cell activity. ii. Following the application of KCl, increased cell activity was observed with a train of action potentials. Similarly, sample action potential is shown on the left (blue), and its deconvolution is shown below (red). Electrophysiology was performed at DIV 8.

The amplitude and shape of recorded potentials are governed by the electrochemical interface at the surface of the nanowire and the degree of sealing for the cell membrane to the nanowire itself, and by the measurement system.[38-40] To account for these effects in both intracellular and extracellular configurations (**Figure 2.20 A**), we developed a circuit model based on experimental measurements for each component of the electrode/neuron interface. Results using analytic transfer functions, circuit simulations, and empirical transfer functions for the overall measurement system provided excellent agreement with the measured potentials.

One of the main signatures of our model is the use of current source and different conductance for the Na^+ and K^+ channels that is commensurate to the physical origin of the faster depolarization and repolarization in action potentials. These were calibrated to patch-clamp measured inward and outward ionic currents from similar cultured cells (**Figure 2.17 (a)**). The longer duration of the patch-clamp action potentials has been previously related to maturity, health and exact temperature of the cell culture for both hiPSC [41] and rodent cortical neurons [42] which was also observed in our reference patch-clamp measurements (**Figure 2.17 (a)**). We propose that our electrophysiological models using either analog circuit analysis or empirical simulations based on detailed electrochemical characterization, similar to the models of Spira et al. [38-40] are self-consistent models that can accurately reproduce both the time and the amplitude of deconvoluted neuronal signals measured from nanowires.

Pharmacological stimulation and inhibition validated the physiological origin of the measured potentials. After adding glutamate to the recording solution, we observed an increase of the cell spontaneous activity (**Figure 2.20 C**-ii) with respect to frequency and amplitude when compared to the baseline (**Figure 2.20 C**-i) measured on the same channel. The bath application of tetrodotoxin (TTX) inhibited the activity on the same channel (**Figure 2.20 C**-iii). Similarly,

for the extracellular configuration, the bath application of KCl led to increased activity (**Figure 2.20 D**-ii) relative to the baseline recording (**Figure 2.20 D**-i) which was also eliminated by TTX treatment.

Strikingly, physiological measurements on mouse hippocampal neurons cultured for 10-13 days on our platform displayed small potential fluctuations prior to the positive (**Figure 2.20 B**-i) and negative (**Figure 2.20 B**-ii) firing events. The SNR of these pre-spike potentials is 20X as evident in the inset of **Figure 2.20 B**-i and their shape is clearly different from coupled action potentials from different cells or channels. The largest action potentials that we measured 10 DIV is 99 mV, as shown in **Figure 2.21 A**, which demonstrates for the first time that nanowires can measure intracellular potentials with similar magnitudes to that of patch-clamp. We generally observed oscillations prior to spikes as highlighted in the insets of **Figure 2.21 A**. For a simultaneously measured extracellular potential from another channel (**Figure 2.21 B**) that is 5.65 μm apart from the intracellular channel, we also observed potential oscillations prior to the extracellular spike. Upon inspecting all other channels, we did not observe action potentials that might be electronically coupled to these two channels. We then embarked on validating that these potential oscillations are subthreshold synaptic potentials. To do so, we pharmacologically blocked both excitatory and inhibitory receptors by adding D-APV to block NMDA receptors, CNQX for blocking AMPA receptors and Picrotoxin for preventing the binding of the inhibitory neurotransmitter GABA to its receptors. After adding the blockers we observed statistically insignificant pre-spike small oscillations (**Figure 2.21 C**) or no oscillations (**Figure 2.21 D**), suggesting that our system has the sensitivity to detect miniature release of neurotransmitters at a quantal level. Given that our nanowires can sometimes measure intracellular potentials with an SNR of 1700 (**Figure 2.21 A**), it is not surprising that they can also resolve subthreshold activity

that we validate with standard pharmacological experiments here. This can be attributed to the height of our nanowires, which is > 6.5 μm compared to the shorter than 2 μm nanowires in prior works, providing larger Si surface interaction area with adherent neurons.

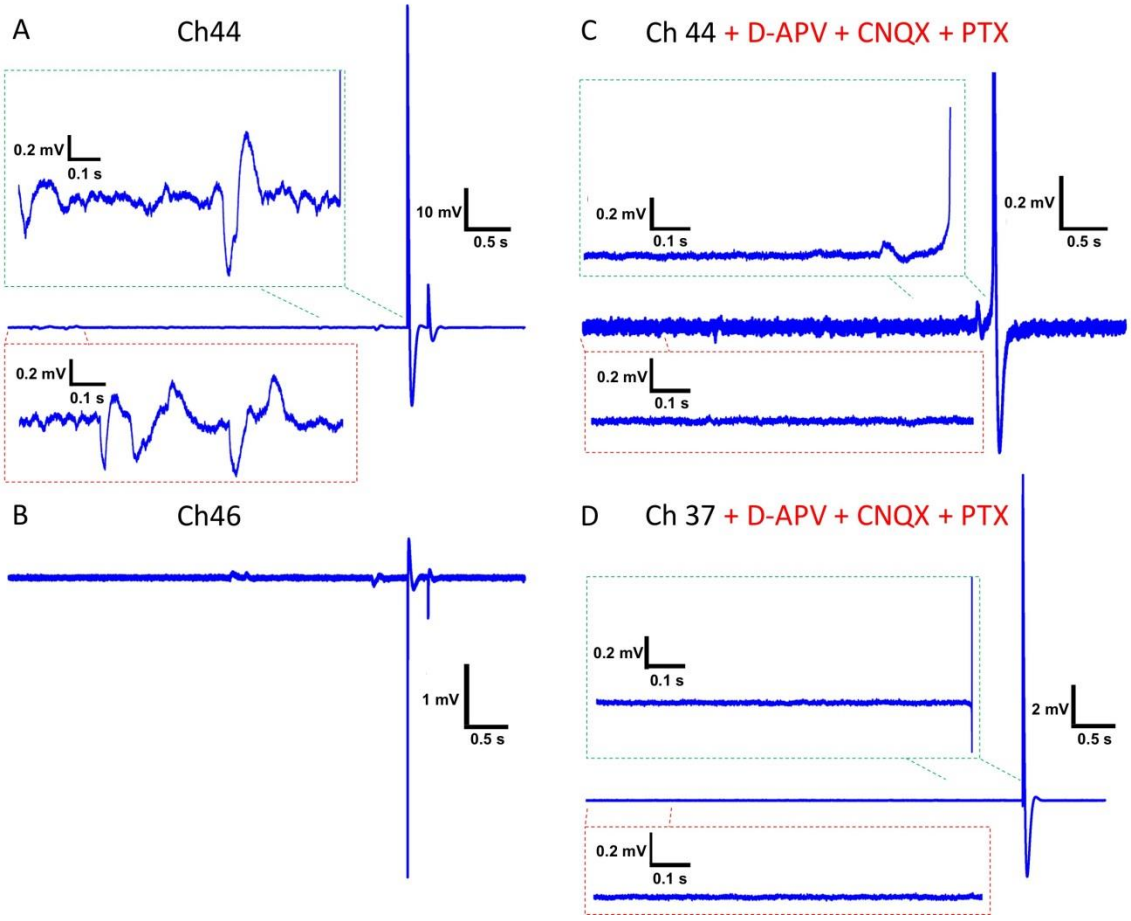

Figure 2.21 Recording of a 99mV Action Potential and Pharmacological experiments for validating subthreshold potentials at DIV 10. A. Spontaneous activity measured on channel 44 showing subthreshold oscillations that are illustrated in the insets of a 1sec time window at the beginning of the trace (lower inset) and just at the action potential generation (top inset). B. Concurrent recording with A from a nearby channel 46 showing some potential oscillations and negative spikes that occur simultaneously with those in A. C. Recording with a solution containing D-APV (50μM), CNQX (10μM) and PTX (1mM) to block NMDA, AMPA, and GABA receptors respectively, shows a single oscillation prior to the spike on the same channel as in A. D. Same in C from channel 37 showing no oscillations prior to the large AP.

The development of high-throughput, sub-cellular neurotechnologies have the potential for application to drug screening on neurological disease models. We therefore tested the sensitivity of our platform with two clinically relevant subtypes of human iPSC-derived neurons, cortical and dopaminergic, for which we had demonstrated electrical activity on conventional microelectrode array recordings (**Figure 2.13**).

Human iPSC-derived cortical neurons cultured on our platform overlapped with multiple nanowires (**Figure 2.22 A**). Post preparation for SEM on this platform, evidence of neurite outgrowth to nearby nanowires is also apparent in **Figure 2.22 A**. Nanowires 7 & 8 displayed positive action potentials whereas nanowire 6 displayed a negative action potential (**Figure 2.22 B**). From the SEM image of **Figure 2.22 A**, we can note the extracellular nature of the interface with nanowire 6. To uncover the nature of the nanowire/neuron interaction for nanowires 7 & 8, we performed a sequential focused ion beam (FIB) cut and thinning of a 300-400nm slice on the sample in regions of wires marked 6,7,8 (**Figure 2.11** and **Figure 2.12**) post Pt plating. The sample is thin enough to allow electron transmission for TEM characterization without risking significant damage to the cell body during the FIB milling process. Fig. **Figure 2.22 C** shows an SEM image of the FIB slice showing a clear dark contrast of the cell around nanowires 7 & 8. The TEM images in **Figure 2.22 D** and **Figure 2.22 E** along the substrate-nanowire-cell regions demonstrated that the nanowires displayed intimate interaction with neurons that is not aided by tension due to neuron adhesion and spreading on the substrate surface or peptide-modification, [43-45] nor assisted with the highly invasive electroporation. [9-10]. The continuity of the inclined interface below the SiO_2

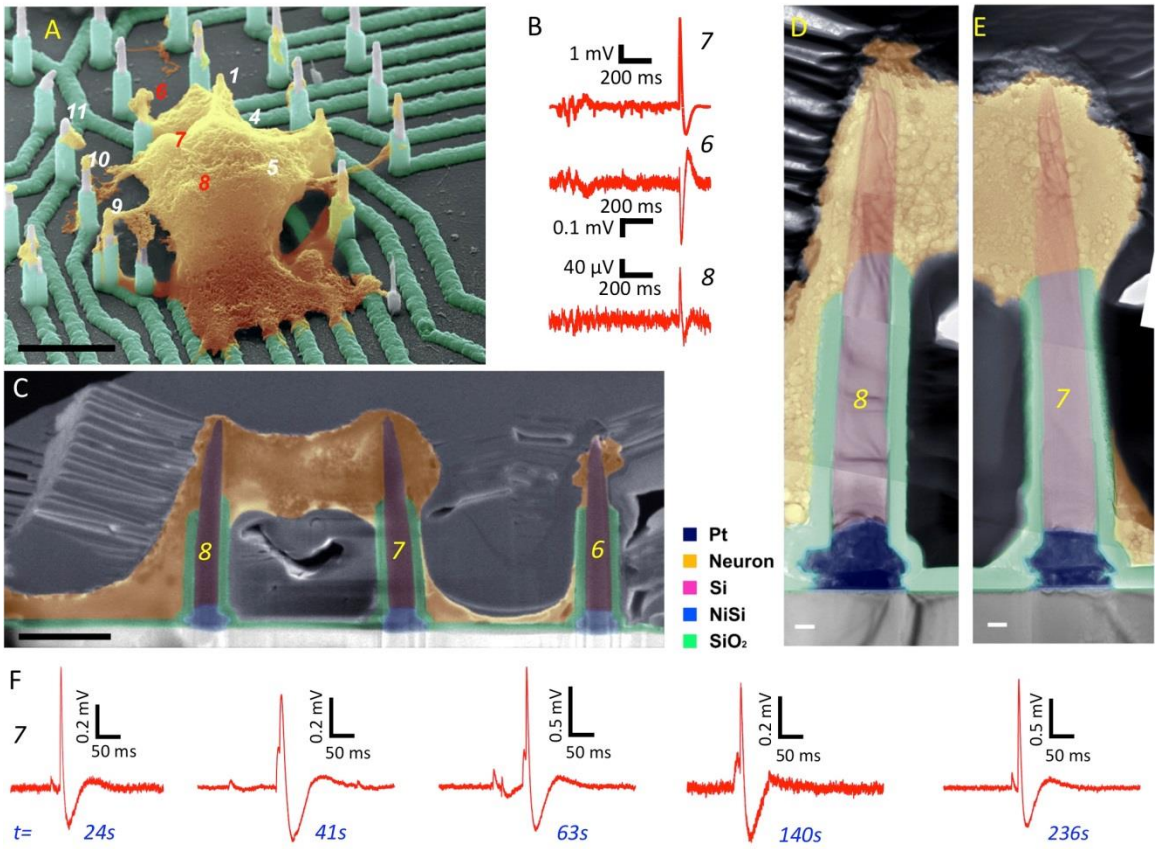

Figure 2.22 Recording from hiPSC-derived cortical neurons. A. Colorized angle-view SEM image showing cell morphology and neurite outgrowth to nearby nanowires. Scale bar is 4 µm. B. Measured potentials on channels 6-8 showing positive potentials for wires 7&8 inside the cell and negative potential for wire 6 outside the cell. C. Colorized SEM image of the Pt coated and FIB thinned cross-section of the cell in panel B. The image shows the cell (dark contrast) engulfing the tops of nanowires 7 & 8, and portions of cell membrane around nanowire 6. Scale bar is 2µm. Electrophysiology was performed 6 weeks post in vitro culture. D-E Higher magnification colorized TEM images collected and stacked to provide a higher resolution close-up to the nanowire-cell interface. The slight bending of the nanowires is likely to have happened during neuron dehydration in preparation for SEM imaging (section 5 of Supplementary Materials). Scale bars are 200 nm. F. Recordings on nanowire number 7 illustrating consistent oscillations prior to action potential firing at different recording times.

passivation layer as seen to the right of the nanowires in **Figure 2.22 D** and **Figure 2.22 E** are suggestive of intracellular penetration of the nanowires into the human cortical neuron cell body which is commensurate with the positive potentials measured with wires 7&8. [46] But it is also

possible that the cell fixation and FIB thinning can lead to artifacts in the observed interface. Also in these recordings, we observed the pre-spike potentials with sharp rise and slow decay times, which are similar in shape to the excitatory post-synaptic potentials (EPSPs) observed by Hai et al. using Au mushroom electrodes. [47] It is possible however that the positive potentials are measured in a extracellular configuration due to their smaller amplitude than those observed in **Figure 2.20, 2.21,** and **2.23**, since we did not validate their nature by blocking the postsynaptic receptors. We note that out of the two hiPSC cells on top of the nanowire array, we measured positive potentials from one neuron. The individually addressable nanowires can record multiple positive potentials from a single neuron.

Dopaminergic neurons are a clinically relevant cell type for study of neurodegenerative disease and neuropsychiatric disorders. We determined whether hiPSC-derived dopaminergic neurons could also survive and demonstrate physiological function on our nanowire device. Six weeks post-plating hiPSC-derived dopaminergic neurons on the nanowire platform, we observed distinctive single slope rise potentials compared to the multi-oscillation behavior exhibited by the mouse hippocampal neurons and hiPSC-derived cortical neurons prior to spontaneous action potential firing for both positive and negative polarities (inset, **Figure 2.23 A**). On some channels, we observed small potential oscillations with varying frequency and amplitude as shown **Figure 2.23 B**. We then performed pharmacological studies after two weeks post-astrocyte co-culture on the hiPSC-derived dopaminergic neurons (6 weeks post initial culture). Upon bath application of KCl, the firing rate increased and then all activity stopped after the addition of TTX as shown in **Figure 2.23 C**. In conclusion, hiPSC-derived neurons not only survived several weeks intimately interfaced with the nanowires, but we also observed extensive electrophysiological activity over

time, leading to the possibility of longitudinal electrophysiological experiments on synaptic activity on in-vitro human neuronal networks.

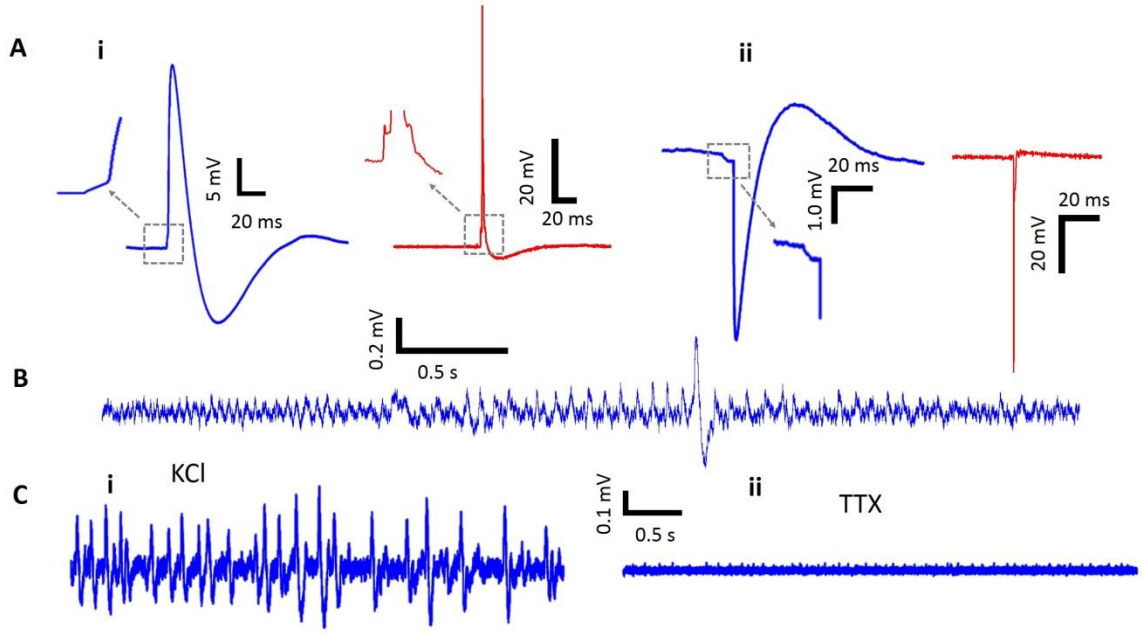

Figure 2.23 Recording from hiPSC-derived dopaminergic neurons 6 weeks post in-vitro culture. A. Spontaneous action potentials. i. Positive potential recordings showing the measured signal (~30mV p-p) (left in blue) and after deconvolution (right in red). ii. Negative potential recordings (~6mV p-p) (left in blue) and after deconvolution (right in red). B. Potential oscillations recorded prior to action potential firing. C. Effect of external application of stimulating/inhibiting media. i. Increase of action potential firing following 13.2mM KCl bath application. ii. The increased activity abolished after the application of 1 μM TTX.

The electrophysiological recordings from our cultures did not display trains of large action potentials, but just one or two APs, which is consistent with recordings from immature neurons and network observed on both human and rodent cultures from other groups. [41, 48] Therefore, we performed immunocytochemistry analyses on primary neurons cultured on our platform. The rat cortical neurons fixed at DIV 15 showed that the cells are well adherent to the nanowire arrays, stained positive for Tuj1, a specific neuronal marker, with some limited neurite extension. (**Figure**

2.14) The normal formation of a mature neuronal network can be compromised by the height of our nanowires that pin the cells above the planar regions of the platform. This can be improved by creating 3D islands at the bottom of the nanowires that can promote network connectivity on a 3D surface. In the extreme case of shortening the nanowires to heights that are similar to that is reported previously, the intracellular capability of the nanowires might be compromised. Increasing the spacing between the nanowires may also strengthen the network activity of the culture as noted in the recent work of Shmoel et al [49] but will compromise their density. Further investigation of the limited neurite extension in our cell culture will lead to improved network synaptic connections and to more robust and consistent measurements of action potentials and PSPs. (**Figure 2.20-2.22**).

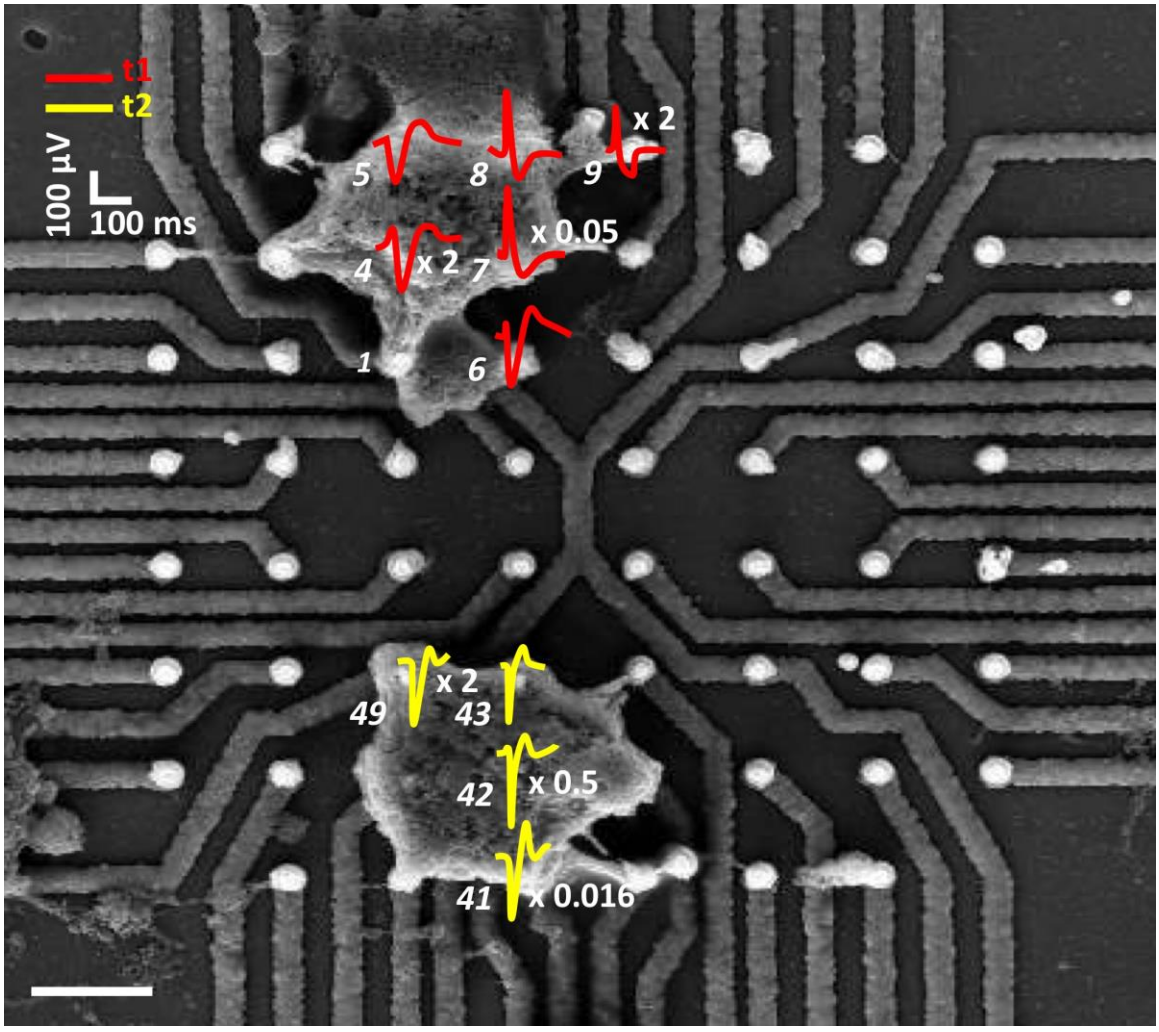

Figure 2.24. Top-view SEM image of the overall device with two hiPSC-derived cortical neurons measured 2 weeks post in-vitro culture with measured signals that have signals above noise level overlaid on the respective nanowires. We did not observe simultaneous spiking in the two cells for these two neurons, and therefore the measured potentials are displayed at two different times. The scale bar in 4µm.

It is also important to report our primary rodent neuron experiments were conducted on 5 devices with successful measurements for several days for both intracellular-like and extracellular-like potentials on 4 out of the 5 devices. The measured intracellular-like potentials varied from 0.1 mV to 99 mV. The hiPSC experiments, were conducted on 4 devices with successful measurements for several days for both intracellular-like and extracellular-like potentials on 4 out

of the 5 sets, and for one device over several weeks (4 weeks and then 6 weeks after culture). The measured intracellular-like potentials varied from 0.1 mV to 35 mV. From **Figure 2.24**, we can observe 2 cells in the 28μm × 28μm square array of nanowires leading to a cell density of ~ 255,100 cells/cm^2. One can also observe from **Figure 2.24** that 2 out of the 12 nanowires in contact with the cultured cells resulted in intracellular-like measurements. As observed by other groups the variability of the Amplitude and duration of APs can be due to different engulfment level or cleft width between the neuron and the nanowire. [49] The yield on nanowire internalization to cells can also be improved, for example with peptide modification. [45]

Measurement of intracellular action potentials using individually-addressable Si nanowire probes, from both mouse and human neurons, opens new prospects on mapping neuronal activity in large networks, while the sensitivity to subthreshold postsynaptic potentials from multiple neurons opens new possibilities to study synaptic transmission mechanisms and plasticity, particularly important for investigating neurological diseases. Given the scalability of our arrays, the simultaneous recording of minute changes in cell potentials can uncover details on the synthesis, processing, and execution of neuronal network activity. In vitro, highly parallel drug screening experiments can be performed using the human relevant iPSC cell line and without the need of the laborious non-scalable patch-clamp. In vivo, targeted modulation of individual neural circuits or even single cells within a network becomes possible, and implications for bridging or repairing networks in neurologically affected regions becomes within reach. Overall, our platform and modified versions thereof have the potential to lead to transformative technologies for both in vivo and in vitro applications.

Chapter 2, in full, is a reprint of material as it appears in the following publication: R. Liu, R. Chen, A. T. Elthakeb, S. H. Lee, S. Hinckley, M. L. Khraiche, J. Scott, D. Pre, Y. Hwang, A.

Tanaka, Y. G. Ro, A. K. Matsushita, X. Dai, C. Soci, S. Biesmans, A. James, J. Nogan, K. L. Jungjohann, D. V. Pete, D. B. Webb, Y. Zou, A. G. Bang and S. A. Dayeh, "High Density Individually Addressable Nanowire Arrays Record Intracellular Activity from Primary Rodent and Human Stem Cell Derived Neurons" Nano Lett. 17 (5), 2757-2764 (2017). The dissertation author is the first author of this paper.

2.7 References

1. W.Kim, J. K. Ng, M. E. Kunitake, B. R. Conklin, P. Yang, Interfacing silicon nanowires with mammalian cells. Journal of the American Chemical Society 2007, 129 (23), 7228-7229.

2. G. Piret, M.-T. Perez, C. N. Prinz, Neurite outgrowth and synaptophysin expression of postnatal CNS neurons on GaP nanowire arrays in long-term retinal cell culture. Biomaterials 2013, 34 (4), 875-887.

3. L. Hanson, Z. C. Lin, C. Xie, Y. Cui, B. Cui, Characterization of the cell–nanopillar interface by transmission electron microscopy. Nano letters 2012, 12 (11), 5815-5820.

4. L. Gällentoft, L. M. Pettersson, N. Danielsen, J. Schouenborg, C. N. Prinz, C. E. Linsmeier, Size-dependent long-term tissue response to biostable nanowires in the brain. Biomaterials 2015, 42, 172-183.

5. F. Patolsky, B. P. Timko, G. Yu, Y. Fang, A. B. Greytak, G. Zheng, C. M. Lieber, Detection, stimulation, and inhibition of neuronal signals with high-density nanowire transistor arrays. Science 2006, 313 (5790), 1100-1104.

6. T. Cohen-Karni, Q. Qing, Q. Li, Y. Fang, C. M. Lieber, Graphene and nanowire transistors for cellular interfaces and electrical recording. Nano letters 2010, 10 (3), 1098-1102.

7. X. Duan, R. Gao, P. Xie, T. Cohen-Karni, Q. Qing, H. S. Choe, B. Tian, X. Jiang, C. M. Lieber, Intracellular recordings of action potentials by an extracellular nanoscale field-effect transistor. Nature nanotechnology 2012, 7 (3), 174-179.

8. B. Tian, T. Cohen-Karni, Q. Qing, X. Duan, P. Xie, C. M. Lieber, Three-dimensional, flexible nanoscale field-effect transistors as localized bioprobes. Science 2010, 329 (5993), 830-834.

9. C. Xie, Z. Lin, L. Hanson, Y. Cui, B. Cui, Intracellular recording of action potentials by nanopillar electroporation. Nature nanotechnology 2012, 7 (3), 185-190.

10. J. T. Robinson, M. Jorgolli, A. K. Shalek, M.-H. Yoon, R. S. Gertner, H. Park, Vertical nanowire electrode arrays as a scalable platform for intracellular interfacing to neuronal circuits. Nature nanotechnology 2012, 7 (3), 180-184.

11. M. R. Angle, B. Cui, N. A. Melosh, Nanotechnology and neurophysiology. Current opinion in neurobiology 2015, 32, 132-140.

12. X. Duan, T.-M. Fu, J. Liu, C. M. Lieber, Nanoelectronics-biology frontier: From nanoscopic probes for action potential recording in live cells to three-dimensional cyborg tissues. Nano today 2013, 8 (4), 351-373.

13. J. T. Robinson, M. Jorgolli, H. Park, Nanowire electrodes for high-density stimulation and measurement of neural circuits. 2013.

14. E. Neher, B. Sakmann, J. H. Steinbach, The extracellular patch clamp: a method for resolving currents through individual open channels in biological membranes. Pflügers Archiv 1978, 375 (2), 219-228.

15. M. Martina, I. Vida, P. Jonas, Distal initiation and active propagation of action potentials in interneuron dendrites. Science 2000, 287 (5451), 295-300.

16. D. Henze, G. Buzsaki, Action potential threshold of hippocampal pyramidal cells in vivo is increased by recent spiking activity. Neuroscience 2001, 105 (1), 121-130.

17. M. Scanziani, M. Häusser, Electrophysiology in the age of light. Nature 2009, 461 (7266), 930-939.

18. Z. C. Lin, B. Cui, Nanowire transistors: room for manoeuvre. Nature nanotechnology 2014, 9 (2), 94-96.

19. M. E. Spira, A. Hai, Multi-electrode array technologies for neuroscience and cardiology. Nature nanotechnology 2013, 8 (2), 83-94.

20. X. Dai, B. Nguyen, Y. Hwang, C. Soci, and S. A. Dayeh, Novel Heterogeneous Integration Technology of III-V Layers and InGaAs FinFETs to Silicon. Advanced Functional Materials, 24, 4420-4426, 2014.

21. W. Tang, B.-M. Nguyen, R. Chen, and S. A. Dayeh, Solid-State Reaction of Nickel Silicide and Germanide Contacts to Semiconductor Nanochannels. Semiconductor Science and Technology 29, 54004, 2014.

22. M. Merz, and P. Fromherz, Silicon Chip Interfaces with a Geometrically Defines Net of Snail Neurons. Adv. Func. Mat. 15, 739, 2005.

23. Y. Shi, P. Kirwan, and F.J. Livesey, Directed differentiation of human pluripotent stem cells to cerebral cortex neurons and neural networks. Nature Protocols, 7(10) 1836-46, 2012.

24. Y. Shi, P. Kirwan, J. Smith, H.P. Robinson, and F.J. Livesey, Human cerebral cortex development from pluripotent stem cells to functional synapses. Nature Neuroscience, 15(5) 477-86, 2012.

25. C. Bardy, M. Hurk, T. Eames, C. Marchand, R. V. Hernandez, M. Kellogg, M. Gorris, B. Galet, V. Palomares, J. Brown, A. G. Bang, J. Mertens, L. Böhnke, L. Boyer, S. Simon, and F. H. Gage, Neuronal medium that supports basic synaptic functions and activity of human neurons in vitro. Proc Natl Acad Sci USA 112(20)E2725-34, 2015.

26. J. R. Buitenweg, W. L. C. Rutten, E. Marani, Geometry-based finite-element modeling of the electrical contact between a cultured neuron and a microelectrode. IEEE Trans. Biomed. Eng. 50 (2003) 501–509.

27. D. Prè, M. W. Nestor, A. A. Sproul, S. Jacob, P. Koppensteiner, V. Chinchalongporn, M. Zimmer, A. Yamamoto, S. A. Noggle, and O. Arancio, A Time Course Analysis of the Electrophysiological Properties of Neurons Differentiated from Human Induced Pluripotent Stem Cells (iPSCs). PlosOne 9, e103418, 2014.

28. S. A. Dayeh, R. Chen, S. H. Lee, R. Liu, Y. G. Ro, and A. Tanaka, "Novel Integration Scheme for High-Density 3D Intra-cellular Probes with sub-micron Pitch and Individual Electrical Addressability," United States Provisional Patent, 2015.

29. S. A. Dayeh, R. Chen, S. H. Lee, R. Liu, Y. G. Ro, and A. Tanaka, "Novel Integration Scheme for High-Density 3D Intra-cellular Probes with sub-micron Pitch and Individual Electrical Addressability," United States Provisional Patent, 2015.

30. R. Wolffenbuttel, K. Wise, Low-temperature silicon wafer-to-wafer bonding using gold at eutectic temperature. Sensors and Actuators A: Physical 1994, 43 (1-3), 223-229.

31. W. Tang, B.-M. Nguyen, R. Chen, S. A. Dayeh, Solid-state reaction of nickel silicide and germanide contacts to semiconductor nanochannels. Semiconductor Science and Technology 2014, 29 (5), 054004.

32. X. Dai, B. M. Nguyen, Y. Hwang, C. Soci, S. A. Dayeh, Novel heterogeneous integration technology of III–V layers and InGaAs finFETs to silicon. Advanced Functional Materials 2014, 24 (28), 4420-4426.

33. R. Chen, S. A. Dayeh, Size and Orientation Effects on the Kinetics and Structure of Nickelide Contacts to InGaAs Fin Structures. Nano letters 2015, 15 (6), 3770-3779.

34. H. S. Engelman, A. B. MacDermott, Presynaptic ionotropic receptors and control of transmitter release. Nature Reviews Neuroscience 2004, 5 (2), 135-145.

35. G. A. Kerchner, R. A. Nicoll, Silent synapses and the emergence of a postsynaptic mechanism for LTP. Nature Reviews Neuroscience 2008, 9 (11), 813-825.

36. Photolithography is used here to define the outer large electrodes, and the center electrodes in nano-scale are patterned by EBL registered to the photolithography pattern utilizing a 100 kV e-beam writer (JEOL JBX- 6300FS) with beam size ~10 nm.

37. M. Merz, P. Fromherz, Silicon chip interfaced with a geometrically defined net of snail neurons. Advanced Functional Materials 2005, 15 (5), 739-744.

38. A. Fendyur, N. Mazurski, J. Shappir, M. E. Spira, Formation of essential ultrastructural interface between cultured hippocampal cells and gold mushroom-shaped MEA-toward "IN-CELL" recordings from vertebrate neurons. Frontiers in neuroengineering 2011, 4, 14.

39. A. Hai, M. E. Spira, On-chip electroporation, membrane repair dynamics and transient in-cell recordings by arrays of gold mushroom-shaped microelectrodes. Lab on a Chip 2012, 12 (16), 2865-2873.

40. S. M. Ojovan, N. Rabieh, N. Shmoel, H. Erez, E. Maydan, A. Cohen, M. E. Spira, A feasibility study of multi-site, intracellular recordings from mammalian neurons by extracellular gold mushroom-shaped microelectrodes. Scientific reports 2015, 5, 14100.

41. D. Prè, M. W. Nestor, A. A. Sproul, S. Jacob, P. Koppensteiner, V. Chinchalongporn, M. Zimmer, A. Yamamoto, S. A. Noggle, O. Arancio, A time course analysis of the electrophysiological properties of neurons differentiated from human induced pluripotent stem cells (iPSCs). PloS one 2014, 9 (7), e103418.

42. J. Lee, J. C. Callaway, R. C. Foehring, Effects of temperature on calcium transients and Ca^{2+}-dependent afterhyperpolarizations in neocortical pyramidal neurons. Journal of neurophysiology 2005, 93 (4), 2012-2020.

43. X. Xie, A. M. Xu, M. R. Angle, N. Tayebi, P. Verma, N. A. Melosh, Mechanical model of vertical nanowire cell penetration. Nano letters 2013, 13 (12), 6002-6008.

44. A. M. Xu, A. Aalipour, S. Leal-Ortiz, A. H. Mekhdjian, X. Xie, A. R. Dunn, C. C. Garner, N. A. Melosh, Quantification of nanowire penetration into living cells. Nature communications 2014 Apr 7; 5: 3613.

45. J.-H. Lee, A. Zhang, S. S. You, C. M. Lieber, Spontaneous internalization of cell penetrating peptide-modified nanowires into primary neurons. Nano letters 2016, 16 (2), 1509-1513.

46. The capacitive nature of the bare Si nanowire-cytoplasm interface precludes the measurement of cell resting potentials but coatings of the nanowire tips with faradiac materials such as Ag/AgCl or bioreagents should make this possible.

47. A. Hai, J. Shappir, M. E. Spira, In-cell recordings by extracellular microelectrodes. Nature methods 2010, 7 (3), 200-202.

48. A. Pedroni, D. D. Minh, A. Mallamaci, E. Cherubini, Electrophysiological characterization of granule cells in the dentate gyrus immediately after birth. 2014.

49. N. Shmoel, N. Rabieh, S. M. Ojovan, H. Erez, E. Maydan, M. E. Spira, Multisite electrophysiological recordings by self-assembled loose-patch-like junctions between cultured hippocampal neurons and mushroom-shaped microelectrodes. Scientific reports 2016, 6.

Chapter 3

High Yield, Ultra Sharp, Individually Addressable Nanowire Arrays Probe Intracellular Activity from large Neuronal Networks and Cardiomyocytes Tissue

3.1 Introduction

A grand challenge in nanowire-neuron interface is to develop the large-scale nanowire arrays with ultra-sharp tip and high high-respect ratio for natural penetration and maintenance of the stable interface and healthy neuron. Scaling of the nanowire diameter is critically important to minimize damage to the cells' membrane during the culture, recording, and pharmacological interrogation. In this chapter, we demonstrate ultra-sharp nanowire tips. We designed and developed a new fabrication method that offers for the first time an ultra-sharp sub-10nm nanowire array for individually addressable intracellular mapping (**Figure 3.1**). The ultra-sharp tip enables natural permeation into neuronal cell membranes without electroporation, popularly used by all

other works in this field. We utilize these arrays to perform electrophysiological recordings from rat cortical neurons and cardiomyocytes. Our recordings demonstrate isolated action potentials and spike trains with high signal-to-noise ratios that can be modulated with pharmacology. Significantly, we observed clear spontaneous excitatory postsynaptic potential (EPSP) prior to the larger spike trains. The interfaces of our nanowires with cultured neurons were characterized by SEM/FIB revealing multi-layer 3D neuronal tissue with nanowires clearly penetrating the neuron's soma. Detailed electrical modeling and simulations were employed to signify the importance of individual electrical addressability for efficient high signal-to-noise ratios compared to multi-nanowires per electrode. The simulation results were in good agreement with our experimental investigations in which we deliberately increased the number of nanowires per channel and observed over 10X reduction in the recorded signal amplitudes. Our platform is scalable in terms of channel count and area coverage and recordings with 1024 channels from 3D cell culture and minibrains are underway. Overall, our platform paves the way for longitudinal electrophysiological experiments on synaptic activity in human iPSC-based disease models of neuronal networks, critical for understanding the mechanisms of neurological diseases and for developing drugs to treat them.

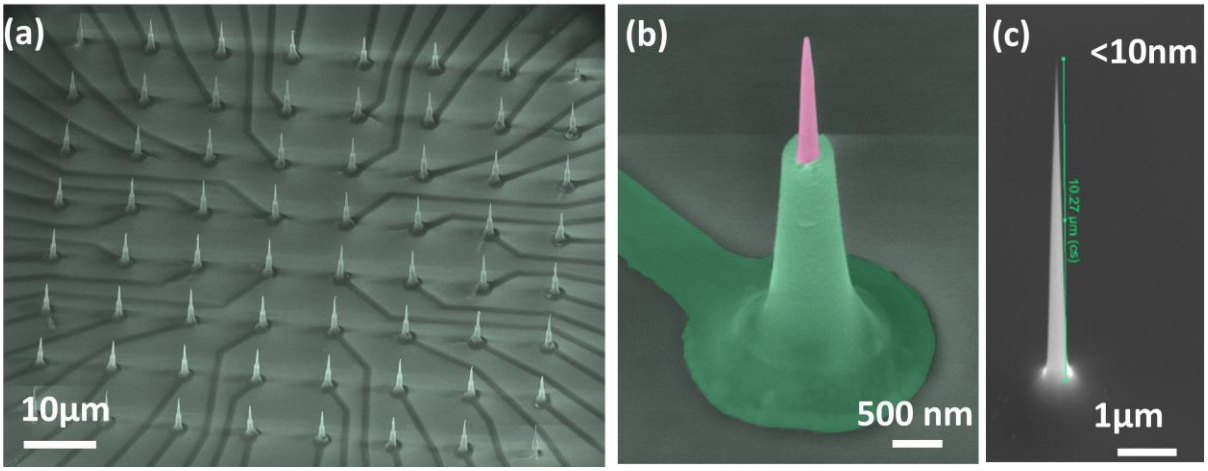

Figure 3.1 SEM images of the high yield, ultra-sharp, individually addressable nanowires: (a) Overview of the nanowire array. (b) a single nanowire with metallization and passivation of SiO_2 (c) nanowire with a few nanometer sharp tip.

3.2 Experimental

3.2.1 Fabrication Flow

The device fabrication flow is shown in Figure 3.1. Firstly, we used electron beam lithography (EBL) to pattern Ni dots and alignment markers on a Si substrate (**Figure 3.2 (a)**). The diameter and shape of the dots influence the nanowire's morphology. The detailed pattern size and shape of Ni dots will be discussed in section **3.2.2**. Secondly, we used dry etching method to form the micro-/nano-wires (**Figure 3.2 (b)**), which was then followed by thermal oxidation at 1100 ℃ (**Figure 3.2 (c)**) and wet etching of SiO_2 (**Figure 3.2 (d)**). By repeating thermal oxidation and wet etching, the diameter of the nanowire's tip could reach a few nanometers. A final thermal oxidation was applied to fully oxidize the nanowires and the surface of the Si substrate (**Figure 3.2 (e)**). Then we used Electron beam lithography/ Photolithography to pattern the electrode leads and pads (**Figure 3.2 (f)**). Finally, we used the PECVD to passivate the surface with the tip of the nanowires exposed. (**Figure 3.2 (g)**).

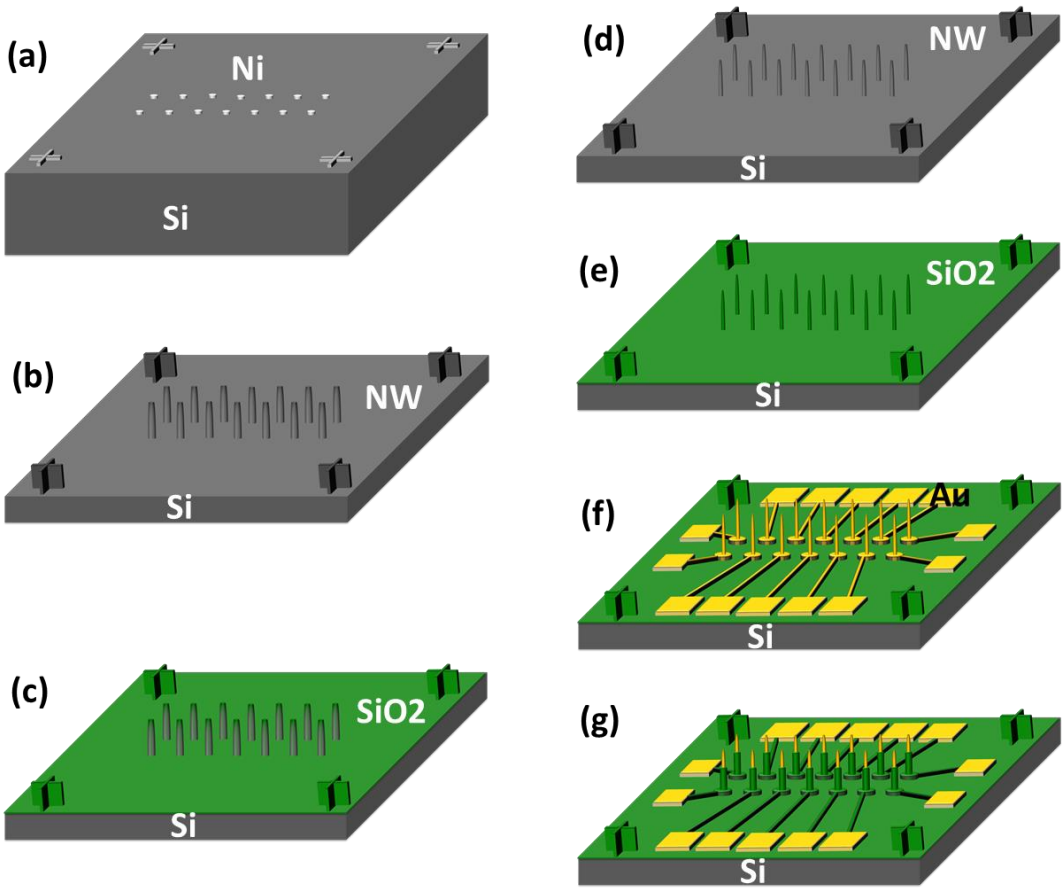

Figure 3.2 Overview of the fabrication flow: (a) Patterning Ni dots on Si substrate; (b) Dry etching micro-/nano-wires; (c) Thermal oxidation; (d) Wet etching oxidation layer; (e) Thermal oxidation; (f) EBL/PL Pattern electrodes; (g) SiO2 Passivation of surface with nanowire tip exposed.

3.2.2 Nanowire Fabrication

We performed mechanistic studies to obtain tapered nanowires with larger base diameter, since the inverted cone structure provides the nanowires enough mechanical strength and stabilize the nanowires' shape and electrical interface with neurons. Firstly, dots patterns (diameter 60 nm) and markers were patterned on the Si substrate by using JEOL EBL (JBX-6300FS), and deposited 10 nm Ti and 200 nm Ni by using electron-beam evaporation. After lift-off process, nanowires and markers were etched by using Plasmatherm SLR-770 DRIE / ICP Etcher. The details of the dry

etching conditions are summarized in **Table 1**, where the reactive-ion etching (RIE) power is 10W, inductively coupled plasma (ICP) power is 700W, chamber pressure is 23 mTorr, chamber temperature is 20 ℃, the gas flow of SF_6, C_4F_8, Ar were 20 sccm, 40 sccm and 40 sccm, respectively, for sample 1 in **Figure 3.3 (a)**. The tip's diameter is larger than that of the base. This structure is unstable and difficult for penetration into the cell's membrane. Since SF_6 is the etching gas for Si, while C_4F_8 can protect the sidewall of the nanowire. Ar helps to increase the Si etching rate. [1] Since we aim to get the tapered nanowire with larger bottom compared to the tip, we decreased the SF_6 gas flow to 15 sccm and kept all other conditions similar to those of sample 1. The nanowire has a tapered structure with the bottom larger than the tip (**Figure 3.3 (b)**). However, the nanowire's height of sample 2 (2.73 μm) is much shorter than its height of sample 1 (10.00 μm). Then, we used 2 hours as the dry etching time for sample 3, which damaged the bottom of the nanowire and cause it to fall down (**Figure 3.3 (c)**).

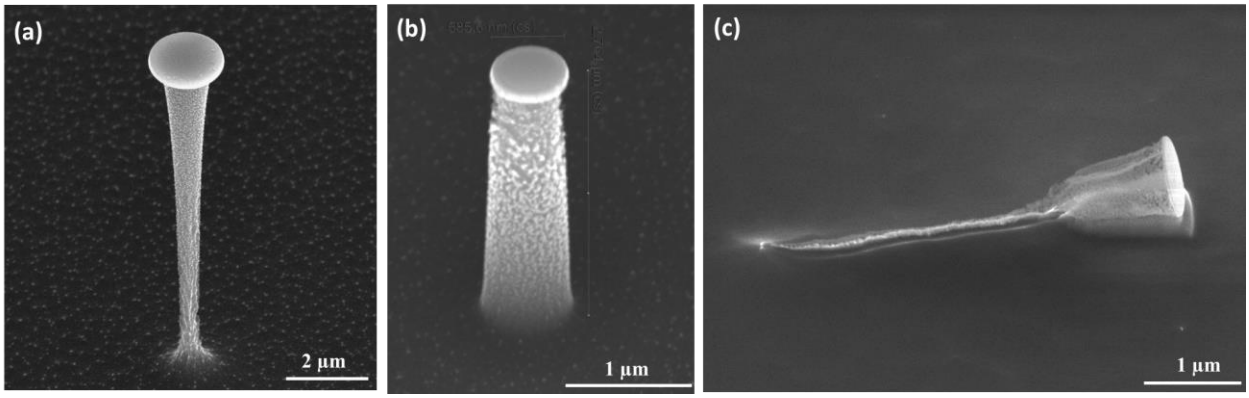

Figure 3.3 Dry etching results for nanowire with the hard mask of a single dot: (a), (b), (c) SEM of the nanowire with dry etching condition of sample 1, 2, 3 in **Table 1**, respectively.

Table 3.1 Dry etching conditions for samples with a single dot as the dry etching mask.

Sample #	SF6 (sccm)	C4F8 (sccm)	Etching Time (min)	Height (μm)	Other conditions
1	20	40	60	10.0	Ar: 40 sccm RIE power: 10 W ICP power: 700 W Temperature: 20 ℃
2	15	40	60	2.73	
3	15	40	120	N.A.	

In order to protect the bottom of the nanowire, we resorted to establish a main larger diameter dot in the center and a group of smaller diameter dots evenly distributed around it (**Figure 3.4 (a)**). The etching conditions of sample 4, 5, 6, and 7 are shown in the Table 2 and etching results are shown in **Figure 3.4 (b)-(e)**. The main dot size, the number of the small dots and the distance of main dot to small dot influence the dry etching results. In **Figure 3.4 (b)**, since the main dot's diameter of sample 4 is not large enough (0.6 µm), the nanowire becomes very thin after 90 min of etching. In **Figure 3.4 (c)**, since the distance of the main dot to the small dot are too far away from each other, the small nanowires fell down during drying etching process. The fallen nanowires formed new hard masks to etch smaller nanowires a little far away to the main nanowire but they could not protect the bottom of the main nanowire. We found that the condition 6 and condition 7 are the best to create the nanowire with the inverted cone structure (**Figure 3.4 (d)** and **Figure 3.4 (e)**).

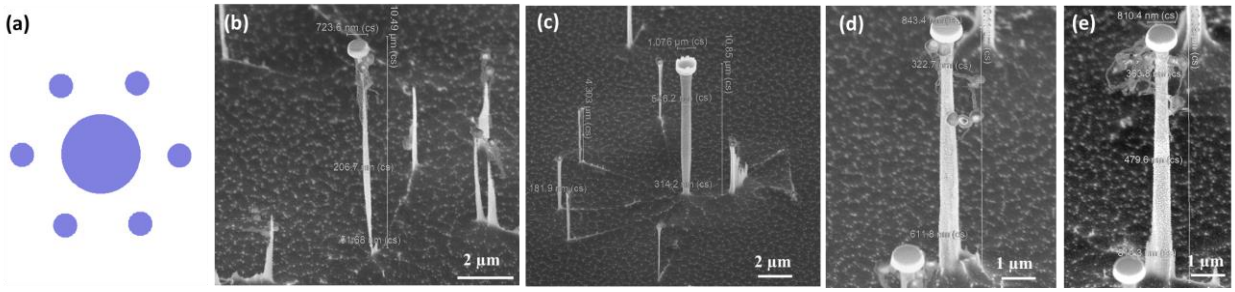

Figure 3.4 Dry etching results for nanowire with the hard mask of a main dot and a group of small dots evenly distributed around it: (a) Design pattern, (b), (c), (d), (e) SEM of the nanowire with dry etching condition of sample 4, 5, 6 and 7 in **Table 2**, respectively.

Table 3.2 Dry etching conditions for nanowires with the hard mask of a main dot and a group of small dots.

Sample #	Main dot (µm)	Small dots (µm)	Number of small dots	Distance: Main dot to Small dot	Other conditions
4	0.6	0.3	6	1.5	SF6: 20 sccm; C4F8: 40sccm Ar: 40 sccm RIE : 10 W;ICP: 700 W Temperature: 20 ℃ Etching Time: 90 min
5	1	0.3	8	2	
6	0.8	0.3	5	1.5	
7	0.8	0.3	6	1.5	

3.2.3 Nanowire Thinning for Ultrasharp Tips

After we optimized the dry etching of the nanowire, we focused on thinning the nanowire to a minimum size of a few nanometers by using thermal oxidation method in **Figure 3.5**. There was still some Ni residue of the hard mask after the dry etching step of the nanowire. Firstly, we use diluted nitric acid (HNO_3: H_2O=1:10) to etch the Ni residue, followed by cleaning polymer with Piranha solution (sulfuric acid: 30% hydrogen peroxide solution=3:1), rinsing with deionized water, drying with N_2 gas (**Figure 3.5 (c)**). Then the sample was then placed on a quartz boat and loaded into a furnace tube. The thermal oxidation temperature is 1100 ℃. There was a layer of SiO_2 formed at the surface of the nanowire and substrate, after the thermal oxidation step. We used wet etching to remove the SiO_2 by using buffered oxide etch (BOE: 6:1 volume ratio of 40% NH_4F in water to 49% HF in water). To avoid the whole nanowire being thermally oxidized, we usually use dry thermal oxidation rather than the wet oxidation. Since the wet oxidation rate is more than 10 times faster than the dry oxidation rate, dry oxidation is more controllable for thinning small nanowires, while wet thermal oxidation is suitable for thick microwire thermal oxide growth and creates a smooth interface at the oxide/Si interface. Even we can calculate the thermal oxidation rate based on Massoud Model, [2-3] there is still small error between the experimental and theoretical results, as expected due to slow oxidation in nanowires. We practically repeated the thermal oxidation and wet etching for a few times to get the nanowire as sharp as a few nanometers (**Figure 3.5 (d) - (f)**).

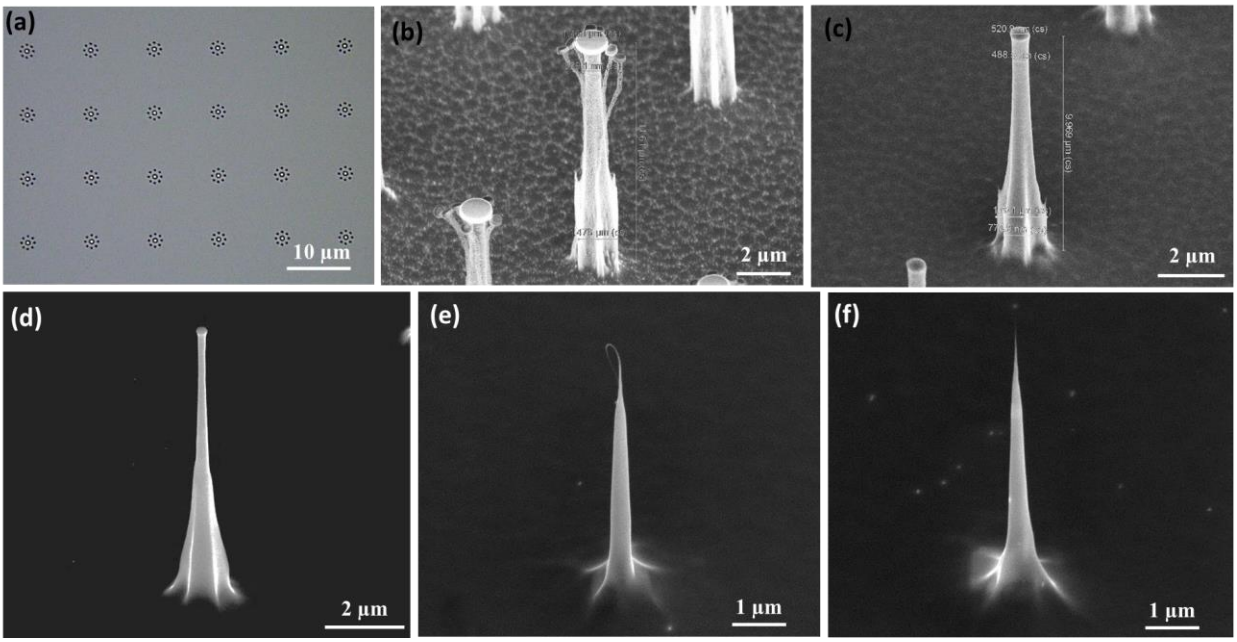

Figure 3.5 Nanowire Thinning: (a) Hard mask pattern after EBL/ebeam depsotion of 10nm Ti and 200nm Ni/ lift off. (b) Dry etching. (c) Ni residue etching. (d), (e), (f) Thermal oxidation and wet etching.

3.2.4 Metallization and Passivation of Nanowire and Electrode

We performed a final step of 400nm thermal oxide growth on the surface after the nanowire tip reaches a few nanometers. This process lasted 9 hours using dry thermal oxidation at 1100 ℃, which compares to only 26 mins using wet thermal oxidation at 1100 ℃. After the sample cleaning by Acetone airbrush, rinsing by isopropyl alcohol (IPA), drying by N_2, dehydration at 180 ℃ on hot plate, O_2 plasma at 200W for 1min, we spun coated a layer of electron beam resist (950 PMMA A6) with spin-coating condition of 4000 rpm, 500 rpm/s and 40s, and baked the sample at 170 ℃ for 10min. Then, we used EBL to write the pattern with the dosage of 1800 µC/cm^2 for leads and 3000 µC/cm^2 for dots (aligned with the nanowire) under the electron beam condition at 100 kV and 6 nA, followed by development (methyl isobutyl ketone (MIBK): IPA=1:3) at 0 ℃ for 2 min, which opens the electron beam resist (950 PMMA A6) on the surface of the nanowires to connect to the leads. We used O_2 plasma descum at 100 W for 1min to etch the PMMA residue in the

pattern. A conductive layer, e.g. 10 nm Ti / 100 nm Au or Pt, etc., was uniformly coated on the sidewall of the nanowire to form a conductive layer and connect the electrode tip to the leads (**Figure 3.6 (a), (d), (e)**). Then, the PL will be used to pattern the outer large electrodes and pads (**Figure 3.6 (b)**). Finally, we used plasma enhanced chemical vapor deposition (PECVD) to deposit a layer of 200 nm SiO_2 at 350 ℃ on the surface of the device with the hard mask (Si wafer with a pocket opening in the center) to avoid the SiO_2 deposition on the around pad (**Figure 3.6 (c)**). Then, we spun coated a layer of electron beam resist (PMMA 950 A4). After 10 min hard bake at 170 ℃, 10 – 20 s O_2 plasma with 200 W was applied to clean the thin PMMA layer on the tip of the nanowire. Then, we use the BOE to etch the SiO_2 on the tip. After cleaning PMMA by acetone and O_2 plasma, the nanowire has ultra-sharp tip (~30 nm) is shown in (**Figure 3.6 (f)**).

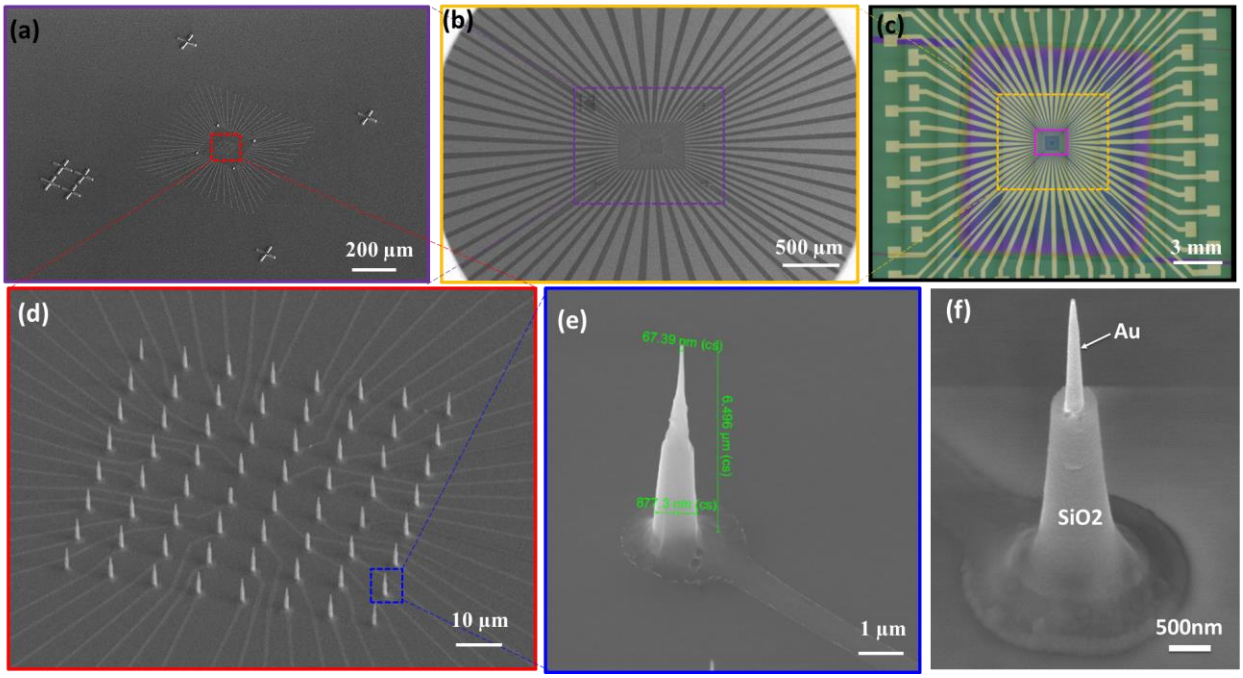

Figure 3.6 Metallization and Passivation of Nanowire and Electrode. (a) EBL of the center leads and nanowire with the detailed SEM image of nanowire array in (b) and detailed SEM image of single nanowire in (e). (b) Photolithography with the outer leads. (c) Passivation surface with SiO2 by PECVD. (f) Passivation of a single nanowire with the tip of metal exposed.

3.2.5 Optimization of the Adhesion between Dielectric Layer and Metal and Solution for Removal of Edge Bead

After culturing the cells on the devices for one week, we found a layer was peeled off in **Figure 3.7 (a)**. A FIB cross-section of peel-off region was cut and showed a gap between the SiO_2 and lead metal (Au or Pt) (**Figure 3.7 (b)**), because of the bad adhesion between SiO_2 with metal of Au or Pt. Another problem is the leads patterned by EBL have high edge bead (**Figure 3.7 (c)**), because that conformally electron beam deposition of metal caused difficulty of the lift-off at the edge of the pattern. To solve the peel-off problem, we deposited an adhesion layer of metal (10 nm Ti) on top of the previous Au or Pt, which helped the passivation adhere well to the metal layers. Then, during EBL of the center leads, we also changed the electron beam resist from a single layer of PMMA 950 A6 to Methyl methacrylate (MMA) (8.5) A6 and PMMA 950 A6. The use for MMA/PMMA bilayer in EBL helps lift-off of metallic structures, since MMA/PMMA bilayer gives an undercut resist profile to avoid metal coating on the sidewall of the resist during the electron beam deposition. After both of the two steps of modification, we did a quick aging test of the devices merging in water at 60 ℃ for 3 days, which is equivalent to the condition of 37 ℃ for 15 days (cell culture temperature and timeline). The devices showed clear surface (**Figure 3.7 (d)**) after the aging test. Two cross-sections of FIB-SEM images demonstrated good adhesion between metal and passivation layer (**Figure 3.7 (e)**) and no edge bead (**Figure 3.7 (f)**).

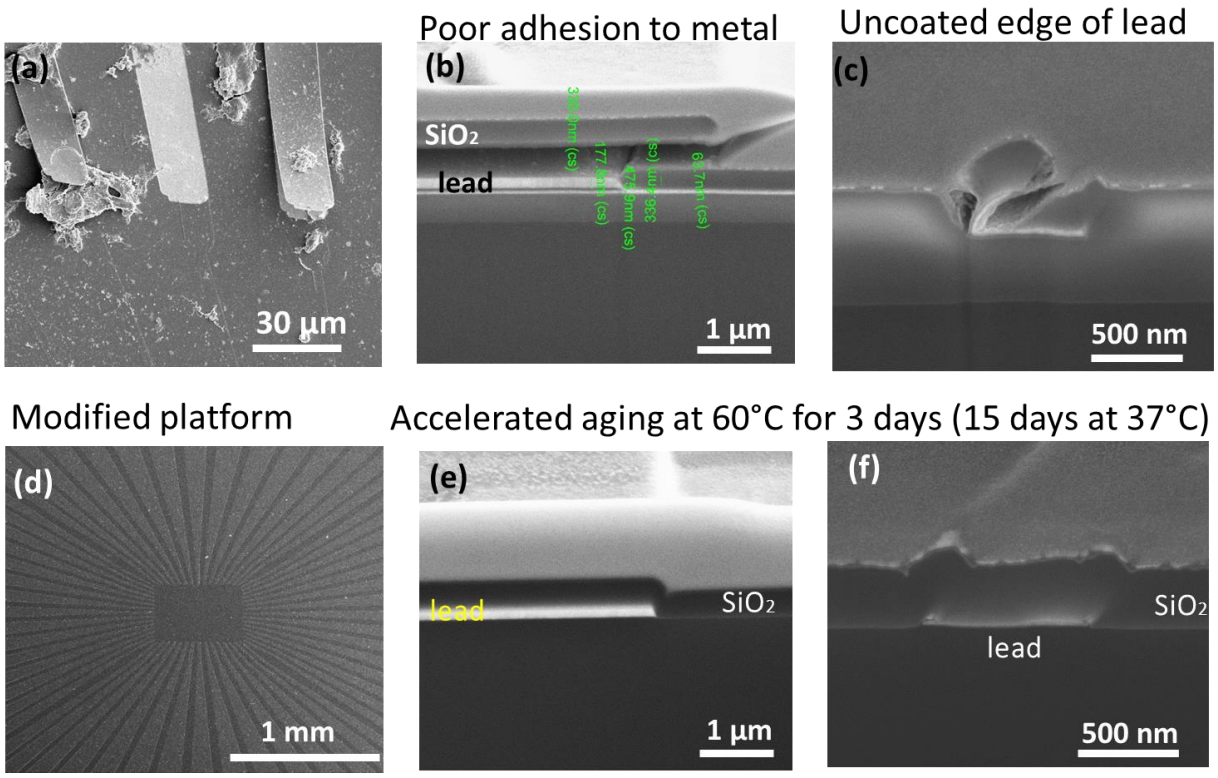

Figure 3.7 SEM images (a) Device peel-off problem. (b) FIB-SEM of poor adhesion between SiO_2 and metal. (c) FIB-SEM of uncoated edge of leads. (d) Device overview after aging test. (e) FIB-SEM of good adhesion between SiO_2 and metal. (f) FIB-SEM of edge of leads.

3.2.6 Surface Roughness Modification

Since surface roughness influence the cell's attachment and neurite formation [4,5], we optimized the surface roughness by two methods in **Figure 3.8**. Diluted HF (volume ratio of HF: DI water=1: 10) doesn't etch the surface uniformly, so we can use it to create rough surface on our device. Our device has two types of SiO_2: first layer is thermal SiO_2 while second layer is PECVD SiO_2. We used diluted HF to etch the device with 200 nm SiO_2 formed by thermal oxidation and the surface roughness is characterized by Atomic Force Microscope (AFM) (**Figure 3.8 (a)**). The 30s etching produced 2.22 nm average roughness and 20.26 nm maximum roughness; the 60s etching created 1.83 nm average roughness and 15.20 nm maximum roughness; the 90s etching

created 0.37 nm average roughness and 4.29 nm maximum roughness. Then, we used diluted HF to etch the device with 500 nm SiO_2 deposited by PECVD and the surface roughness is characterized by AFM (**Figure 3.8 (b)**). The 30s etching produces 1.12 nm average roughness and 15.62 nm maximum roughness; the 60s etching creates 4.34 nm average roughness and 50.71 nm maximum roughness; the 90s etching creates 12.2 nm average roughness and 147.03 nm maximum roughness.

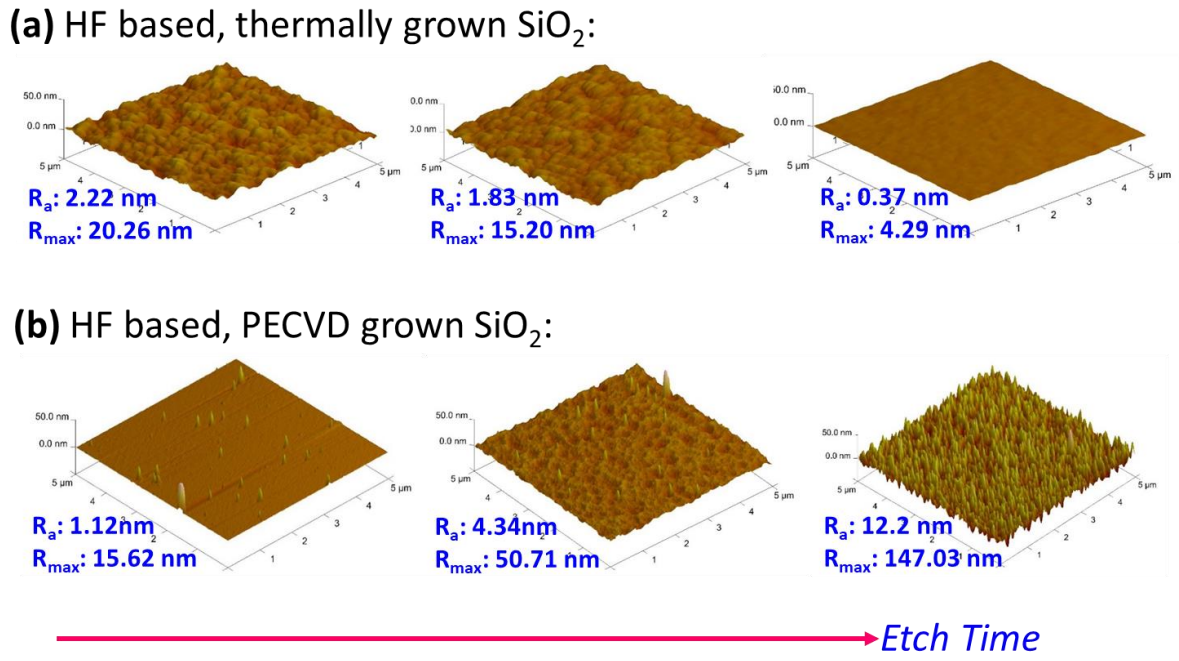

Figure 3.8 AFM images of surface roughness modification: (a) AFM images shows the results of diluted HF etching the SiO_2 formed by thermal oxidation with etching time 30s, 60s, 120s from left to right respectively. (b) AFM images shows the results of diluted HF etching the SiO_2 deposited by PECVD with etching time 30s, 60s, 120s from left to right respectively.

3.2.7 Surface Passivation of Parylene C

Earlier studies have shown that Parylene C is a bio-compatible organic polymer material [6, 7]. We used Parylene C as a top layer of device to preserve the cell's health during culture on our platform. 500 nm Parylene C was deposited by SCS PDS 2010 Specialty Parylene Coating System. Then, we spun coated a layer of photoresist (AZ 1518), applied a hollow PDMS mask with Al foil to protect the center Parylene C layer and the Nanowire array during the photolithography, followed by developing with AZ 300. The exposed Parylene C at the pad regions and nanowire tips was etched by O_2 plasma by using Oxford P80 RIE etcher. The final SEM image of the nanowire with two passivation layers is shown in **Figure 3.9 (a)**. We also use the AFM to characterize the surface roughness, which showed an average roughness of 7.00 nm in **Figure 3.9 (b)**.

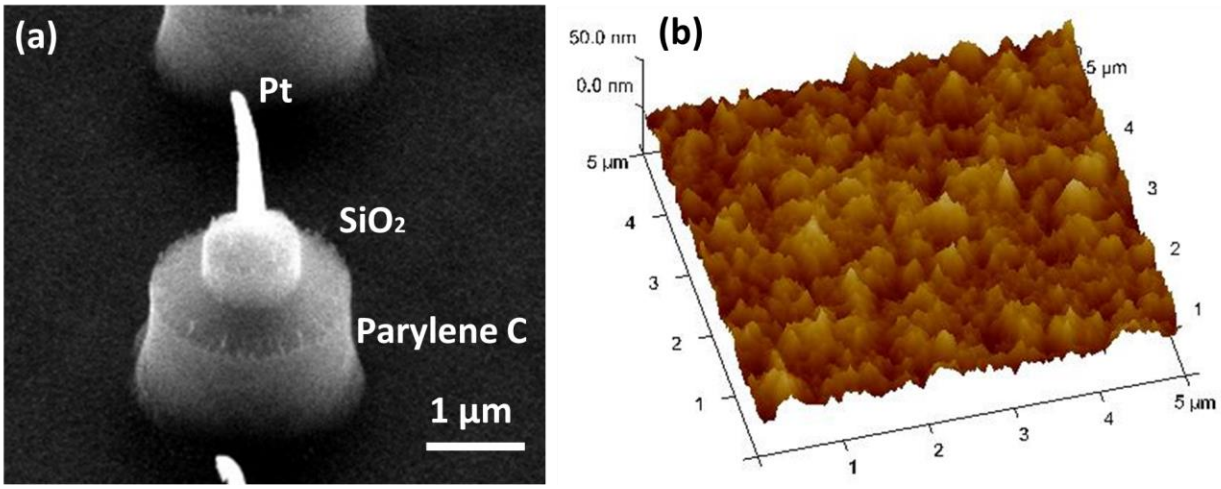

Figure 3.9 (a) SEM image of the nanowire with two passivation layers of SiO_2 for Electrical insulation and Parylene C for cell adhesion. (b) AFM of the final roughness of the device.

3.2.8 Packaging of Fabricated Nanowire Arrays

Two types of devices were fabricated to fit two types of measurement equipment: Tucker-Davis Technologies (TDT) neurophysiology platform (**Figure 3.10** (a)) and the Intan Stimulation/Recording System (**Figure 3.10** (b)). The device (named as 64_Ch_TDT) made for TDT platform has 64 channels (**Figure 3.10** (c)) and the 8×8 individually addressable nanowire array is shown at the center of the device (**Figure 3.10** (e)). We bonded a culture ring in the center of the sample 64_Ch_TDT by Polydimethylsiloxane (PDMS), where cells were cultured inside of the ring. While the device (named as 128_Ch_Intan) made for Intan Stimulation/Recording System had 128 channels (**Figure 3.10** (d)) and the 4 arrays of 32 individually addressable nanowire are shown in the center of the device (**Figure 3.10** (f)). We bonded a culture ring in the center of sample 128_Ch_Intan by PDMS. Then, the device is bonded with the flexible ribbon cable by using the anisotropic conductive film (ACF) bonding at 100 ℃. The 128 nanowires of sample 128_Ch_Intan are distributed for 4 arrays with different nanowire pitch as 5 μm, 10 μm, 30 μm, 70 μm as shown in the **Figure 3.11 (a)-(d)**, respectively.

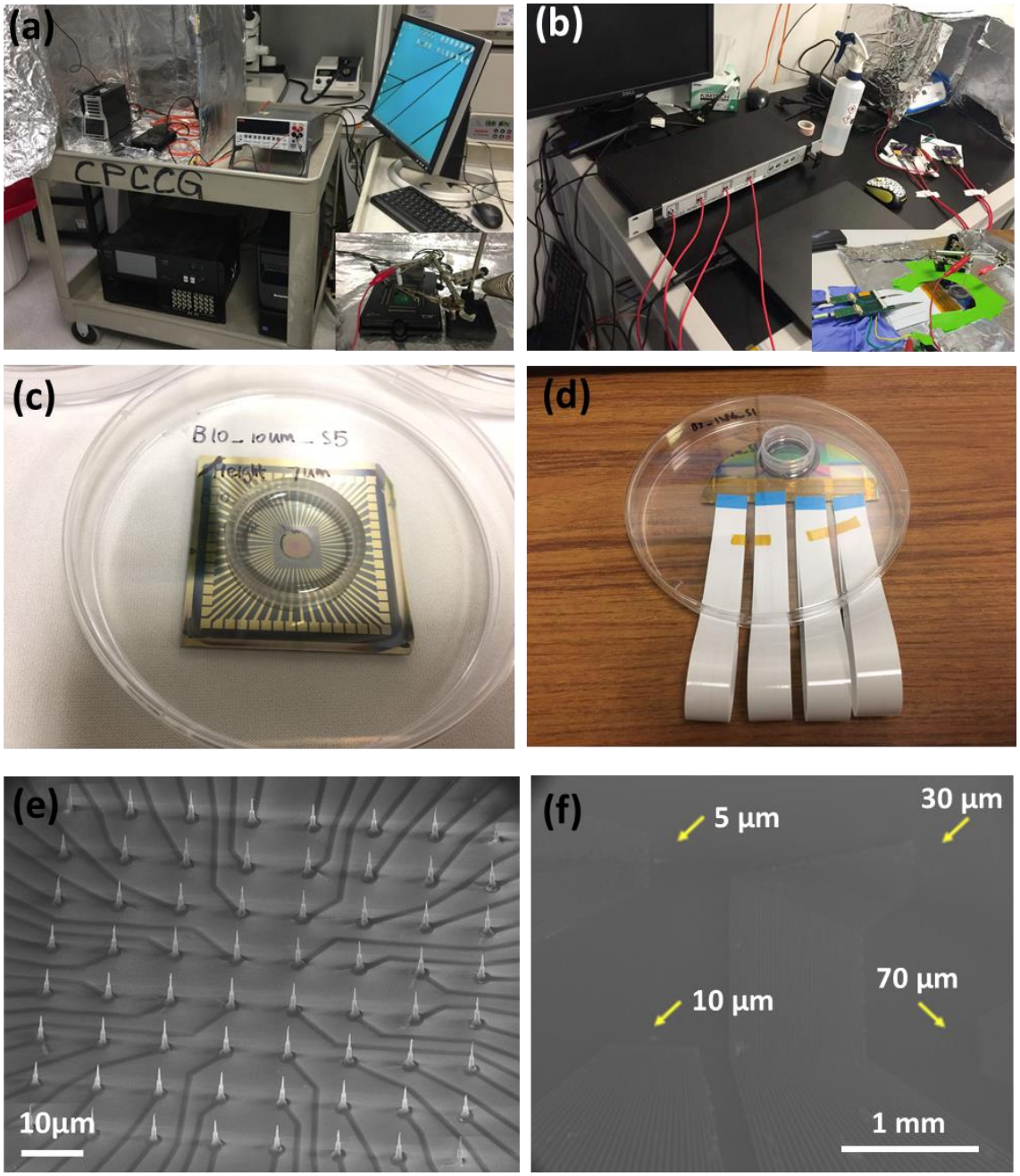

Figure 3.10 (a) TDT platform. (b) Intan Stimulation/Recording System (c) Overview image of sample 64_Ch_TDT. (d) Overview image of sample 128_Ch_Intan. (e) Overview SEM image of the 8×8 individually addressable nanowire for sample 64_Ch_TDT. (f) Overview SEM image of the 4 addressable nanowire arrays for sample 128_Ch_Intan.

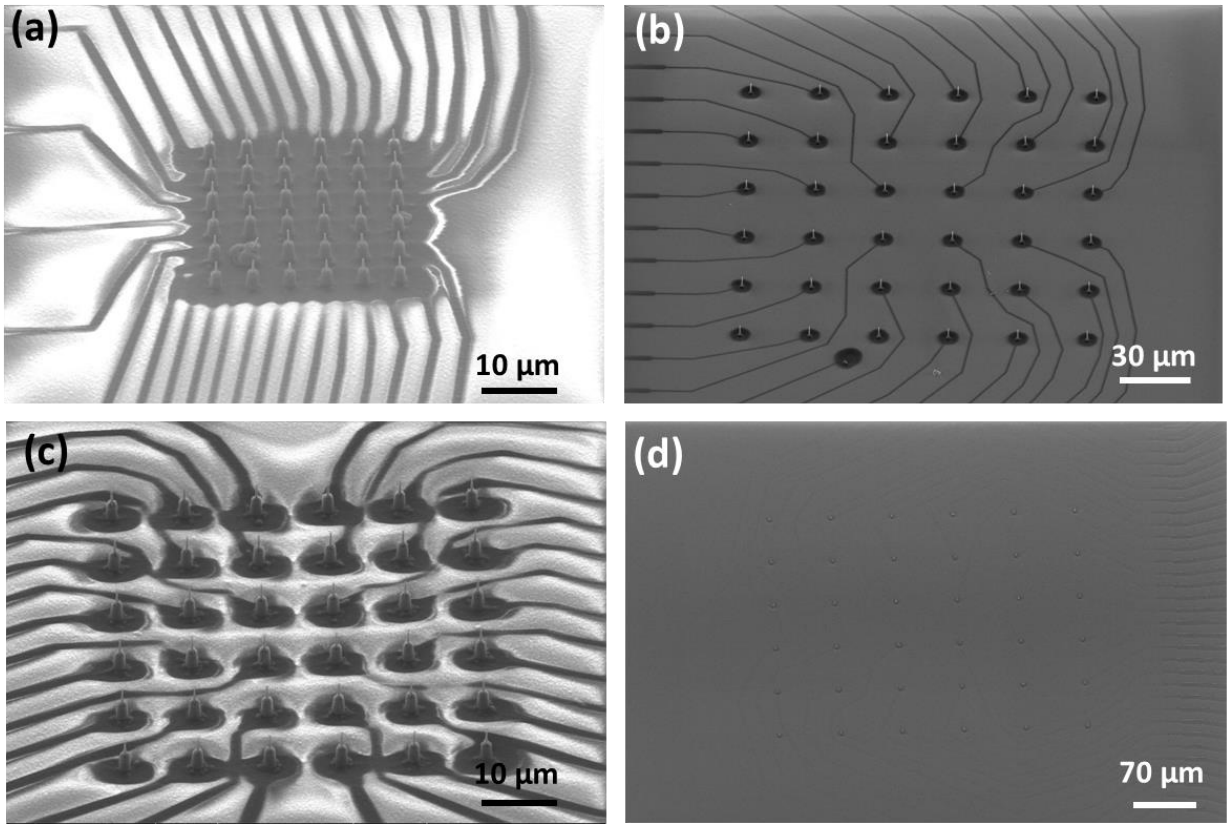

Figure 3.11 (a)-(d) Overview SEM image of the 4 arrays for sample 128_Ch_Intan with nanowire pitch of 5 µm, 10 µm, 30 µm, 70 µm, respectively.

3.2.9 Nanowire Electroplation with PEDOT:PSS for Neural Stimulation

Poly (3, 4-ethylenedioxythiophene): Poly(styrenesulfonate) (PEDOT:PSS) is widely applied in biomedical device research due to its biocompatibility [8, 9], its excellent chemical stability [10], and its low electrochemical impedance over a very wide range of frequencies [11, 12]. For efficient extracellular electrical stimulation of the neuronal networks, we electroplated PEDOT: PSS on several channels of the array (**Figure 3.12**), since PEDOT: PSS allows higher current injection without reaching water hydrolysis.

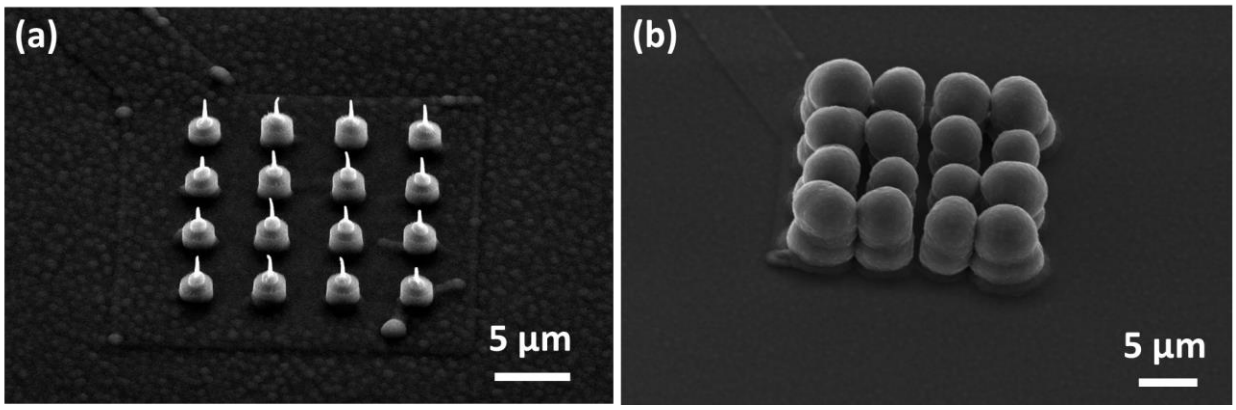

Figure 3.12 (a) SEM image of nanowire before electroplated. (b) SEM image of nanowire after electroplated PEDOT: PSS

3.2.10 Electrochemical Impedance Spectroscopy and Charge Injection Capacity

EIS was performed by using the GAMRY Interface 1000E with merging the nanowire array in phosphate buffer saline (PBS) solution, by using three electrodes: a large platinum electrode as a counter electrode, an Ag/AgCl electrode as a reference, and nanowire electroplated with PEDOT:PSS as the working electrode. Then, sinusoidal signals with 10 mV rms (root mean square) AC voltage (zero DC voltage) were applied. We measured the electrochemical impedance for a bare nanowire (**Figure 3.13** (a)) and a nanowire electroplated PEDOT: PSS (**Figure 3.13** (b)) with the frequency range from 1 Hz to 10 kHz. The electrode impedance decreased by two orders of magnitude for all frequencies.

In addition, electrochemical current pulse injection with chronopotentiometry mode and cyclic voltammetry were performed by using the GAMRY Interface 1000E by submerging the nanowire array in PBS solution and using three electrodes: a large platinum electrode as a counter electrode, an Ag/AgCl electrode as a reference, and nanowire/ nanowire electroplated PEDOT:PSS as the working electrode. Cathodic first, bi-phasic, charge-balanced current pulse were injected across counter electrode and working electrode, while the working electrode's polarization

potential with reference to Ag/AgCl electrode was measured. E_{mc} is calculated as working electrode potential versus Ag/AgCl electrode 10 μs after cathodal pulse ended, while E_{ma} is calculated as working electrode potential versus Ag/AgCl electrode 10 μs after anodal pulse ended. For organic electrodes (PEDOT:PSS/Au or PEDOT:PSS/Pt), the water window limit is between -0.9 V to 0.6 V; while for metallic electrodes (Pt or Au), water window limit is between -0.6 V to 0.8 V [13]. E_{mc} is the potential when the electrode/solution interfacial potential reaches reduction (cathodal limit) and E_{ma} is the potential when it reaches oxidation (anodal limit). CIC is total charge density at which either E_{ma} reaches water oxidation potential or E_{mc} reaches water reduction potential in equation (3-1).

$$\boldsymbol{CIC=Q_{inj}/GSA} \tag{3-1}$$

The CIC for bare Pt nanowire and the nanowire electroplated PEDOT: PSS were 0.60 mC/cm^2 and 2.98 mC/cm^2, respectively (**Figure 3.13 (c) (d)**). Electroplating PEDOT: PSS on the nanowire increases its current injection capacity by nearly 5 times. The PEDOT:PSS is therefore more effective for neuronal stimulation without reaching water hydrolysis.

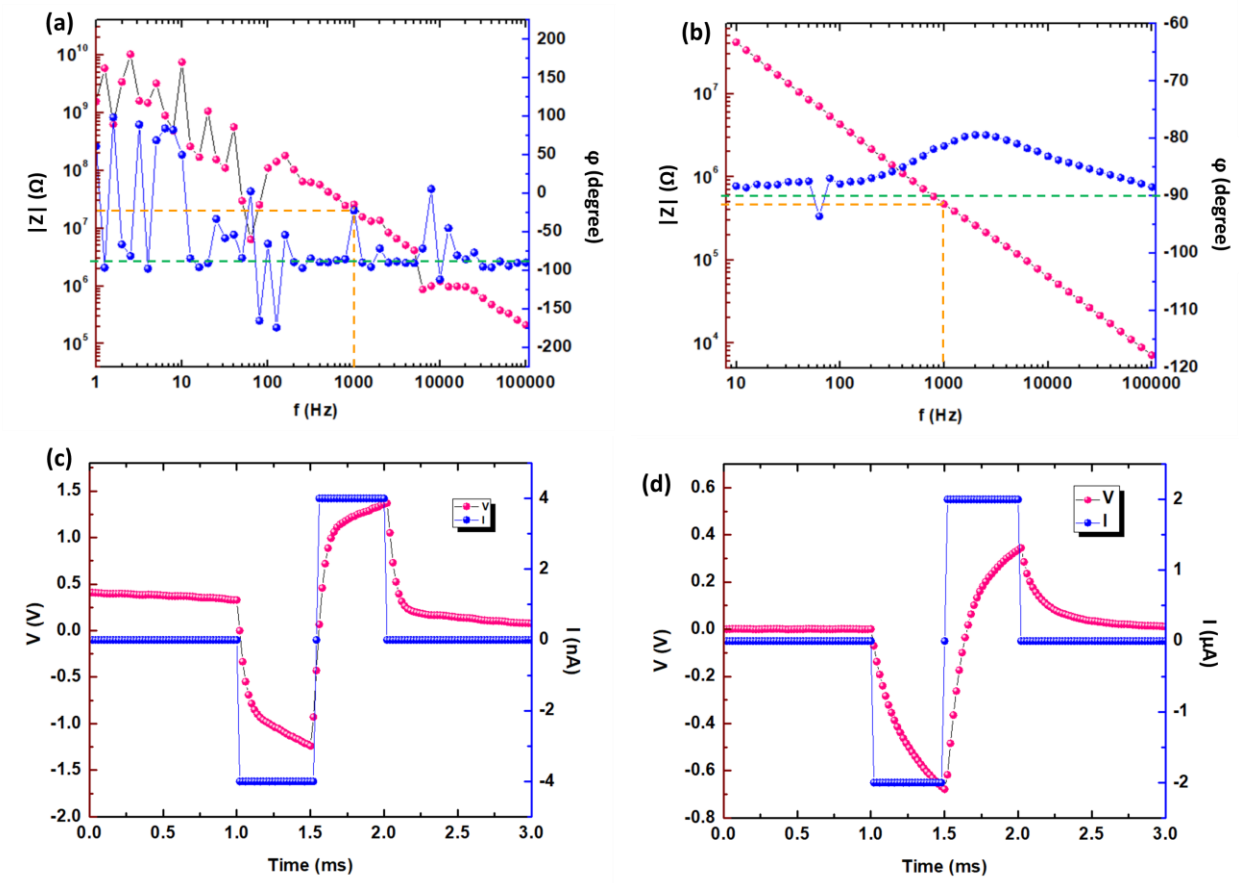

Figure 3.13 (a) EIS for bare nanowire. (b) EIS for nanowire electroplated PEDOT: PSS. (a) CIC for bare nanowire. (b) CIC for nanowire electroplated PEDOT: PSS.

3.2.11 Cell culture: Neurons and Cardiomyocytes

The cell culture of neurons followed previously discussed processes in section **2.4**, and the cell culture of CMs is discussed below. iPSC-derived cardiovascular progenitor cells (iPSC-CVPCs) derived as described by D'Antonio-Chronowska [14] were cryopreserved at day 25 (D25) of the differentiation. Next, cryopreserved iPSC-CVPCs were thawed either on a 6-well plate coated overnight with Matrigel (Corning) or directly on a nanowire device coated with Matrigel for 5h or overnight. Next day, cells were fed with fresh RPMI 1640 medium (Thermo Fisher

Scientific) containing B27 Supplement (50X) (Thermo Fisher Scientific). Cells were cultured on a 6-well plate for 2 days before plating on a nanowire device. 5×10^4, 1×10^5 or 2×10^5 cells were plated over the active regions of a nanowire device in a 5-8 μl of RPMI 1640 medium containing B27 Supplement. After cells were plated on a nanowire device, iPSC-CVPCs were cultured for 5-7 days prior to first recording with medium change every other day. iPSC-CVPCs were also fed with fresh medium a day before any recording.

3.2.12 Cell Fixation and SEM/FIB Sample Preparation

Cell fixation and SEM/FIB sample preparation were followed the procedure described in section **2.3.3.1**.

3.3 Results and Discussion

3.3.1 Impact of Surface Roughness and Parylene C on Network Formation

Since the device was fabricated on the Si substrate that had a smooth surface with an average roughness less than 1nm in the AFM image of **Figure 3.14 (a).** After cell culture for 13 days in vitro (DIV), cells are fixed, dehydrated, dried at critical point and coated with 10 nm IrOx for the images in **Figure 3.14 (c).** There were very few or no neurites formed around and in between different somas. After the surface roughness modification of SiO_2 and Parylene C as described in **3.2.5 and 3.2.6**, the average roughness was 7 nm in **Figure 3.14 (b).** The cell culture results were shown in **Figure 3.14 (d),** where the neuronal soma showed spherical shape, millions of neurites were formed and connected with each other. For the fluorescence images of Rat cortical neurons, red color labels MAP2b neuronal marker, blue color labels DAPI nuclear marker and green color labels GFAP of astrocyte marker in **Figure 3.15 (a)**, while yellow color labels β-

Tubulin of neuronal marker, blue color labels DAPI nuclear marker and green color labels GFAP of astrocyte marker in **Figure 3.15 (b)**.

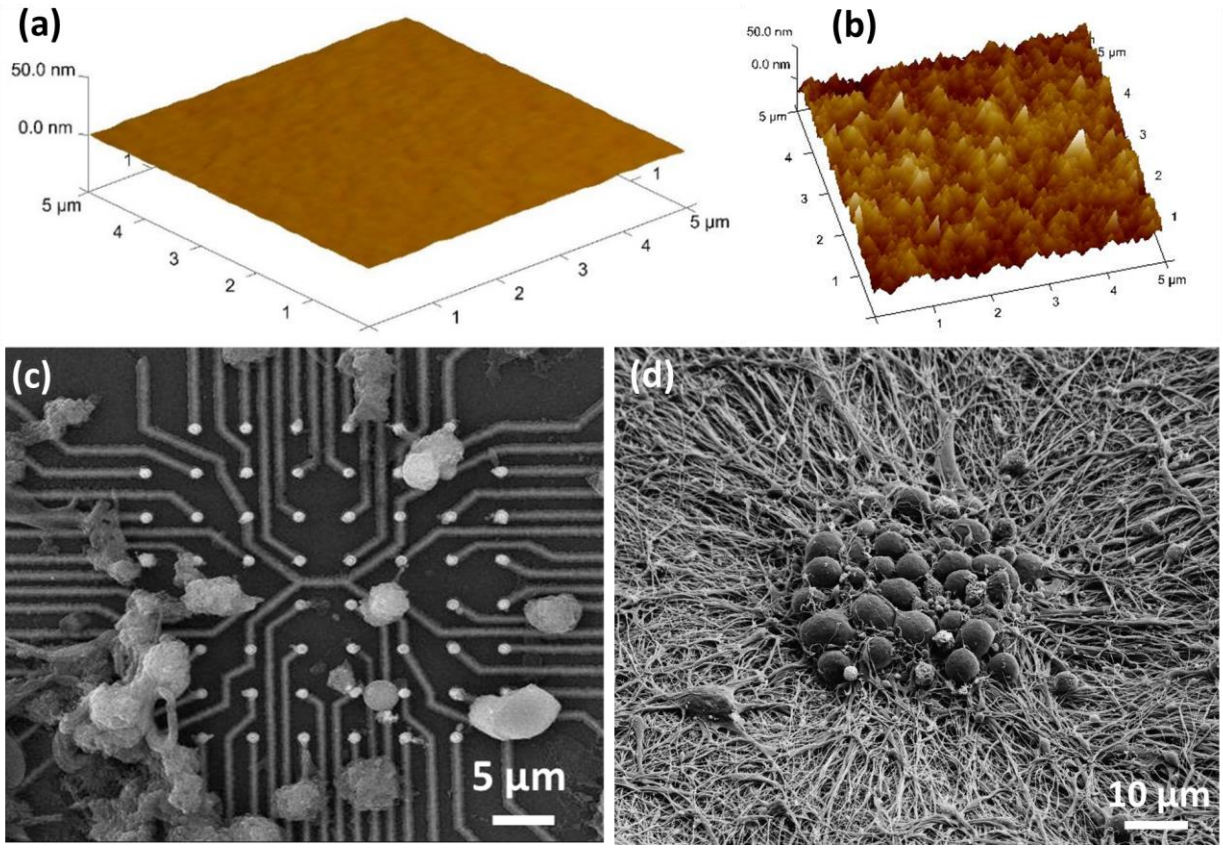

Figure 3.14 (a) AFM image of the device before the roughness optimization with average roughness less than 1 nm. (b) AFM image of the device after the roughness optimization with average roughness of 7 nm. (c) (d) SEM images of the rat cortical neurons interface with the device before and after surface optimization.

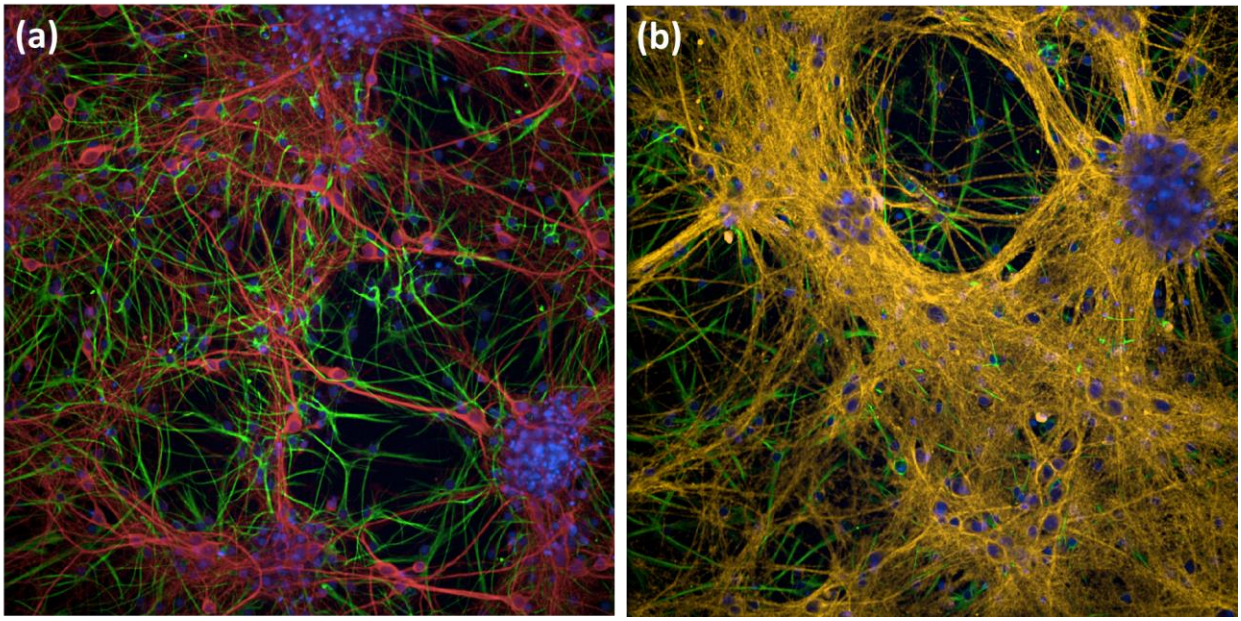

Figure 3.15 Fluorescence images of Rat cortical neurons (a) Red: MAP2b neuronal marker; Green: GFAP, astrocyte marker; Blue: DAPI nuclear marker. (b) Yellow: β-Tubulin, neuronal marker; Green: GFAP, astrocyte marker; Blue: DAPI nuclear marker.

3.3.2 Mapping Activity of Large Neuronal Networks with Sensitivity to Subthreshold Potentials

Multiple arrays with variable nanowire pitch (5 µm, 10 µm, 30 µm, and 70 µm) were investigated with each array composed of 32 nanowires. Electrophysiological recordings were carried out 7 days in vitro (DIV) (**Figure 3.16**) using Intan stimulation/recording amplifiers, in which 31 out of 32 channels showed positive potentials with some channels exhibiting spike trains. These spike trains manifested intracellular features with clear EPSP events (**Figure 3.17 (b)**). The natural intracellular penetration of the cellular membrane resulted in stable amplitude of the action potentials in the recorded spike trains. This amplitude was clipped in many instances to the maximum range of the Intan recording amplifiers of ~10mV. Two types neuronal activities were

recorded: first neuronal activity showed a firing rate of ~15 Hz (**Figure 3.17 (a)**), while second neuronal activity shows clear EPSP caused action potential with firing rate at ~2.4 Hz (**Figure 3.17 (c)**). From the power spectrogram (**Figure 3.17 (b) and (d)**) high frequency (~ 1 kHz) power is evident and corresponds to the fast depolarization step caused by sodium ion channels that open with large amount of Na^+ flow inside the cell. The results shown in Fig. 3.17 are the first electrophysiological results demonstrating reliable nanowire recordings of action potential trains with clear graded potentials and without any electroporating manipulation elevating the promise of this technology for longitudinal and reliable intracellular electrophysiology from networks of neurons and mini-brains.

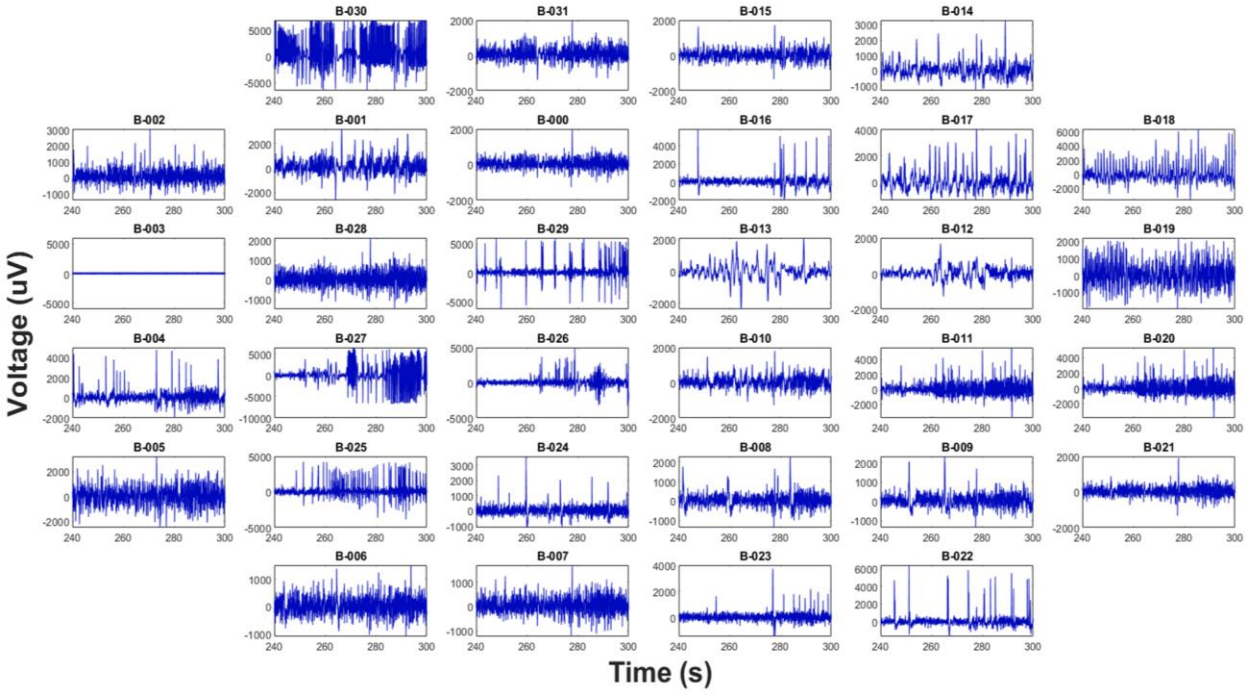

Figure 3.16 Large neuron network activities mapping from all 32 channels of this array: Most channels showed large action potentials with some channels showing spike trains.

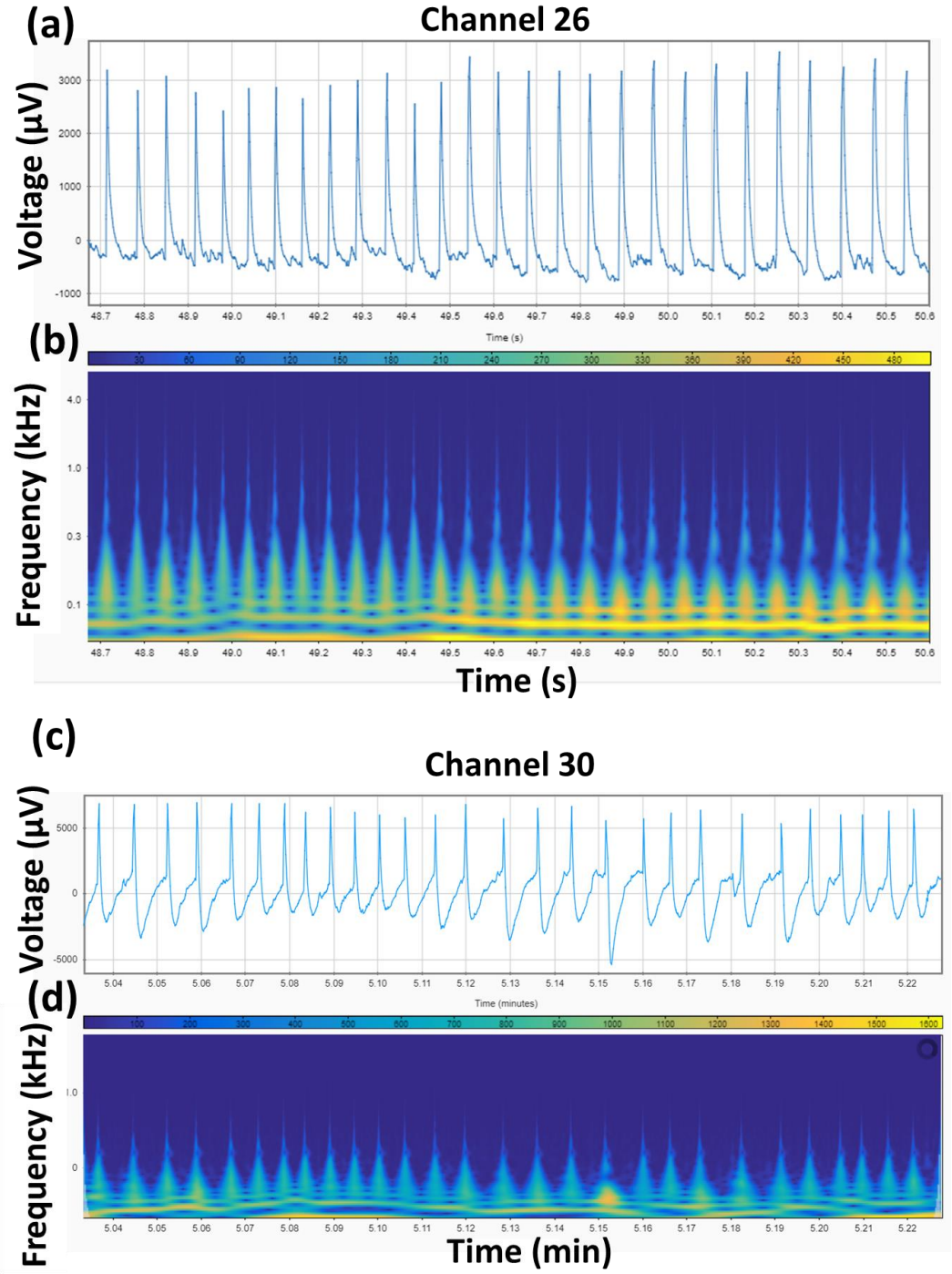

Figure 3.17 Two types neuronal activities: (a) action potential with firing rate at ~15 Hz. (c) EPSP caused action potential with firing rate at ~2.4 Hz. (b), (d) power spectrogram of (a), (c), respectively.

3.3.3 Electrical Stimulation and Response

The nanowire platform recorded clear electrical response from neurons with electrical stimulation. **Figure 3.18** shows a sequence recorded from channel 30 from 60^{th} second to 105^{th} second, where 60^{th} – 65^{th} seconds shows the neuron activity before stimulation (**Figure 3.18 (a)**), 79^{th} – 84^{th} seconds shows the neuron activity during stimulation (5 biphasic pulses with 1 Hz frequency, the amplitude of ±10 nA and time of 500 µS) (**Figure 3.18 (b)**), and 100^{th} – 105^{th} seconds shows the neuron activity after stimulation (**Figure 3.18 (c)**). Local field potentials with few or no action potentials were recorded before stimulation. A few action potentials start to emerge between two stimulation pulses and the firing rate increased with further stimulation to continuous firing. Replotting **Figure 3.18 (c)** on a smaller voltage range in **Figure 3.18 (d)**, clear spikes with local field potentials can be observed. By applying high pass filter (HPF) at 270 Hz and low pass filter (LPF) at 100 Hz, the filtered signals were shown in **Figure 3.18 (c)**, respectively, where the action potential showed similar amplitude, indicating the stable interface of nanowire and neurons.

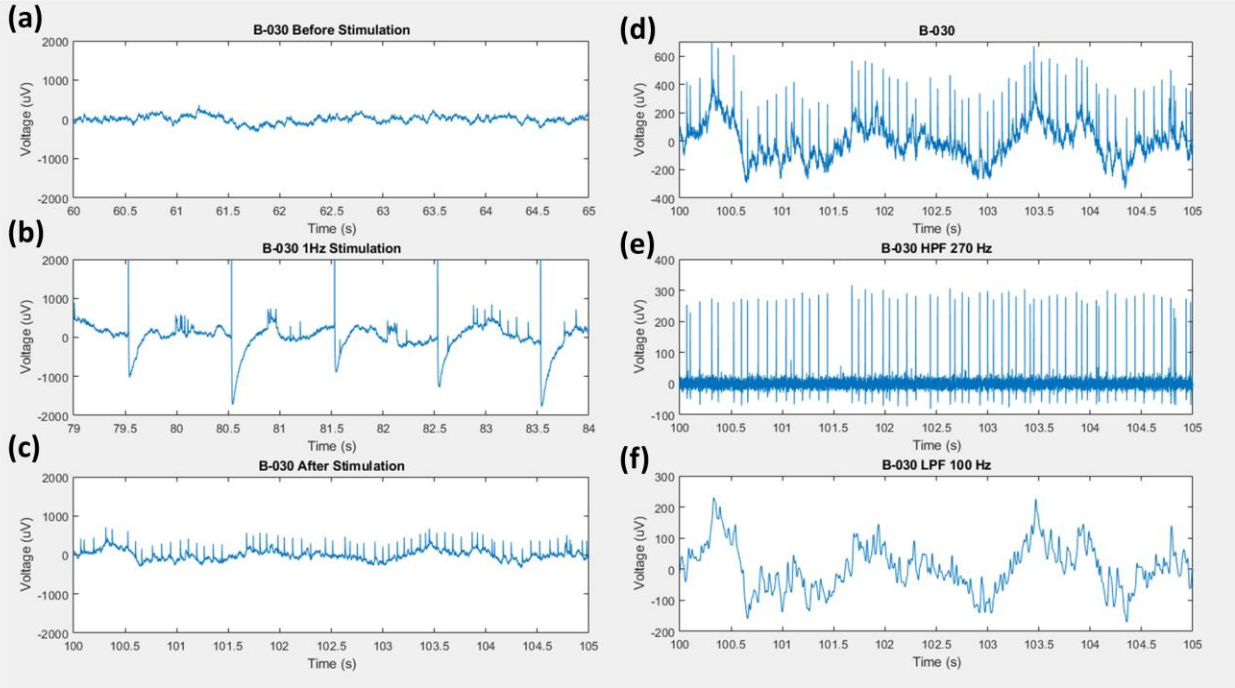

Figure 3.18 (a) the neuron activity before stimulation. (b) neuron activity during stimulation. (c)(d) the neuron activity after stimulation. (e) HPF filtered signal above 270 Hz. (e) LPF filtered signal below 100 Hz.

3.3.4 Pharmacological Response

Pharmacological responses were performed to validate the neuronal activities are of electrophysiological origing. Picrotoxin (PTX) is an equimolar mixture of two compounds, picrotoxinin ($C_{15}H_{16}O_6$; CAS# 17617-45-7) and picrotin ($C_{15}H_{18}O_7$; CAS# 21416-53-5). Due to its interactions with the inhibitory neurotransmitter $GABA_A$, PTX acts as a stimulant for the neurons and causes neurons generate high-frequency action potentials [15]. Tetrodotoxin (TTX) is a sodium gate channel blocker. Due to it binding to the voltage-gated sodium channels in neuronal membranes, it blocks the passage of sodium ions (sodium ions are responsible for the rising phase of an action potential) into the neuron, it finally inhibits the firing of action potentials in neurons [16]. We recorded the baseline activities of rat cortical neurons on 7 DIV in **Figure**

3.19 (a), which showed some action potentials in channel A003. Then, we pipetted PTX (50 μM, 1μL) to the culture medium, and the neuronal activities increased and generated high-frequency action potentials due to the application of PTX to the culture medium blocks $GABA_A$ receptor–mediated inhibition **Figure 3.19 (b)**. TTX (50 μM, 1μL) were pipetted to the culture medium after the PTX and the activity decreased until it disappeared **Figure 3.19 (c)**.

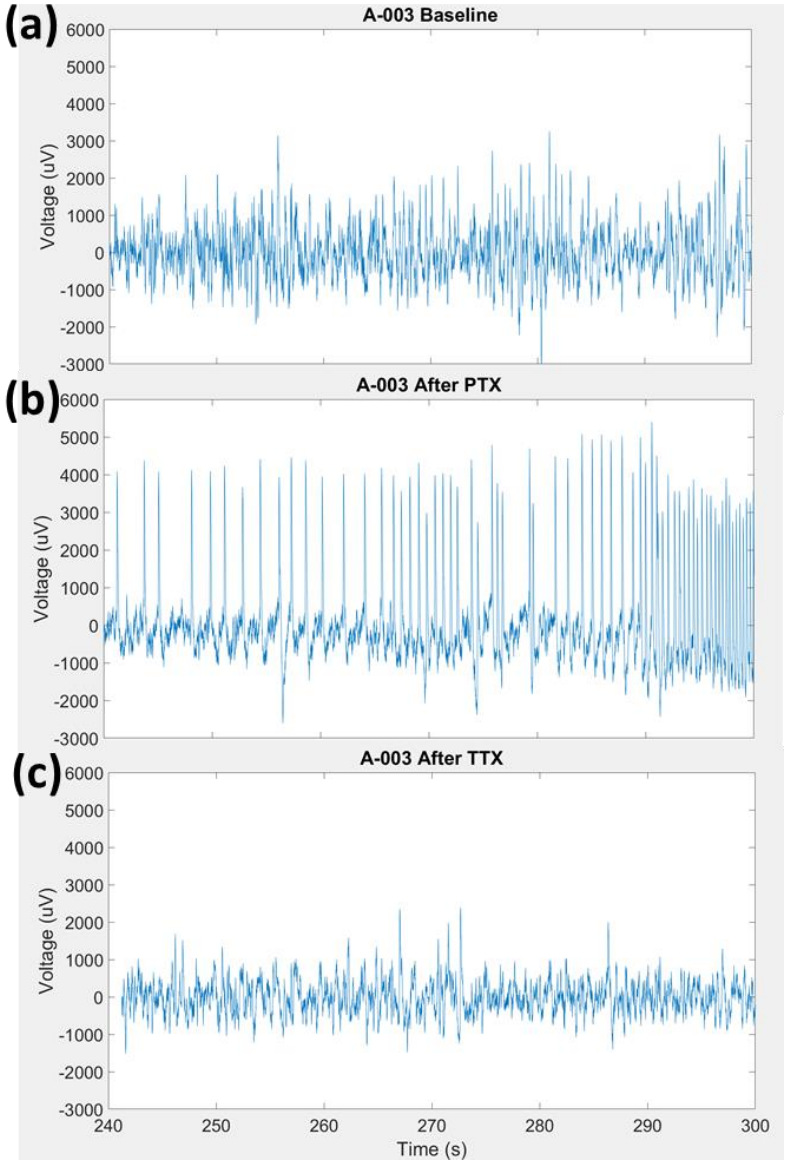

Figure 3.19 Pharmacological Response: (a) baseline activities of rat cortical neurons on 7 DIV. (b) neuronal activities responded to PTX (50 μM, 1μL) pipetted to the culture medium. (c) neuronal activities responded to TTX (50 μM, 1μL) pipetted to the culture medium.

3.3.5 Cross-section Scanning Electron Microscopy for Neuron-Nanowire Interface

The surface of the devices were passivated with a dual layer of SiO_2 (bottom) and biocompatible parylene C (top), which was exposed to a brief O_2 plasma treatment to roughen the surface to improve neuronal adhesion and network formation of rat primary cortical neurons. We recorded action potentials with clear spike trains and EPSP from rat cortical neurons on 7 DIV, validated by the electrical stimulation and pharmacological response test as discussed in section **3.3.2-3.3.4**. Then, we used cell fixation and SEM/FIB sample preparation process in **3.2.11** to prepare the SEM/FIB samples, shown in **Figure 3.20**. The neuronal somas exhibited nearly spherical structures, arranged in multi-layers with extended neurites (**Figure 3.20 (a), (c)**). Satellite-like 3D islands with neuronal fiber interconnects were formed (**Figure 3.20 (b)**). These cell culture features are indicative of the devices' excellent biocompatibility. Sequential slicing by a focused ion beam in the nanowire arrays revealed that the nanowires penetrated the soma of neurons in the bottom neuronal layer (**Figure 3.20 (d), (e)**). The cell body rested on the bi-layer passivation bi-layer of SiO_2/ Parylene C providing a stable nanowire-neuron interface for recording intracellular potentials for the duration of our experiments. **Figure 3.20 (f)** shows four nanowires interfacing with large neuronal network.

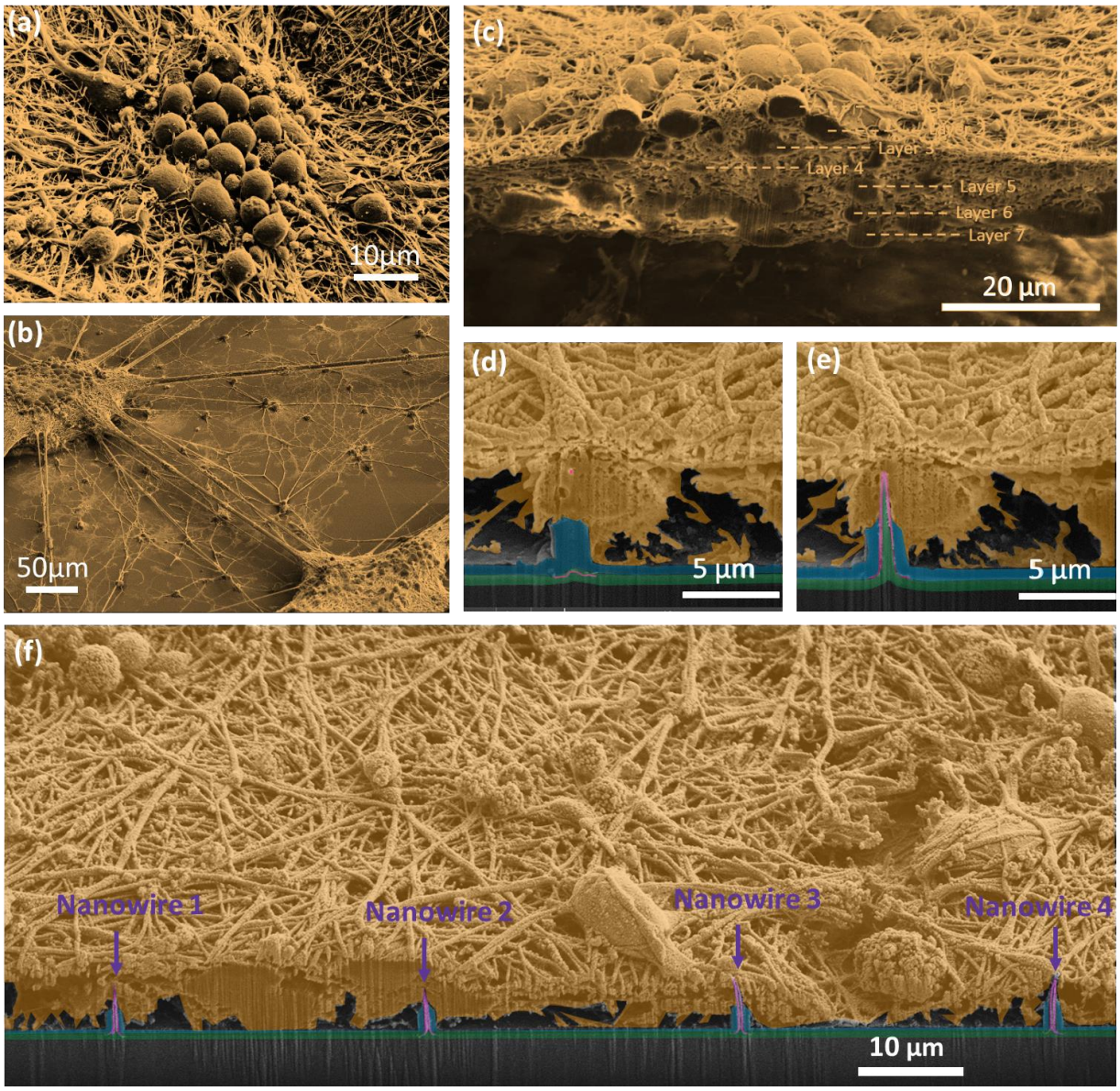

Figure 3.20 SEM images of the cultured neurons showing (a) nearly spherical neuronal somas, (b) neuronal fiber interconnects formed between satellite-like 3D islands, (c) arranged in multi-layers with extended neurites. (d-e) Sequential FIB cutting of nanowire-neuron interface revealing nanowire penetration into the cytoplasm of neurons. (f) FIB cutting of 4 nanowire-neuron interfaces.

3.3.6 The Importance of Individual Electrical Addressability

We utilized two different types of vertical nanowire arrays that have a single nanowire per channel (**Figure 3.21 (a)** and **(b)**) or 16 nanowires per channel (**Figure 3.21 (c)** and **(d)**). Electrophysiological recordings were preformed 7 days in vitro (DIV) from cultured rat primary cortical neurons. While both platforms showed clear spike trains, the peak amplitude of the recorded action potentials from single nanowires were as large as ~9mV (**Figure 3.21 (e)**), and that from multiple nanowires were ~ 300μV (**Figure 3.21 (f)**), which is 300 times smaller without accounting for potential clipping due to the amplifier range of ±5mV.

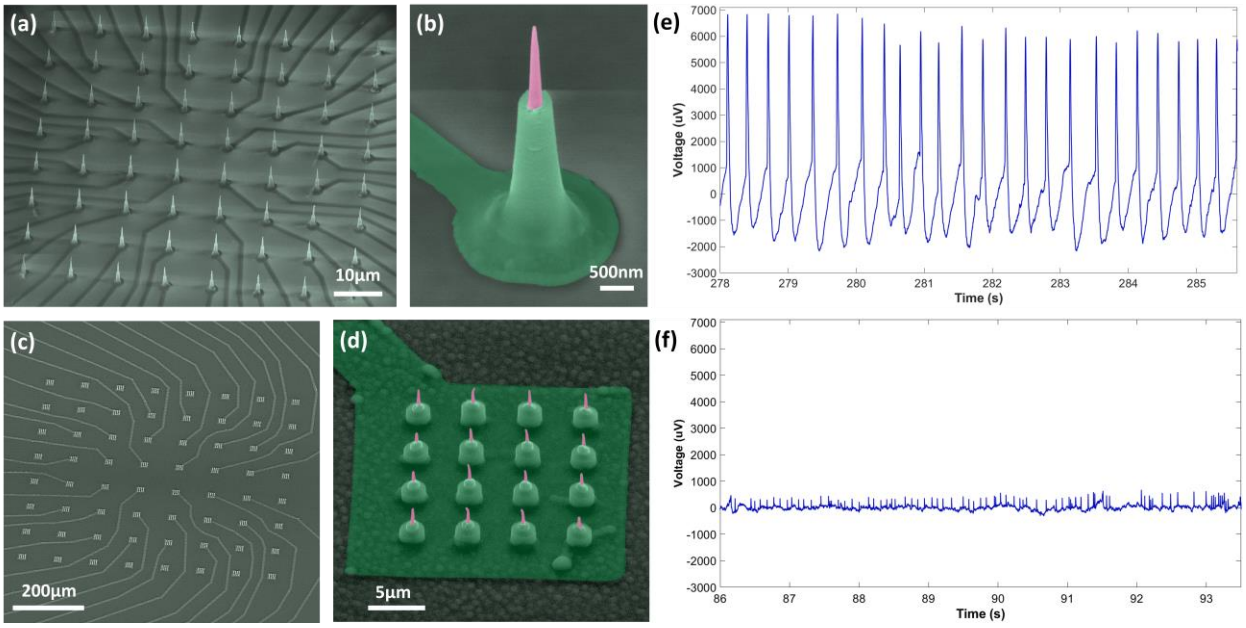

Figure 3.21 Single versus multiple nanowires per electrode. SEM images of (a-b) single nanowire per pad and (c-d) 4 by 4 multiple nanowire per pad electrode arrays. Recorded spike train of action potentials from (e) single nanowire and (f) multiple nanowire per pad electrode.

The benefit for recording large signals from the neurons is to measure the true intracellular potential changes. The recorded spike train of action potentials from individually addressable nanowires show intracellular features, and clear EPSPs, whereas the spike train recoded from

multiple nanowires did not show these features. These experimental results are in good agreement with the modeling results (section **3.3.6**) that predicted exponential decay for the amplitude of recorded spikes with the number of extracellular nanowires per single channel.

3.3.7 Electrical Model of Multi-nanowires and Individually Addressable Nanowire per Channel

It is well-known that the nature of the geometrical configuration of the nanowire-neuron interface strongly influences the electrophysiological recordings made by nanowires.[17-21] These various configurations can produce different distortions in terms of amplitude and temporal response of the neuronal signal. The discussion is expanded here building off of the investigations by Hai et al. [17] to experimental paradigms in which electrodes with multiple nanowires were used. [22-24] As illustrated in **Figure 3.22**, the neuron is modeled by two lumped membrane impedances, one of which is active contributing to ionic current flow and is denoted as a junctional membrane (right) and the other is passive depicting leakage across the cellular membrane and denoted as a non-junctional membrane (top). Because the ground for this circuit model exists some distance away from the cell, thus there exists some non-zero electrical impedance between the outside of the cell and ground. This impedance is modeled as a spreading resistance (R_{spread}) of the extracellular medium which can hold some non-zero potential when the neurons transmembrane potential is perturbed from the resting potential, i.e. is active and current flows through the cell membrane. This potential across R_{spread} can lead to a reversal in the measured potential polarity from positive to negative resulting from an opposite change in ionic charge polarity at the active membrane junction. The electrochemical interface between the intracellular fluid and the intracellular nanowire is usually modeled as a simple parallel RC circuit (R_{EC}, C_{EC}), and the quality

of the membrane seal around this penetrating electrode is modeled with a sealing resistance R_{seal}. Finally, depending on the cell geometry, extracellular fluid conductance, and other factors, there may exist a signal pathway between the non-junctional extracellular region and the junctional extracellular region. We introduce here an isolation resistance (R_{iso}) to capture this effect.

For the case where more than one nanowire is fabricated on a single pad, we illustrate in **Figure 3.22 (b)** such a situation wherein one nanowire penetrates the neuron, while the other sits outside. This modelling is important in analyzing situations where a neuron only partially the nanowires on a single pad. While numerous prior efforts focused on nanowire-neuron interfaces with multiple nanowires on a single pad, [22-24] the impact of presence of multi-wires, some inside and some outside the cells, have not been modeled, studied, or discussed before. Here, we capture the situation with an extracellular nanowire that is in close proximity to a lumped model of the junctional portion of the membrane which contributes to the transmembrane ionic current. The parameter R_{seal2} models the surrounding cell engulfment at this junction, and R_{spread} models the spreading resistance to a distant reference point away from the cell.

One can intuitively deduce that the amplitude of the recorded signals will be attenuated in this latter configuration, because we are effectively shorting the neuron's transmembrane potential. This intuition is supported by **Figure 3.22 (d)**, where the simulated potential at the input of the amplifier is plotted for various numbers of extracellular nanowires on a single pad. One can observe that the amplitude of the waveform is largest in the case of a single intracellular nanowire with zero extracellular nanowires shorted on the same pad and decreases as more nanowires are added. Furthermore, in **Figure 3.22 (e)**, the coupling coefficient which we define as the ratio of the potential seen by the amplifier over the peak intracellular potential, decays exponentially with increasing number of extracellular nanowires. We also introduce here a temporal spreading

coefficient, which is defined as the ratio of pulse widths of the simulated signal at the input to the amplifier over the intrinsic width of the unperturbed potential inside the neuron. To the first order, this coefficient can provide insight into the frequency-dependent signal distortion and is shown to decrease with the number of nanowires per pad. These simulation results agree well with experimental results that are presented in **Figure 3.21**, which compare electrophysiological recordings from neuronal cells using a single nanowire and multiple nanowires on a single pad.

The most critical parameters that can affect the signal seen by the amplifier are the parasitic capacitance (C_p), R_{seal}, R_{EC} and C_{EC}. **Figure 3.22 (f)** shows the impact of C_p on the signal distortion. From **Figure 3.22 (a)**, one can see that C_p and C_{amp} form an effective capacitive load, which, together with R_{EC} and C_{EC}, forms a voltage divider. Thus, with increasing C_p, we see a sharp decrease in coupling coefficient as this load impedance shunts the amplifier input more strongly towards ground. It is straightforward to deduce from **Figure 3.22 (f)** that C_p is a critically important parameter that should be minimized for optimal recordings. Since the load is purely capacitive, one expects that this effect would be frequency dependent. In fact, this is why we also see an increase in the temporal spreading coefficient, because as C_p increases, it results in a lower impedance path to ground for higher frequencies, thus higher frequencies are attenuated more strongly.

R_{seal} is another critical part of the nanowire-neuron interface and its effect on signal distortion is illustrated in **Figure 3.22 (g)**, R_{seal} forms a separate signal path to ground and thus produces a loading effect on the electrophysiological signal source similar to the intracellular electrode. If the value of R_{seal} is large compared to other signal paths from inside the cell to ground, then it will produce negligible signal distortion. As R_{seal} approaches similar orders of magnitude to the primary signal path's impedance we begin to see a sharp decrease in amplitude at the

amplifier input as current is redirected away from the electrode towards this leakage path. In the extreme, the amount of current flowing through the electrode actually becomes negligible compared to this leakage path, thus the voltage drop across the electrode interface becomes very small, and we begin to see the measured signal begin to match the true intracellular potential. However, what this circuit model does not account for is that a decreasing R_{Seal} will likely compromise the physiological functioning of the cell as shown by the rapid decrease in intracellular peak amplitude below R_{Seal} value of 109 Ω in **Figure 3.22 (g)**.

The impact of the parallel RC electrode impedance, R_{EC} and C_{EC}, has on signal distortion is shown in **Figure 3.22 (h)** and **(i)** where each contour line indicates the log of the magnitude of impedance at 1kHz (commonly used frequency that represents the frequency content of an action potential58) as a function of R_{EC} and C_{EC}. It is customary to report magnitude of impedance at 1kHz. However, **Figure 3.22 (h)** and **(i)** clearly demonstrate that two intracellular electrodes with equivalent 1kHz impedance can have dramatically different coupling efficiency depending on whether the impedance is Faradaic or capacitive dominant. For example, if we have a 1kHz impedance magnitude between 10M and 100M, the more Faradaic-like electrodes will likely have a higher coupling efficiency and lower temporal spreading coefficient compared to a more capacitive-like electrode.

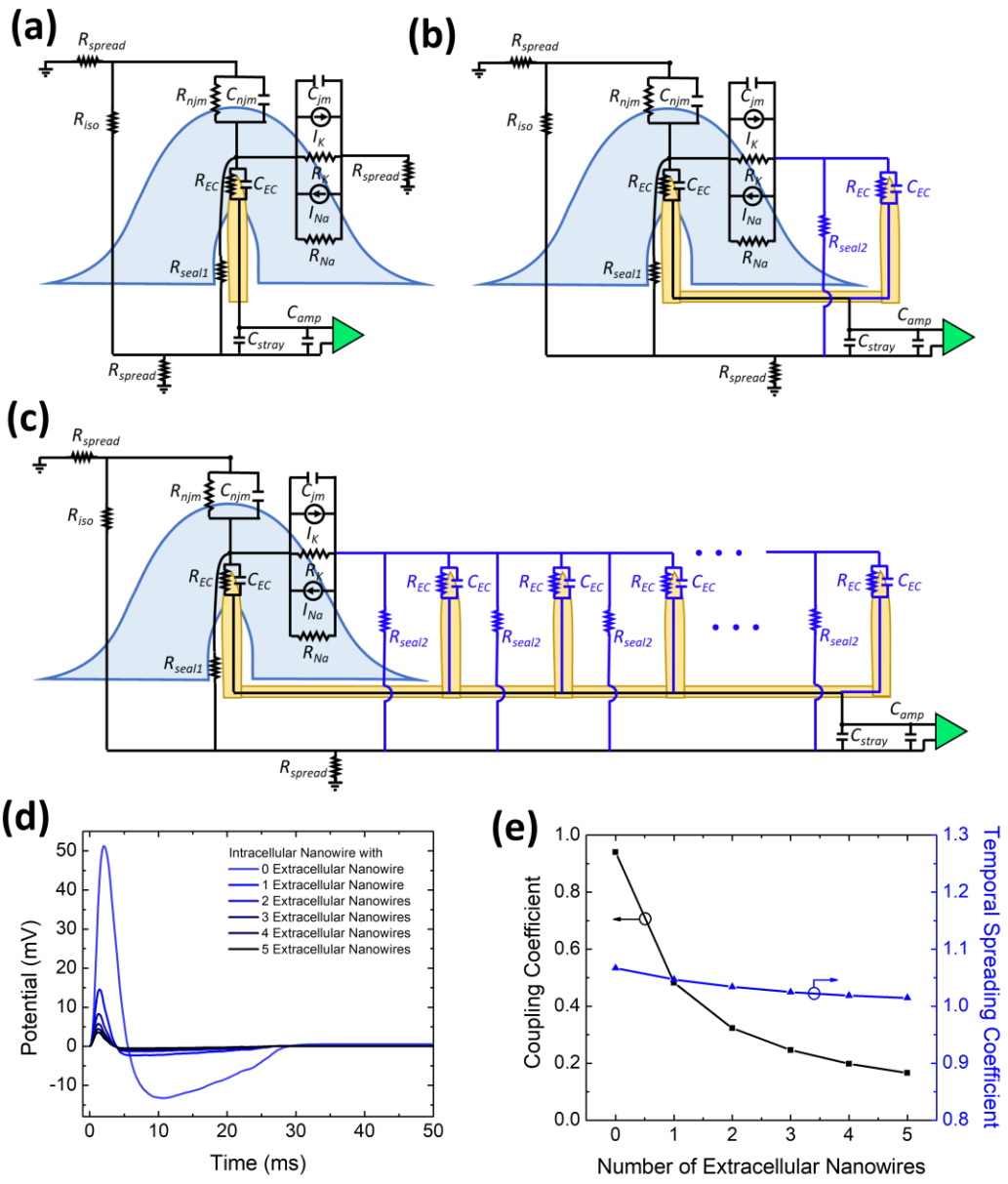

Figure 3.22 Modelling nanowire-neuron junction. Circuit diagram of (a) single nanowire penetrating a cell and (b) two nanowires with partially engulfed in a cell. (c) multiple nanowires with partially engulfed in a cell. (d) Simulated action potential at the input of the amplifier plotted for various numbers of extracellular nanowires on a single pad. Coupling and temporal spreading coefficients with (e) increasing number of extracellular nanowires and (f) parasitic capacitance. (g) Seal resistance dependent peak amplitude and pulse width of action potential inside the cell and at the input of the amplifier. Mapping of the coupling (h) and temporal spreading coefficients (i) depending on the REC and CEC of the nanowire electrode.

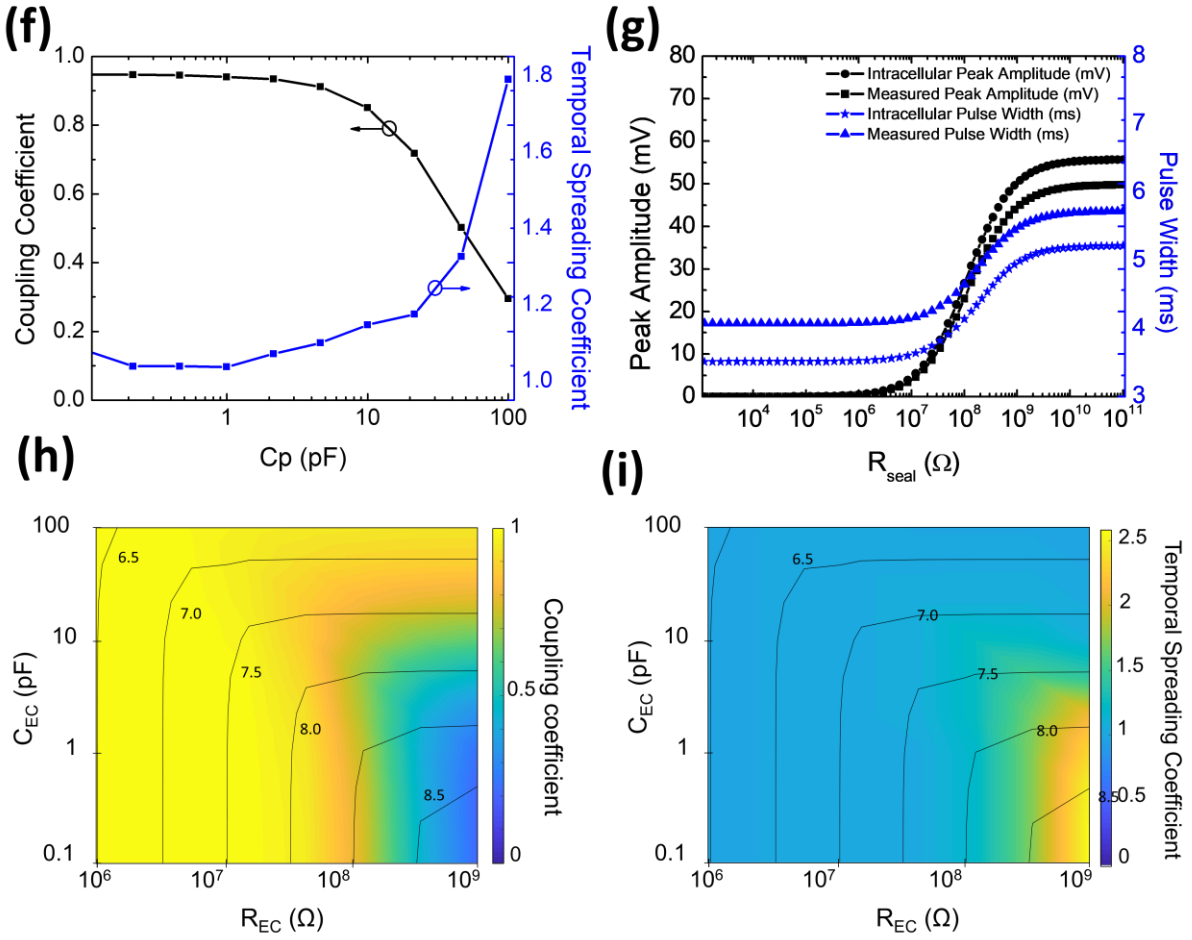

Figure 3.22 Modelling nanowire-neuron junction. Circuit diagram of (a) single nanowire penetrating a cell and (b) two nanowires with partially engulfed in a cell. (c) multiple nanowires with partially engulfed in a cell. (d) Simulated action potential at the input of the amplifier plotted for various numbers of extracellular nanowires on a single pad. Coupling and temporal spreading coefficients with (e) increasing number of extracellular nanowires and (f) parasitic capacitance. (g) Seal resistance dependent peak amplitude and pulse width of action potential inside the cell and at the input of the amplifier. Mapping of the coupling (h) and temporal spreading coefficients (i) depending on the REC and CEC of the nanowire electrode. (continuous)

3.3.8 Cardiomyocyte Recording and Microscopy

CMs were cultured on our platform with the culture process were described in section **3.2.10**. CMs activities were recorded 5 DIV (**Figure 3.23**), since CMS started to beat on 5 DIV. In **Figure 3.23**, we recorded CMs' activities show clear spike train of pacemaker action potential

with clear phase 4, 0 and 3 for sinoatrial nodal cells. Phase 4 is related to hyperpolarization of cell membrane with activation of slow Na^+ channels, slow Na^+ entry and the intracellular potential slowly increasing until reach the Ca^+ voltage-gated threshold potential, the phase 0 starts with the Ca^+ gate open and fast Ca^+ flow entry inside of the cell with causing depolarization of the cell membrane. Then, with phase 3 starting, Ca^+ channels close and K^+ channels open with slow K^+ exit of the cell and cell membrane repolarization. Our CM's pacemaker action potential showed a beating frequency of ~70 beats per minute, which is closed to the frequency of sinoatrial nodal cells in human body (72 beats per minute).

By using the cell fixation and SEM sample preparation process in section **3.2.11**, we fixed the cells on 5 DIV and the SEM images of the CMs and nanowires shows in **Figure 3.24**, where **Figure 3.24 (a)** shows large CMs network on top of the nanowire array, **Figure 3.24 (b)** shows zoom in SEM image of CMs and **Figure 3.24 (c)** shows zoom in SEM image of the CMs on top of the nanowires. The CMs are healthy and have stable interface with nanowires.

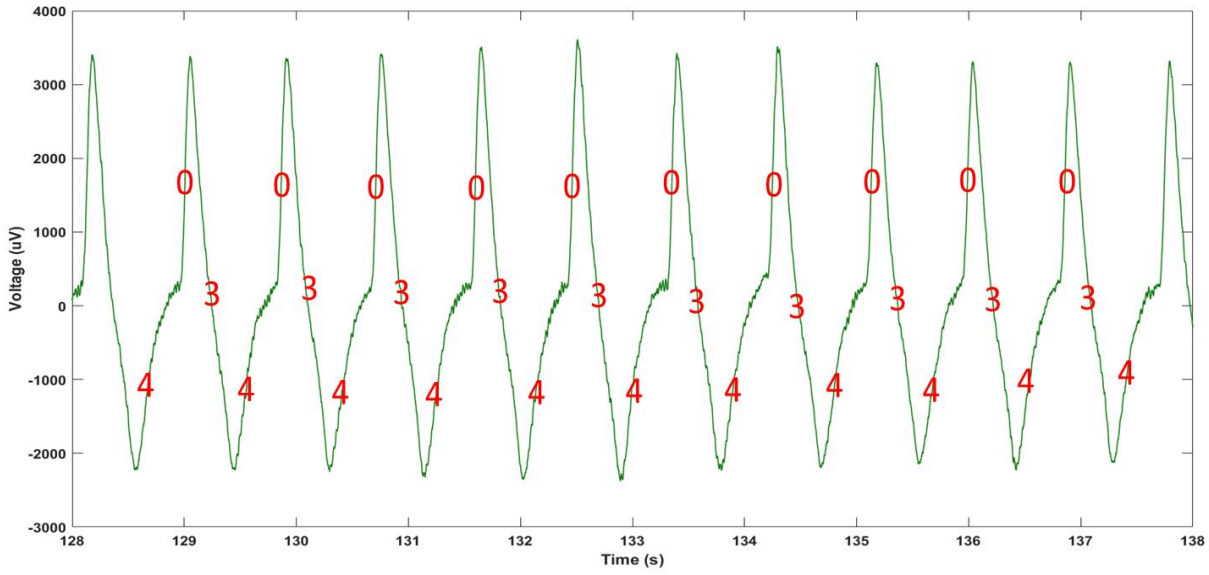

Figure 3.23 CM's pacemaker action potential.

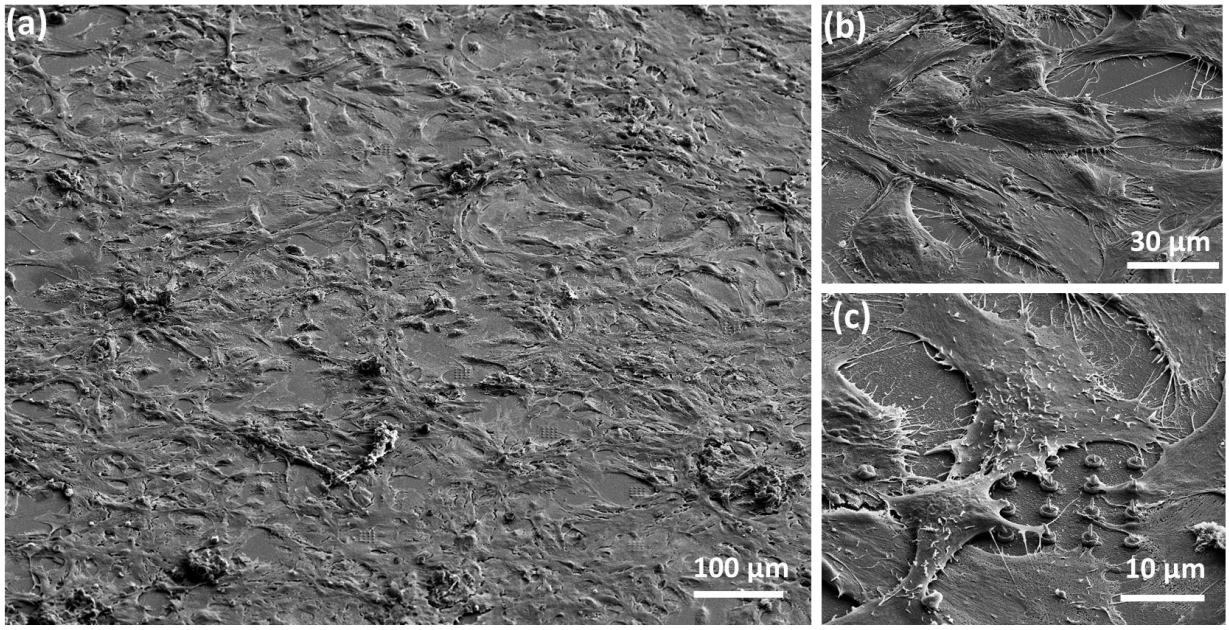

Figure 3.24 CMs SEM images: (a) overview SEM image of CMs on the nanowire arrays. (b) Zoomed-in SEM image of the CMs. (c) Zoomed-in SEM image of CMs on the nanowire arrays.

3.4 Conclusions

We designed and developed a new fabrication method that offers for the first time an ultra-sharp sub-10nm nanowire array for individually addressable intracellular mapping of large neuronal networks and cardiac tissue. With the surface roughness modification of bi-dielectric layers of SiO_2 and Parylene C, the devices showed superb bio-compatibility, validated by the culture of neurons and cardiomyocytes. The ultra-sharp tip enableed natural permeation into neuronal cell membranes without electroporation, popularly used by all other works in this field. We utilize these arrays to perform electrophysiological recordings from rat cortical neurons and cardiomyocytes. Our recordings demonstrated isolated action potentials and spike trains with high

signal-to-noise ratios that can be modulated with pharmacology and electrical pulses. Significantly, we observed clear spontaneous excitatory postsynaptic potential (EPSP) prior to the larger spike trains. The interfaces of our nanowires with cultured neurons were characterized by SEM/FIB revealing multi-layer 3D neuronal tissue with nanowires clearly penetrating the neuron's soma. Detailed electrical modeling and simulation was employed to signify the importance of individual electrical addressability for efficient high signal-to-noise ratios compared to multi-nanowires per electrode. The simulation results were in good agreement with our experimental investigations in which we intentionally increased the number of nanowires per channel and observed over 10X reduction in the recorded signal amplitudes. Our platform is scalable in terms of channel count and area coverage and recordings with 1024 channels from 3D cell culture and minibrains are underway. Overall, our platform paves the way for longitudinal electrophysiological experiments on synaptic activity in human iPSC based disease models of neuronal networks, critical for understanding the mechanisms of neurological diseases and for developing drugs to treat them.

Most of chapter 3 is currently being prepared for submission for publication. R. Liu, A. Bourhis, G. Robin, A. D'Antonio-Chronowska, Y. Tchoe, K. Frazer, A. G. Bang and S. A. Dayeh. The dissertation author will be the first author of this paper.

3.5 References

1. L. Chen, V. Luciani, H. Miao, Effect of Alternating Ar and SF6/C4F8 Gas Flow in Si Nano-Structure Plasma Etching, Microelectronic Engineering, 2011, 88, 8, 2470-2473.

2. H. Z. Massoud, J. D. Plummer, and E. A. Irene, Thermal oxidation of silicon in dry oxygen: Accurate determination of the kinetic rate constants. Journal of the Electrochemical Society, 132(7):1745-1757, 1985.

3. H. Z. Massoud, J. D. Plummer, and E. A. Irene, Thermal oxidation of silicon in dry oxygen: Growth - rate enhancement in the thin regime II. Physical mechanisms. Journal of The Electrochemical Society, 132(11):2693-2700, 1985.

4. S. P. Khan, G. G. Auner, G. M. Newaz, Influence of nanoscale surface roughness on neural cell attachment on silicon. Nanomedicine: Nanotechnology, Biology, and Medicine 1(2005) 125-129.

5. S. Bonde, T. Berthing, M. H. Madsen, T. K. Andersen, N. Buch-Månson, L. Guo, X. Li, F. Badique, K. Anselme, J. Nygård, K. L. Martinez, Tuning InAs Nanowire Density for HEK293 Cell Viability, Adhesion, and Morphology: Perspectives for Nanowire-Based Biosensors, ACS Appl. Mater. Interfaces 2013, 5, 21, 10510−10519.

6. M. Ganji, A. T. Elthakeb, A. Tanaka, V. Gilja, E. Halgren, and S. A. Dayeh, Scaling Effects on the Electrochemical Performance of PEDOT: PSS, Au, and Pt for Electrocorticography Recording, Advanced Functional Materials, Vol. 27, (2017), 1703018.

7. I. Uguz, M. Ganji, A. Hama, A. Tanaka, S. Inal, A. Youssef, R. M. Owens, S. A. Dayeh, and G. G. Malliaras, "Autoclave Sterilization of PEDOT: PSS Electrophysiology Devices," Advanced Healthcare Materials, Vol. 5, No. 24 (Dec 2016), pp. 3094-3098.

8. M. Asplund, E. Thaning, J. Lundberg, A. Sandberg-Nordqvist, B. Kostyszyn, O. Inganäs, H. von Holst, Toxicity evaluation of PEDOT/biomolecular composites intended for neural communication electrodes, Biomedical Materials 2009, 4, 045009.

9. D.-H. Kim, J. A. Wiler, D. J. Anderson, D. R. Kipke, D. C. Martin, Conducting polymers on hydrogel-coated neural electrode provide sensitive neural recordings in auditory cortex. Acta Biomater. 2010 Jan;6(1):57-62.

10. L. Groenendaal, F. Jonas, D. Freitag, H. Pielartzik, J. R. Reynolds, Poly(3,4‐ethylenedioxythiophene) and Its Derivatives: Past, Present, and Future. Advanced Materials 2000, 12, 481.

11. J. Rivnay, S. Inal, B. A. Collins, M. Sessolo, E. Stavrinidou, X. Strakosas, C. Tassone, D. M. Delongchamp, G. G. Malliaras, Structural control of mixed ionic and electronic transport in conducting polymers. Nature communications, 2016 Apr 19;7:11287.

12. M. R. Abidian, D. C. Experimental and theoretical characterization of implantable neural microelectrodes modified with conducting polymer nanotubes. Martin, Biomaterials, 2008 Mar;29(9):1273-83.

13. M. A. Svirsky, A. M. Robbins, K. I. Kirk, D. B. Pisoni, and R. T. Miyamoto, Language development in profoundly deaf children with cochlear implants, Psychological science, vol. 11, pp. 153-158, 2000.

14. A. D'Antonio-Chronowska, M. K.R. Donovan, W. W. Young Greenwald, J. P. Nguyen, K. Fujita, S. Hashem, H. Matsui, F. Soncin, M. Parast, M. C. Ward, F. Coulet, E. N. Smith, E. Adler, M. D'Antonio, and K. A. Frazer, Association of Human iPSC Gene Signatures and X Chromosome Dosage with Two Distinct Cardiac Differentiation Trajectories. Stem Cell Reports, Vol. 13, 924–938, November 12, 2019.

15. J. Tønnesen, A. T. Sørensen, K. Deisseroth, C. Lundberg, and M. Kokaia, Optogenetic control of epileptiform activity. PNAS July 21, 2009 106 (29) 12162-12167.

16. V. Bane, M. Lehane, M. Dikshit, A. O'Riordan, A. Furey, Tetrodotoxin: chemistry, toxicity, source, distribution and detection. Toxins (Basel). 2014 Feb 21;6(2):693-755.

17. M.E. Spira and A. Hai, Nat. Multi-electrode array technologies for neuroscience and cardiology. Nanotechnol. **8**, 83 (2013).

18. D.R. Kipke, W. Shain, G. Buzsáki, E. Fetz, J.M. Henderson, J.F. Hetke, and G. Schalk, Advanced neurotechnologies for chronic neural interfaces: new horizons and clinical opportunities. J. Neurosci. 28, 11830 (2008).

19. J.T. Robinson, M. Jorgolli, A.K. Shalek, M.H. Yoon, R.S. Gertner, and H. Park, Vertical nanowire electrode arrays as a scalable platform for intracellular interfacing to neuronal circuits. Nat. Nanotechnol. 7, 180 (2012).

20. A. Aalipour, A.M. Xu, S. Leal-Ortiz, C.C. Garner, and N.A. Melosh, Plasma membrane and actin cytoskeleton as synergistic barriers to nanowire cell penetration. Langmuir 30, 12362 (2014).

21. X. Duan, R. Gao, P. Xie, T. Cohen-Karni, Q. Qing, H.S. Choe, B. Tian, X. Jiang, and C.M. Lieber, Intracellular recordings of action potentials by an extracellular nanoscale field-effect transistor. Nat Nanotechnol. 2011 Dec 18;7(3):174-9.

22. C. Xie, Z. Lin, L. Hanson, Y. Cui, and B. Cui, Intracellular recording of action potentials by nanopillar electroporation. Nat. Nanotechnol. 2012 Feb 12;7(3):185-90.

23. J. Abbott, T. Ye, K. Krenek, R.S. Gertner, S. Ban, Y. Kim, L. Qin, W. Wu, H. Park, and D. Ham, A nanoelectrode array for obtaining intracellular recordings from thousands of connected neurons. Nat. Biomed. Eng. (2019).

24. D.B. Suyatin, L. Wallman, J. Thelin, C.N. Prinz, H. Jörntell, L. Samuelson, L. Montelius, and J. Schouenborg, Nanowire-based electrode for acute in vivo neural recordings in the brain. PLoS One 8, 1 (2013).

Chapter 4

Post-CMOS Processing of Nanowire Arrays for Electrophysiological Imaging and Stimulation

4.1 Introduction

To develop novel power-efficient, simultaneous, compact and portable tools that enable large scalability and high spatiotemporal resolution for recording of neuronal activity, especially intracellular action potentials, is one of the primary goals for advancing neurophysiology studies from single neuron to the brain. As noted earlier, the patch-clamp is the gold standard procedure for studying neuronal activity with high sensitivity but is generally restricted to single or few cells and is destructive, [1-5] while microelectrode arrays enable recordings from networks of neurons, but they lack the sensitivity to subthreshold potentials that are critical electrophysiological features for drug screening. [6] Nanowires offer potential for: intracellular recordings and sensitivity to subthreshold potentials, less-destructive interaction, scalability to interface with neuronal networks, [7-10] while complementary metal-oxide semiconductor (CMOS) integrated circuits (IC) has the ability of high power-efficiency, large scalability, simultaneousness and compactness. By combining the nanowire with CMOS IC, it will realize a high-fidelity, high-throughput, simultaneous intracellular recording at the large neuronal network level [11-12]. Although significant advances have been made by combining nanowires with CMOS IC, full system

integration for low-power operation and high-density has not been achieved. Here, we utilize a new system-on-chip integrating nanowire electrodes and all acquisition and control functions, illustrated in **Figure 4.1** and designed by Dr. J. Wang in Prof. G. Cauwenberghs' group from Bioengineering at UCSD. The size of chip is 2.236 mm × 2.236 mm, which integrated 256 sensor channels in the center, 4 reference electrodes in each corner and 17 x 4 periphery pads for input/output (I/O). Each sensor channel includes an analog front-end (AFE) for simultaneous current stimulation and voltage recording, a data reading block and a continuous comparator, so each sensor channel can be configured as either voltage clamp mode or current clamp mode. To integrate the nanowire array on the small CMOS IC chip is challenging. In this chapter, I will introduce two CMOS-compatible and bio-compatible methods by using Focus Ion Beam (FIB) to integrate ultra-sharp nanowires on the IC chip to realize the neuron network recording and pharmacological responsive test.

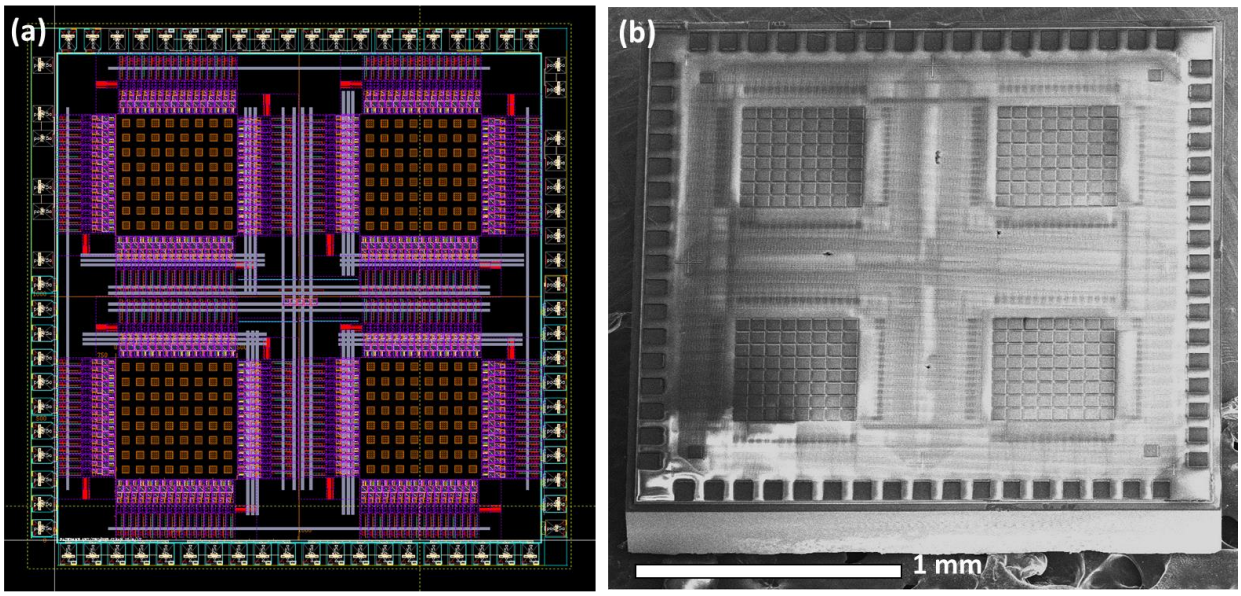

Figure 4.1 The overview of the CMOS chip (a) design pattern. (b) SEM image of the dice.

4.2 Experimental

4.2.1 Cross-sectional SEM-EDS Elemental Mapping

Determining the layout of the CMOS chip is significant to integrate nanowires and connecting them electrically to the chip. SEM-EDS elemental mapping was performed to define the layout at the cross0section of the center of the chip, where shows the elemental distribution of Si, O, Al and N, respectively in **Figure 4.2 (a)**, and SEM image of the cross-section of the CMOS chip in **Figure 4.2 (b)**. From top to down, the layout is 500nm Si_3N_4 and 4.2 µm SiO_2 as the surface passivation layers, 3.8 µm Al as the sensor- pad, Al electronics for amplifying and processing signals and Si as the carrier substrate.

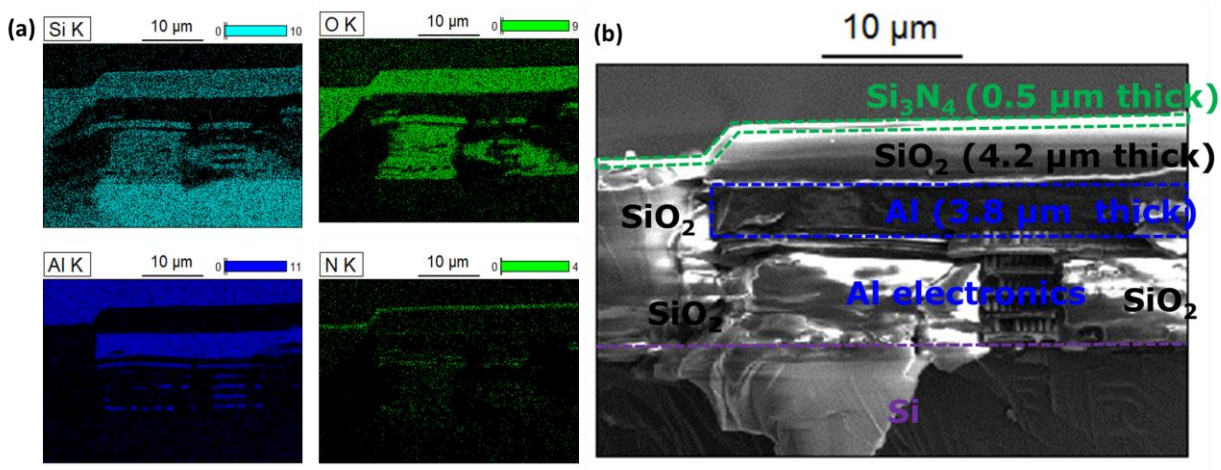

Figure 4.2 Cross-sectional SEM-EDS Elemental Mapping: (a) the elemental distribution of Si, O, Al and N, respectively. (b) SEM image of the cross-section of the CMOS chip.

4.2.2 Integrate Pt Nanowire with the CMOS Chip

The CMOS chip has double dielectric layers of SiO_2 with the thickness of 4.2 µm and Si_3N_4 with the thickness of 500nm. To integrate the nanowires with the CMOS chip, we developed two

methods of integrating nanowires with CMOS by Focused Ion Beam (FIB). The first method is to remove the double dielectric layers of SiO_2 and Si_3N_4 and to deposit the Pt nanowires (**Figure 4.3**), while the second method is to mill a cavity through the dielectric layers of SiO_2 and Si_3N_4, and to deposit the Pt nanowires (**Figure 4.4**). We used RIE (power 250 W) and combination gas of O_2 (flow: 5 sccm) and CHF_3 (flow: 5 sccm) for 60 cycles with 2 min each by Trion P80 RIE system. In the second method, to improve the adhesion of cells to the chip, we deposited a bio-compatible dielectric barrier layer of Parylene C with the thickness of 500nm. [13] Second, a 10nm Ti was deposited on the surface of the chip for electrical conduction during the Focused Ion Beam (FIB). Then, FIB was conducted by a FEI Scios DualBeam FIB/SEM system. First, ion beam with the voltage of 30kV and current of 5nA was used to etch through all the dielectric layers of Parylene C, Si_3N_4, and SiO_2, and the pattern size is a circle with the diameter of 2 μm. Second, ion beam with voltage of 30 kV and current of 1.5 pA was used to deposit a Pt nanowire at position of the milled hole. The nanowire diameter was about 200 nm and the height was about 9 μm with 4 μm above the surface the chip. We used the milling step with Ion beam (30 kV, 100 pA) to smooth the sidewall of the nanowire an ultra-sharp the tip of it, which is about 60nm. Then, we used Electron beam with the voltage of 10kV and current of 13 pA to deposit a ultra-sharp tip with the diameter of 20 nm on the Nanowire. We used the process flow above to finish all the nanowire deposition. A Reactive-ion etching (RIE: Oxford Plasmalab 80) with the combination gas of SF_6 with the flow of 45 sccm and Ar with the flow of 7 sccm was used to etch the 10 nm Ti on the surface of the chip.

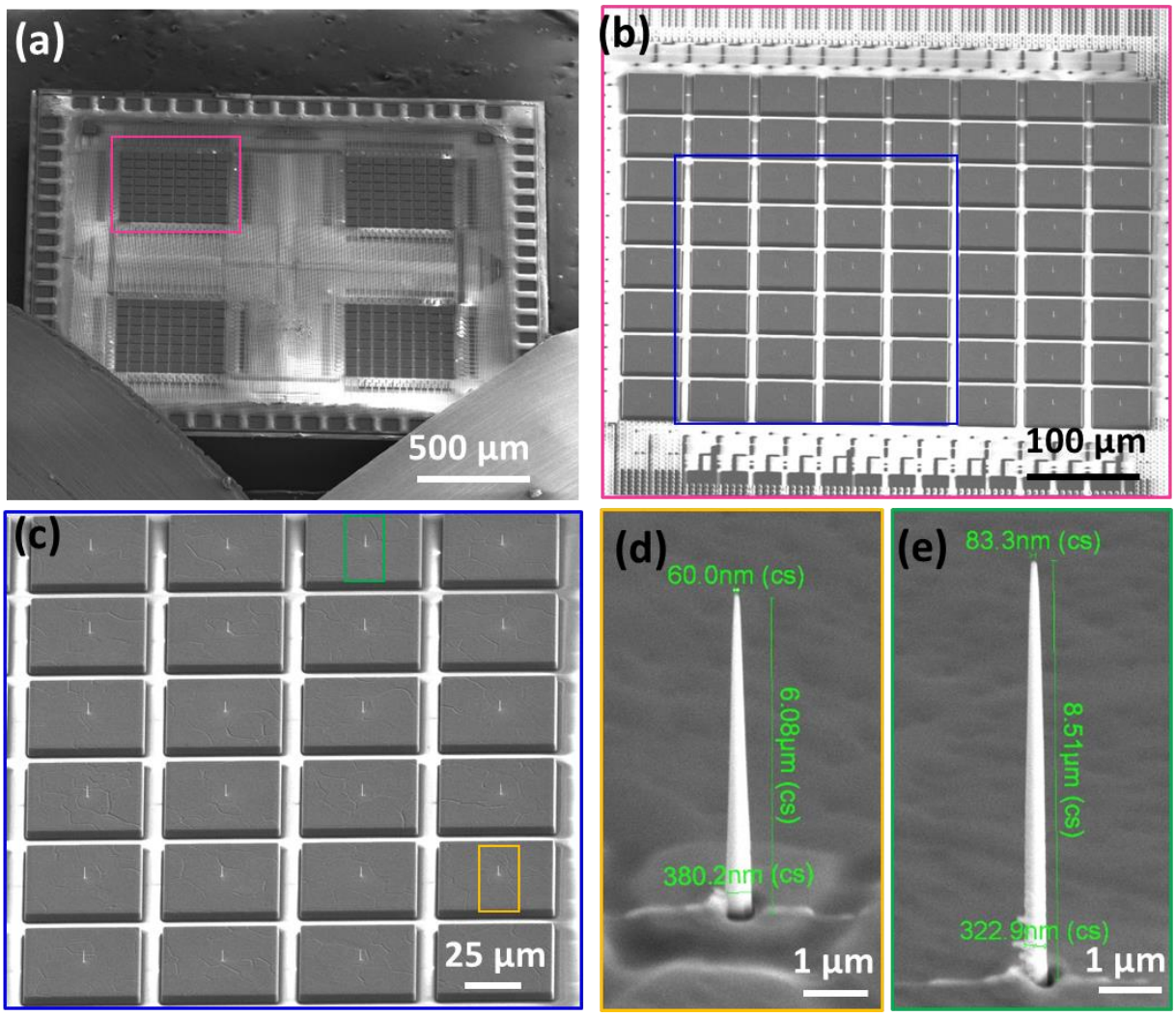

Figure 4.3 Method 1 of FIB deposition of Pt NWs on top of the CMOS chip

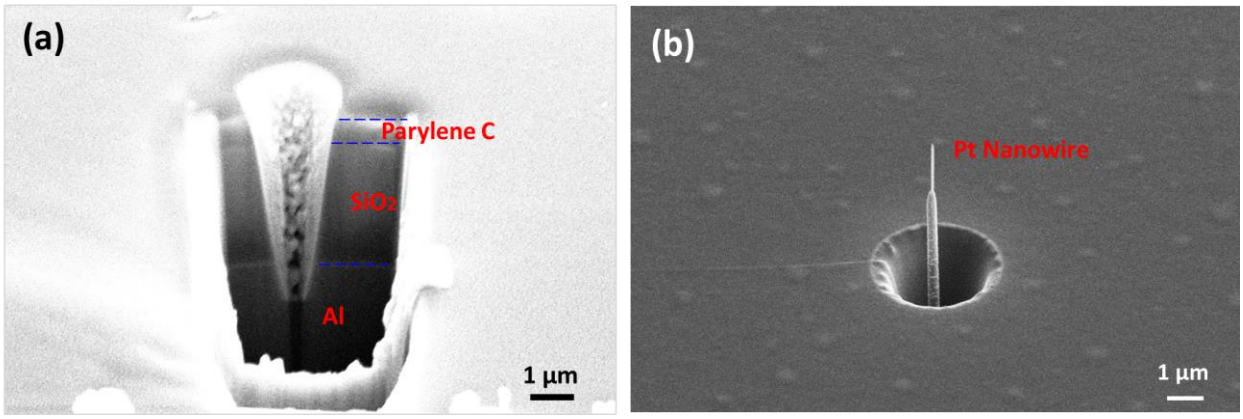

Figure 4.4 Method 2 of FIB deposition of Pt NWs on top of the CMOS chip

4.2.3 Packaging

The main agent and hardener of Polydimethylsiloxane (PDMS) are mixed in a mass ratio of 5:1 and the air bubbles in the mixture were evacuated out by vacuum. Plastic tube was bonded on the carrier substrate by using the PDMS at 100 deg C for 1hr to tight seal the interface to against fluid leakage to localize the neuron culture chamber. The overview of the final device was shown in **Figure 4.5 (b)**, where the center of the chip with 256 channels are exposed in **Figure 4.5 (a)**. Each of the pad was milled for a cave and deposited with an individually addressable Pt nanowire (**Figure 4.5 (c)** and **(d)**).

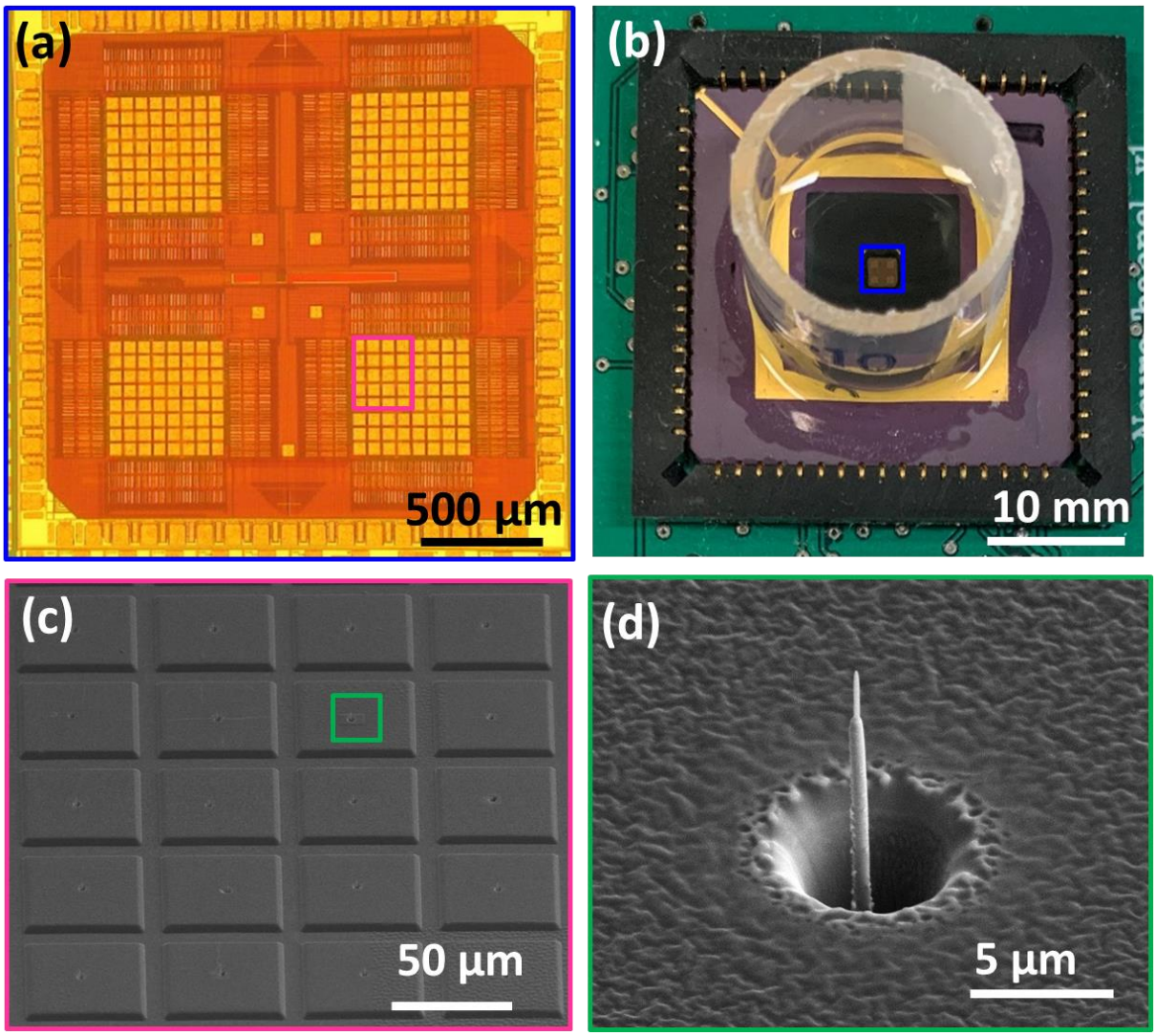

Figure 4.5 Packaging of the chip. (a) optical microscope image for the overview of the CMOS chip. (b) Plastic tube was bonded on the carrier substrate. SEM image of (c) a 5×4 nanowire array and (d) an individually addressable nanowire made by method 2.

4.2.4 Neuron culture

The cell culture of neurons followed previously discussed processes in part **2.4**. 400 k of primary rat cortical neurons were plated and cultured on the platform for 10 days in vitro (DIV). Neuronal recording and pharmacological test of KCl and TTX were performed on 7th DIV, and 10th DIV.

4.3 Results and discussion

Similar to previous recordings, the nanowires integrated on the CMOS chip resulted in recording large neuronal potentials. Pharmacological responses were performed to validate the neuron activities are action potentials. Both of PTX and TTX were applied to active and eliminate the rat cortical neurons activities for 8 DIV. We recorded the baseline activities of rat cortical neurons in **Figure 4.6 (a)**, which showed some action potentials with the amplitude of 60 mV. Then, we pipetted PTX (50 μM, 1μL) to the culture medium, and the neuronal activities increased and generated high-frequency action potentials due to the application of PTX to the culture medium blocks $GABA_A$ receptor–mediated inhibition (**Figure 4.6 (b)**). TTX (50 μM, 1μL) were pipetted to the culture medium after the PTX and the activity decreased until disappeared in 30 s (**Figure 3.19 (c)**.) Our Nanowire-CMOS platform showed pharmacological response, which validated the Pt nanowire's nature penetration property and stable interface of nanowire and cells.

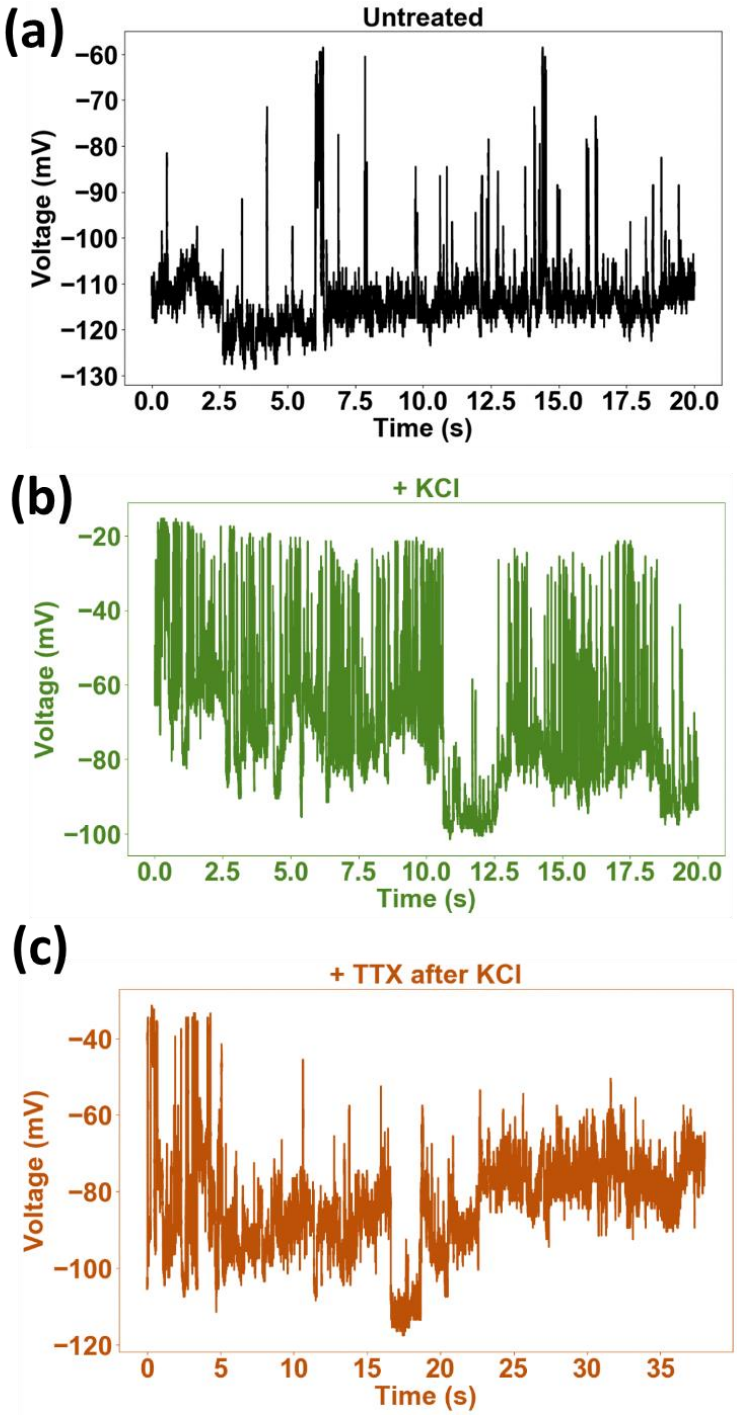

Figure 4.6 Rat cortical neuron baseline activity (a), pharmacological response to PTX (b) and to TTX (c) on 10th DIV.

4.4 Conclusions

The CMOS chip cross-section was characterized by SEM-EDS. Based on it, two FIB methods to integrate ultra-sharp nanowires with the IC chip were introduced. Then we presented the intracellular stimulation and recording through ultra-sharp-tipped Pt nanowire-needle electrode arrays. The electrophysiology system-on-chip (eSOC) performed simultaneous electrical recording and stimulation through each of the 256 electrodes, with digital control and time-multiplexed readout. The eSOC is validated by using prerecorded action potential replayed through the phosphate-buffered saline (PBS) solution and demonstrated its ability to accurately record the signals at high spatiotemporal resolution at low cross-talk. Primary rat cortical neurons were plated and cultured on the platform for 10 days in vitro (DIV). Intracellular action potentials were recorded, and validated by the pharmacological test of KCl and TTX on 7^{th} DIV, and 10^{th} DIV. With the integration of nanowires on the electrode plates of the IC chip, the eSOC enabled precise intracellular electrophysiology recording and stimulation at the large neuron network level.

4.5 References

1. E. Neher, B. Sakmann, J. H. Steinbach, The extracellular patch clamp: a method for resolving currents through individual open channels in biological membranes. Pfluegers Arch. 1978, 375 (2), 219−228.

2. M. Martina, I. Vida, P. Jonas, Distal initiation and active propagation of action potentials in interneuron dendrites. Science 2000, 287 (5451), 295−300.

3. D. Henze, G. Buzsaki, Action potential threshold of hippocampal pyramidal cells in vivo is increased by recent spiking activity. Neuroscience 2001, 105 (1), 121−130.

4. M. Scanziani, M. Häusser, Electrophysiology in the age of light. Nature 2009, 461 (7266), 930−939.

5. Z. C. Lin, B. Cui, Nanowire transistors: room for manoeuvre. Nat. Nanotechnol. 2014, 9 (2), 94−96.

6. M. E. Spira, A. Hai, Multi-electrode array technologies for neuroscience and cardiology. Nat. Nanotechnol. 2013, 8 (2), 83−94.

7. W. Kim, J. K. Ng, M. E. Kunitake, B. R. Conklin, Yang, P. Interfacing silicon nanowires with mammalian cells. J. Am. Chem. Soc. 2007, 129 (23), 7228−7229.

8. G. Piret, M.-T. Perez, C. N. Prinz, Neurite outgrowth and synaptophysin expression of postnatal CNS neurons on GaP nanowire arrays in long-term retinal cell culture. Biomaterials 2013, 34 (4), 875−887.

9. L. Hanson, Z. C. Lin, C. Xie, Y. Cui, B. Cui, Characterization of the cell−nanopillar interface by transmission electron microscopy. Nano Lett. 2012, 12 (11), 5815−5820.

10. L. Gällentoft, L. M. Pettersson, N. Danielsen, J. Schouenborg, C. N. Prinz, C. E. Linsmeier, Size-dependent long-term tissue response to biostable nanowires in the brain. Biomaterials 2015, 42,172−183.

11. J. Abbott, T. Ye, L. Qin, M. Jorgolli, R. S. Gertner, D. Ham, and H. Park, CMOS nanoelectrode array for all-electrical intracellular electrophysiological imaging, Nature Nanotechnology, vol. 12, p. 460, 2017.

12. J. Abbott, T. Ye, K. Krenek, R. S. Gertner, S. Ban, Y. Kim, L. Qin, W. Wu, H. Park, and D. Ham, A nanoelectrode array for obtaining intracellular recordings from thousands of connected neurons. Nature Biomedical Engineering, 2019.

13. M. Ganji, A. C. Paulk, J. C. Yang, N. W. Vahidi, S. H. Lee, R. Liu, L. Hossain, E. M. Arneodo, M. Thunemann, M. Shigyo, A. Tanaka, S. B. Ryu, S. W. Lee, M. Marsala, A. Devor, D. R. Cleary, J. R. Martin, H. Oh, V. Gilja, T. Q. Gentner, S. I. Fried, E. Halgren, S. S. Cash, and S. A. Dayeh, “Selective Formation of Porous Pt Nanorods for Highly Electrochemically Efficient Neural Electrode Interfaces”, Nano Lett. 2019, 19, 9, 6244-6254.

Chapter 5

Ongoing and Future Work

5.1 Scalability to 1024 Channel Arrays

This research work aimed to continuously scale the arrays developed and discussed in Chapter 3 which is significant for mapping activities in large extended neuronal networks and cardiomyocyte tissue. A 1024 individually addressable nanowire array platform is under-development in our laboratory. This platform constitutes a 32×32 nanowire array distributed in the area of 1.5 mm × 1.5 mm with 50 µm pitch between the nanowires, where the electrode leads are patterned with 3 µm spacing and placed in between the nanowires. The overview of the 1024 channel nanowire array platform is shown in **Figure 5.1**.

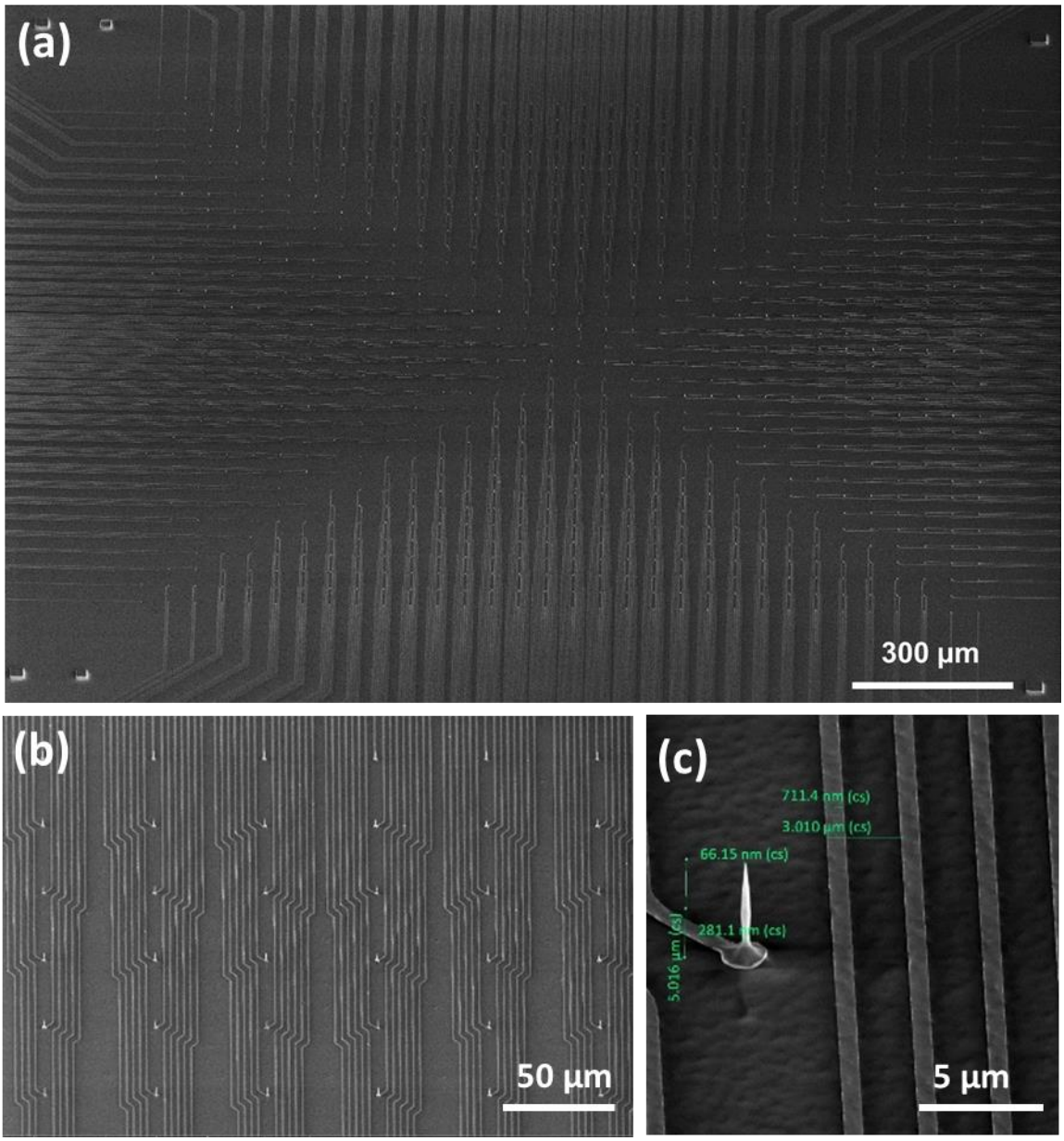

Figure 5.1 1024 channels nanowire array platform. (a) Overview of the SEM image of the 32×32 individually addressable nanowire array. (b) SEM image of the high density leads and individually addressable nanowire array. (c) Zoomed in SEM image of a single nanowire and the nearby electrode leads.

5.2 High-Density Depth Probe Devices

We developed the fabrication process for high-density depth probe devices for clinical applications, which can be used to localize normal and aberrant activity in subcortical layers of the brain. The sensor tip was integrated 128 contact channels in a shank with 1.5mm length and 230 µm width. (d) The tip of the shank is about 30 µm wide and each sensor dot has a diameter of 10 µm.

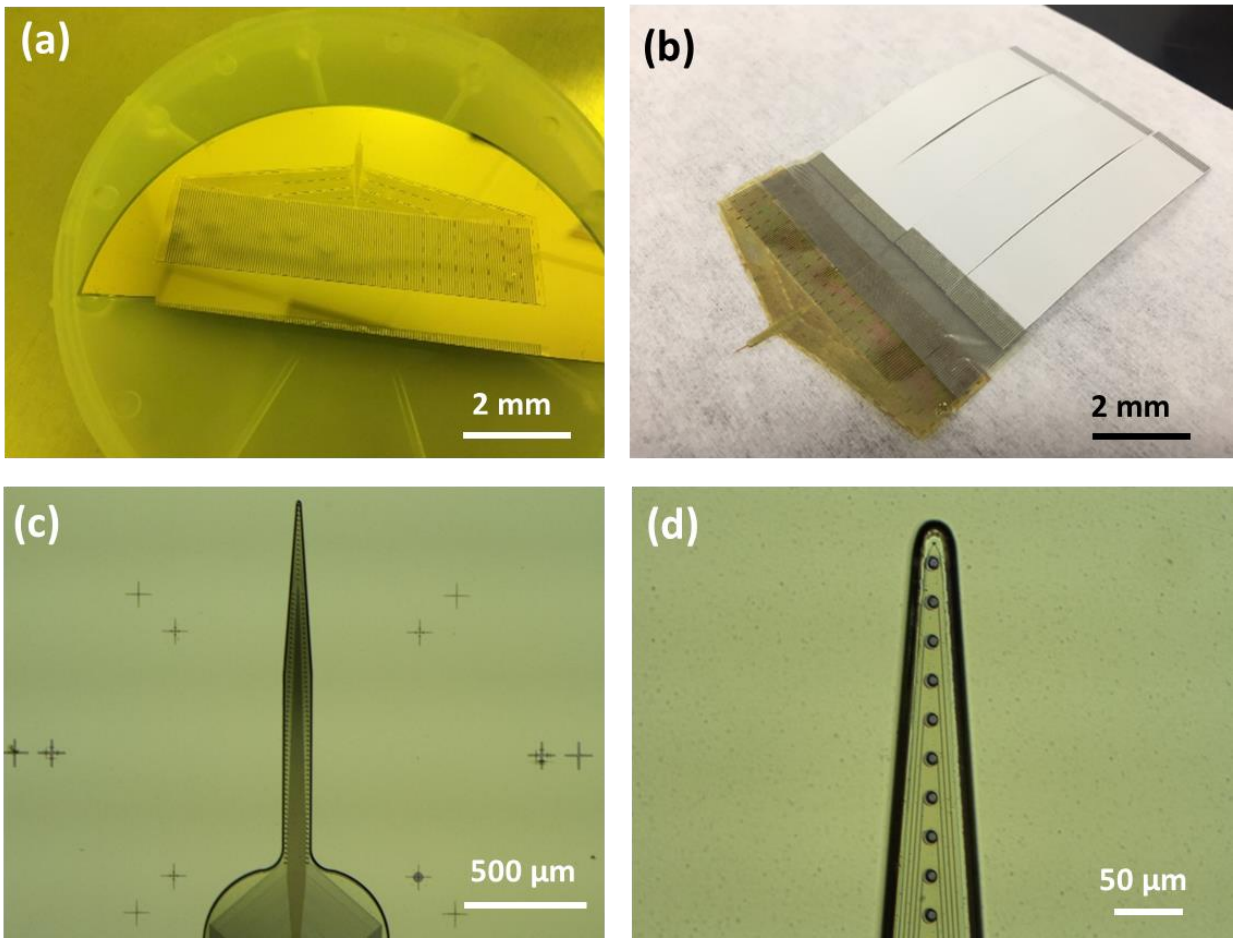

Figure 5.2 High Density Depth Probe Devices: (a) Overview of the devices before it is released from the Si substrate. (b) Overview of the devices after it is released from the Si substrate and bonded to the ribbon cables. (c) The sensor tip integrated 128 channels of the shank with 1.5mm length and 230 µm width. (d) The tip of the shank is about 30 µm width and each sensor dot has the diameter of 10 µm.

5.3 Large Scale Integration of Nanowires and CMOS Chip

The method to integrate nanowire to CMOS chip that we introduced in Chapter 4 utilized Focused Ion Beam, which is not conveniently scalable. Deposition of each nanowire lasts 10-30 mins to be grown on the chip, each chip needs at least 43 hours with 256 nanowires. To develop an efficient way for the integration of nanowires to the CMOS chip, it is important to utilize a different and more efficient integration scheme. The method of Ni-Si bonding that we introduced in Chapter 2 provides a possible solution, where Ni-Si reaction time starts from 295 ℃, which is lower than the CMOS chip's tolerant temperature of up to 400 ℃. Ni-Si bonding provides us a CMOS compatible way to integrate the nanowire to the CMOS chip. This method is currently in pursual in our laboratory.

5.4 Electrofluidic Neuronal Interfaces

This project aimed at developing arrays of nano-fluidic probes for simultaneous nano-fluidic drug delivery [1-4] and electrophysiological measurements [5-10] on a sub-cellular. We utilized advanced hybrid integration and nanolithography techniques to build arrays of nano-fluidic probes atop microfluidic channels with an intermediate metal electrode layer that is of similar diameter to the nano-fluidic probe, and that is suitable for individual electrical addressability. In addition to mapping of cellular activity in networks of cells [11-14], for instance neurons, at different spatiotemporal resolutions, our platform will enable the localization and isolation of cellular molecular events and fluidic intervention [15-17], simultaneously, which is not possible otherwise at such sub-cellular scale. This platform can enable multimodal measurements including monitoring activity of Ca^{2+} currents through fluorescence imaging and the electrophysiological recording of the network activity. While this can be traditionally achieved through a combination of Ca^{2+} imaging and patch-clamp, the scalability to large networks of

neurons and the longitudinal measurements over long durations of time is not possible, our platform will break this barrier. Earlier work demonstrated several forms of micro-fluidic and nanowire probes for probing neuronal activities including IrO_2 nanotubes, [11] Al_2O_3 nanostraws, [3, 4] and SiO_2 nanotubes. [12] Overall, these efforts are promising and have demonstrated that one can perform, despite independently, intracellular recordings and manipulation with microfluidics. A greater challenge is posed in performing the simultaneous biochemical intervention and electrophysiology in arrayed scalable devices to interface with networks of neurons. Our platform will provide such capabilities.

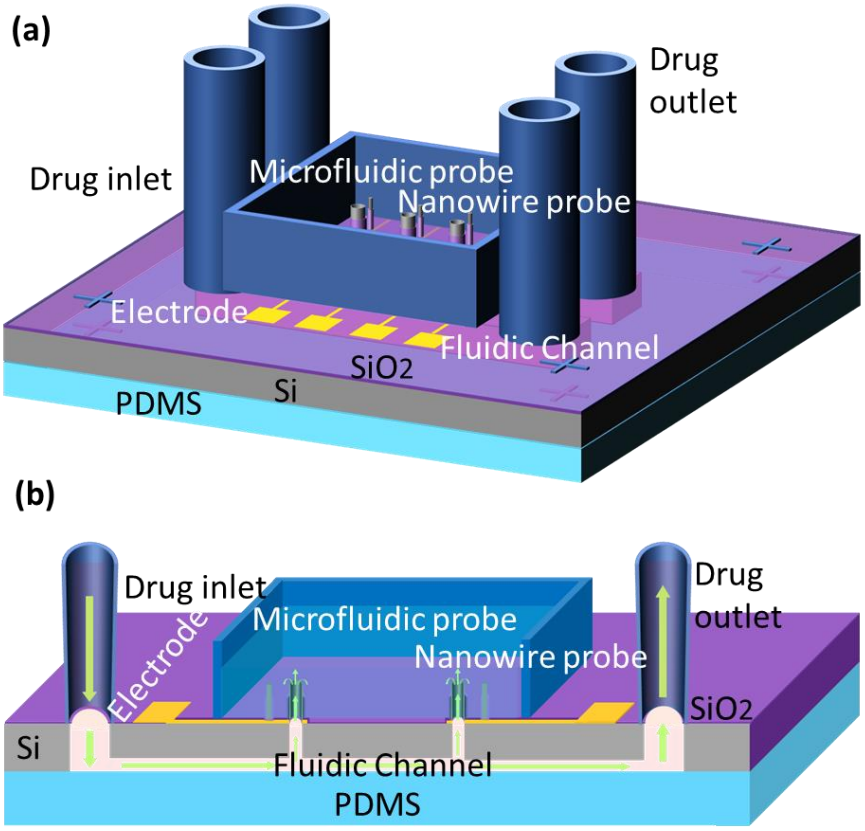

Figure 5.3 Schematic illustration of Electro-nanofluidic channels device. (a) overview of our device, (b) cross-section of our device.

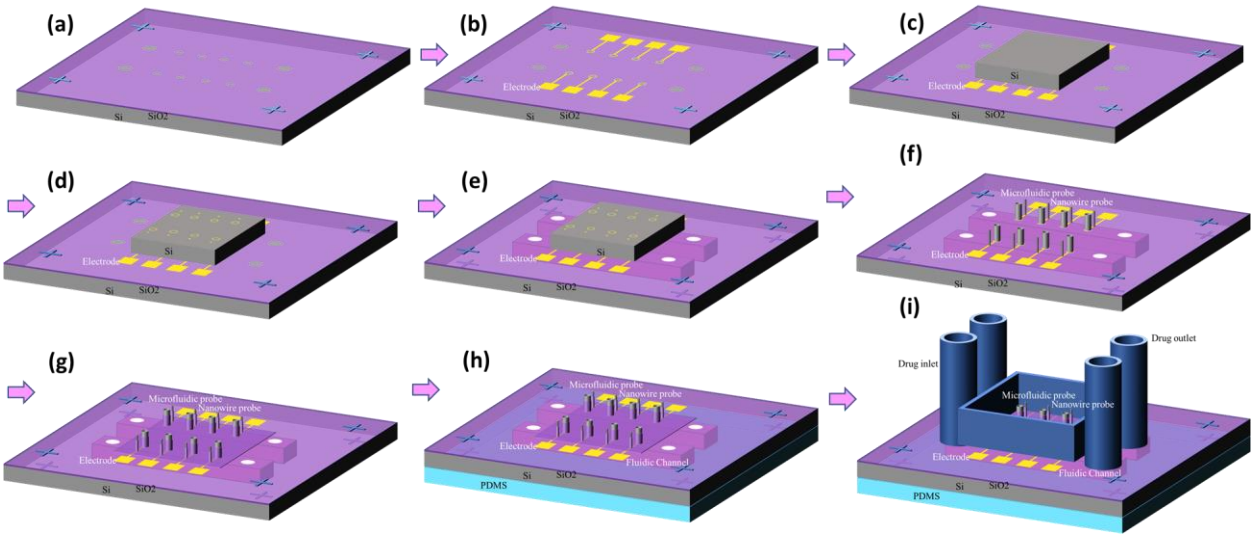

Figure 5.4 Process flow for the formation of electro-microfluidic channels on Si. (a) ICP dry etching through the SiO2 layer to get the SiO2 holes. (b) Photolithography/ EBL/ Electron beam evaporation to make the electrodes pattern, which are well aligned to the SiO2 holes. (c) Bond the device with a thin piece of Si. (d) EBL/ Electron beam evaporation to make the nano-dots and micro-rings on top of Si. (e) Photolithography of SU8 to make back-side channel pattern followed by Bosch etching of exposed Si to realize the backside channels. (f) ICP dry etch top-side Si to obtain nanowires and microtubes. (g) passivate the surface with SiO2 and expose the tip of nanowires and microtubes for cell electrophysiological signal detection and drug delivery. (h) Bond the device with PDMS substrate to seal the backside channels. (i) Bond inlet microtubes, outlet microtubes and cell culture ring on top of our device.

We depicted our device concept in **Figure 5.3** (a) with a cross-sectional view for clarity shown in **Figure 5.3** (b). In this demonstrative prototype, we fabricated 8 individual microchannels to deliver 8 different drugs, fluorescent dyes, or biological agents and 64 individually addressable nanowires for electrophysiological recording. Each channel connected to 8 individual electrodes through embedded nano-fluidic probe. Therefore, 64 electrically isolated and addressable micro-fluidic probes and 64 individually addressable nanowires in total were fabricated, each connecting to its independent electrode lead. The dimensions of our prototype device are about 18mm × 18mm without pushing to the limits of our nanoscale lithography and microfluidic channel fabrication.

Because our process is devised based on standard semiconductor manufacturing techniques, our device is highly scalable with potential to achieve ~ 2,000 chips per 4-inch wafer, which will be a dramatic improvement in throughput of drug screening devices, as an example, while enhancing their capabilities in the detection efficiency at cellular or sub-cellular levels in biological and clinical research.

Fabrication of the electrofluidic neuronal devices was based on a 200 μm width double-side polished Si wafer, with 2 μm thick thermally grown SiO_2 layer on one side of the wafer. In the first step, we patterned the nano-dots for nanowire probes and micro-dots for microfluidic channel inlets and outlets by electron-beam lithography (EBL). This were followed by a dry etch through the SiO_2 layer to get SiO_2 holes as shown in **Figure 5.4** (a). Secondly, we used photolithography/EBL to pattern the electrodes followed by metal deposition as shown in **Figure 5.4** (b), which should be aligned with the nano-dots and micro-dots of SiO_2. These electrodes contain four layers of metals (30nm Ti/ 200nm Ni/ 50nm Ti/ 200nm Ni for adhesion/ conduction/ diffusion-barrier/ silicidation purposes, respectively) [18]. Thirdly, we bonded a 50μm thin Si sample in the center region of the devices as schematically illustrated in **Figure 5.4** (c). Fourthly, we used EBL to pattern the nano-dots and micro-rings on top of Si, which aligned with the electrode dots and SiO_2 hole underneath the Si as shown in **Figure 5.4** (d). Fifthly, we used photolithography to pattern backside channels, followed by Bosch Si etch in order to realize the microfluidic channels at the back as shown in **Figure 5.4** (e). Sixthly, we etched the nanowires and microtubes from top-side as shown in **Figure 5.4** (f). Seventhly, we passivated the surface but exposed the tip of the nanowires for cell signal detection as shown in **Figure 5.4** (g). Eighthly, we bonded the device to a PDMS substrate to seal the backside channel as shown in **Figure 5.4** (h).

Finally, we bonded the outlet micro-tubes and cell culture ring on top of the device as shown in **Figure 5.4** (i).

Firstly, the backside channel etching modification were shown in **Figure 5.5**. Originally, we used Ni metal mask to define regions where microfluidic channels in the 'back' surface of the Si substrates would be created. But after Si deep reactive ion etching of the channels, the removal of such a mask layer can compromise the surface-micromachined nanoscale sensors. Therefore, I resorted to the use of a chemically resistive polymer etch-mask (SU8) that is also photolithography-definable. Then, utilizing an etch/passivate Si etching process (Bosch etching), the backside channel is formed as shown in the **Figure 5.5**. The thickness of the SU8-10 layer was ~13μm. It is thick enough to serve as the dry etching mask for etching through the 200μm Si wafer and to reach the SiO_2 surface layer that separates the top of the device from the back microfluidic channels.

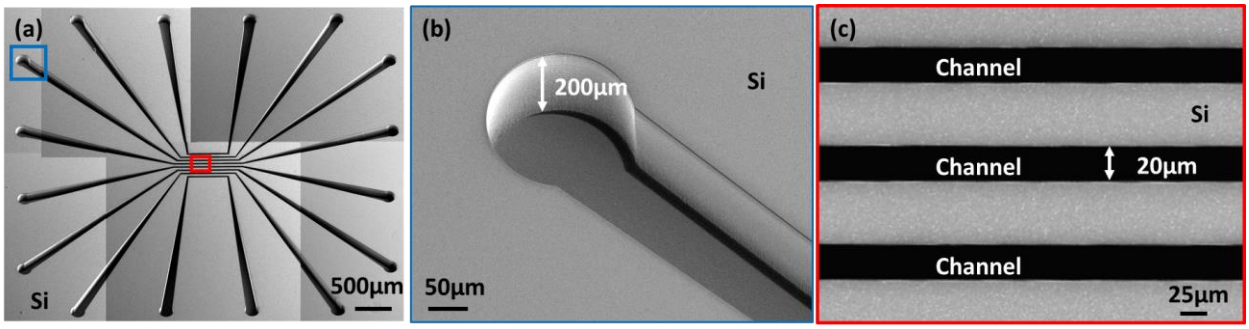

Figure 5.5 SEM images of the backside channel (a) overview, (b) and (c) are the end and the center of the channel for the highlighted blue and red squares in panel (a), respectively.

Secondly, in order to connect the backside channel and top side cylinders, the multimodal probe, SiO_2 at the center region of the channel were required to be etched through, which should be well aligned with the top side cylinder and dots. Etching through the thick SiO_2 layer has proven to be problematic because the etching mask could not resist the fluorine based etch (CF4 (45sccm) and Ar (5sccm)) of the 2.5μm thick SiO_2 layer. Initially, I used typical etching masks like Poly(methyl methacrylate) (PMMA), photoresist, and Ni but none of them was strong enough during the dry etching. Since the hard mask cannot protect the surface totally, it caused some undesired damage in the SiO_2 layer during the dry etching step, which will influence the device quality in the following step. Some of these undesired effects include surface roughness that compromises the forthcoming bonding step, or the creation of small holes in the SiO_2 in the channel region away from the cylindrical outlet region that can cause the leakage of drugs during the measurement period. Additionally, the backside channel etching always left around 1μm Si that cannot be etched thoroughly during the channel etching as shown in **Figure 5.6**. In order to get a stable and repeatable method, I finally used SU8-10 as the etching mask. This hard mask can tolerate the whole SiO_2 etching as well as the etching of 2 ~ 3μm of the underlying Si substrate, the layer which I could not etch from the back as was described in **Figure 5.6** (d). Since the thickness of SU8 10 is 13 μm, the minimum diameter of SiO_2 hole pattern is pushed to 11 μm. Although the diameter of the SiO_2 hole is increased, which corresponds to ~13-15μm diameter mirco-tube above it, we still can do intracellular measurement with nanowire and drug delivery with the microfluidic channel at same time.

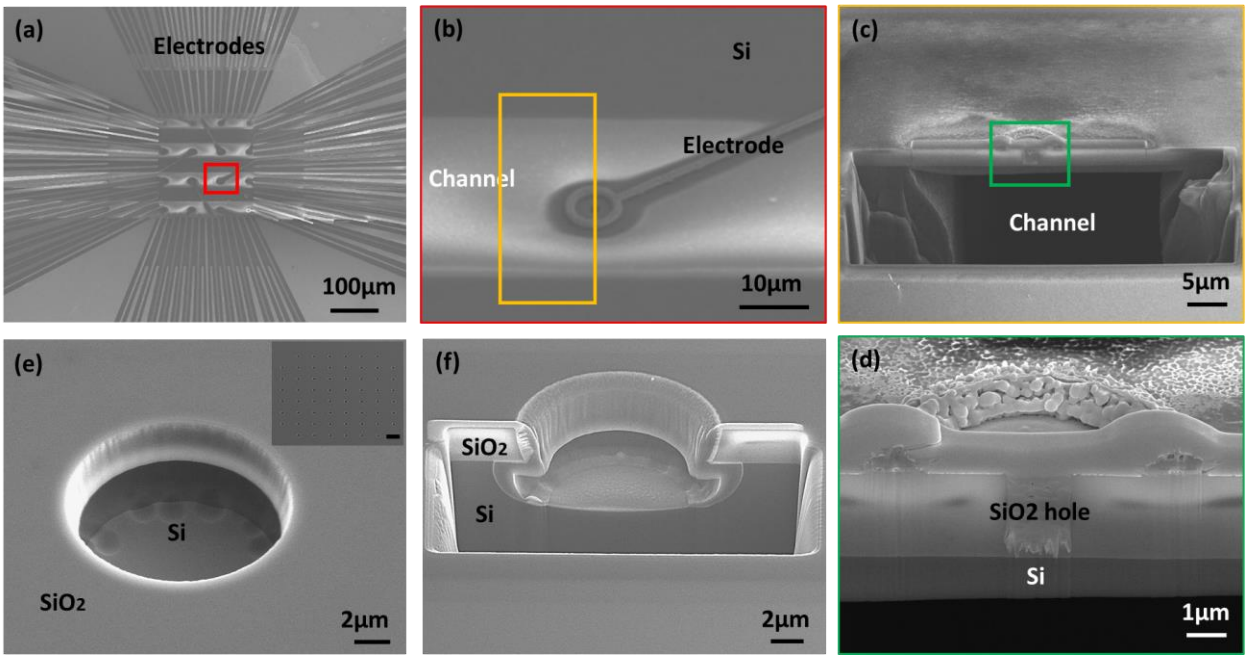

Figure 5.6 SEM images to characterize the hole creation in the SiO2 layer (a) overview of electrode leads and SiO_2 holes, (b) single electrode lead and SiO_2 hole for the red-square marked region in (a), (c) FIB cross-section of channel, aligned well with electrode lead and SiO_2 hole for orange-colored square in (b), (d) the zoom-in image of the green-colored square region in (c). (e) and (f) are the overview and FIB cross-section of SiO_2 for the drying etching result with an optimized SU8 mask.

The lithography alignment is modified as shown in **Figure 5.7**. Since I used photolithography method to make SiO_2 hole pattern and electron-beam lithography (EBL) to make the center electrodes underneath the microfluidic channels, even if we used the same set of markers for the alignment, the misalignment between different layers continues to occur because of the photolithography accuracy limitation as shown in **Figure 5.7** (b). To solve the problem, we fabricated markers in the same etching step of the SiO2 hole pattern. Afterwards, the definition of the electrodes leads pattern by EBL was very well aligned to the markers as shown in **Figure 5.7** (c), the alignment accuracy of the two layers of the pattern depends on the EBL alignment accuracy, which can be pushed to a few nm.

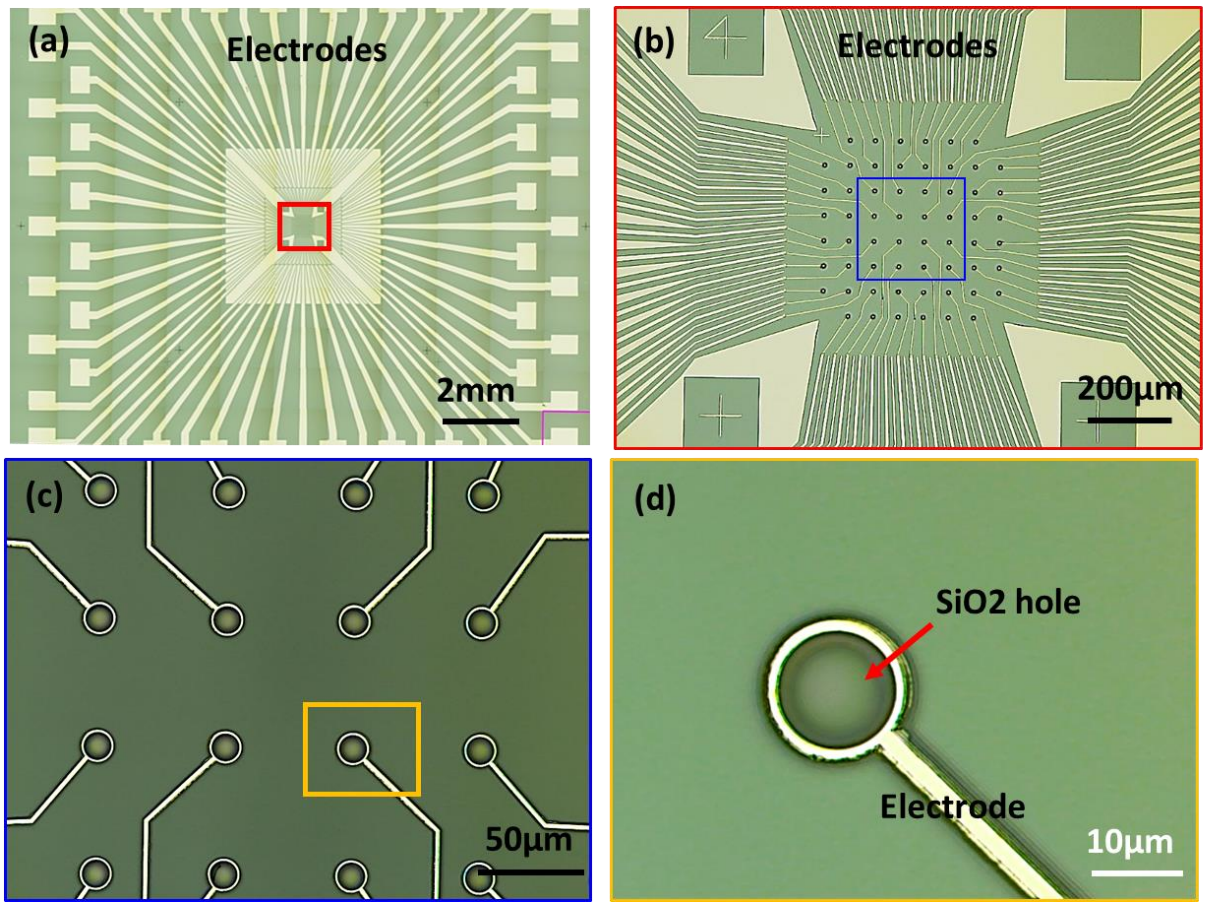

Figure 5.7 Optical microscope images of electrodes and SiO_2 holes (a) overview of Electrode leads and SiO_2 holes, (b) electrode leads cannot align well to the SiO_2 hole since the photolithography accuracy limitation, (c) electrode leads align well with the SiO_2 hole after improvement.

Finally, the micro-tube etching was optimized in **Figure 5.8**. Different size of microtube etching test has been done to find the optimal diameter for a given height. Since we made intracellular measurements with nanowires that are 9µm high, we studied the microtube etching with a total height of 9µm. Firstly, we pattern a Ni ring mask structure on the substrate, followed by electron-beam evaporation of Ni and lift off. Then, we used dry etching to fabricate the micro-tubes with the inner diameter of 2µm, 3µm, and 4µm, respectively. The results are shown in the **Figure 5.8** (a)-(c). By using Focused Ion Beam (FIB) milling, we got the cross-section SEM

images in the **Figure 5.8** (d)-(f), in which we can observe that smaller diameter microtubes etch less than larger diameter ones. We predict that the Si inside of a microtube with inner diameter of 11μm can be etched thoroughly for the future work.

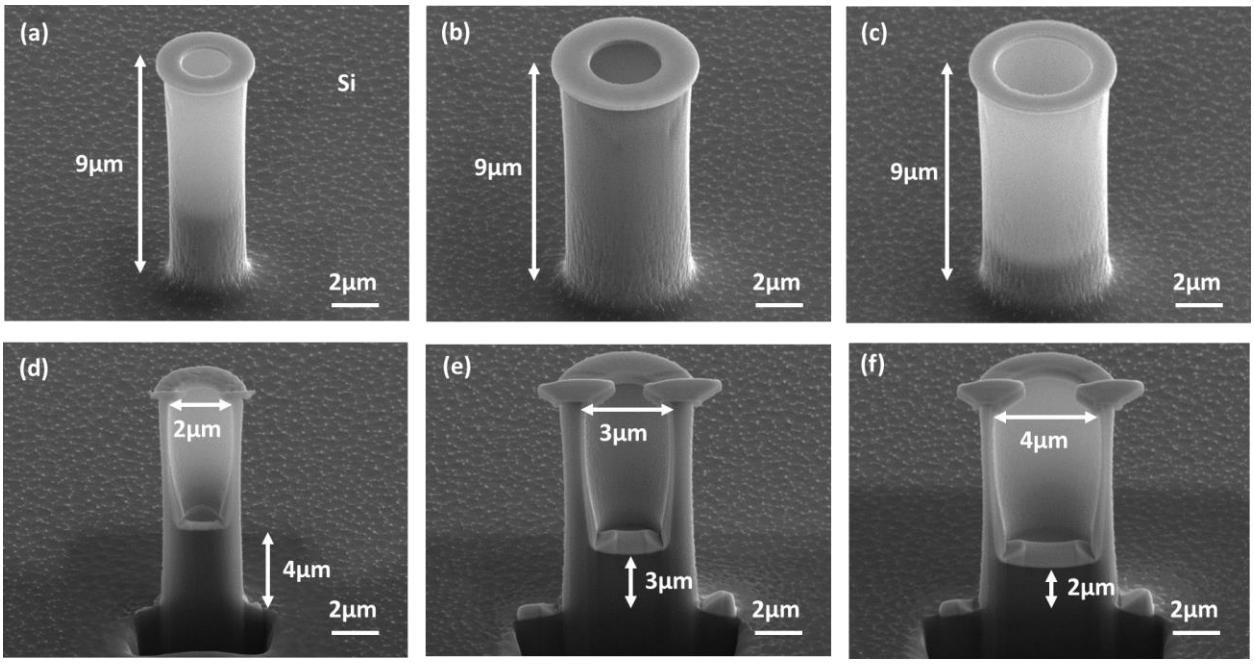

Figure 5.8 SEM images of microtube etching. (a), (b), and (c) are the SEM images of micro-tube with 2μm, 3μm and 4μm inner diameter, respectively. (d), (e), and (f) are the SEM images of FIB cross-section of microtube with 2μm, 3μm and 4μm inner diameter, respectively.

5.5 References

1. X. Xie, A. M. Xu, S. Leal-Ortiz, Y. Cao, C. C. Garner, and N. A. Melosh, “Nanostraw-Electroporation System for Highly Efficient Intracellular Delivery and Tansfection,” ACS Nano 7, 4351, 2013.

2. J. J. VanDersarl, A. M. Xu, and N. A. Melosh, “Nanostraws for Direct Fluidic Intracellular Access,” Nano Lett. 12, 3881, 2012.

3. K. Seidl, S. Spieth, S. Herwik, J. Steigert, R. Zengerle, O. Paul, and P. Ruther. "In-plane silicon probes for simultaneous neural recording and drug delivery." J. Micromech. Microeng. 20, 105006, 2010.

4. S. Metz, A. Bertsch, D. Bertrand, and Ph. Renaud. "Flexible polyimide probes with microelectrodes and embedded microfluidic channels for simultaneous drug delivery and multi-channel monitoring of bioelectric activity." Biosensors and bioelectronics 19, no. 10 (2004): 1309-1318.

5. A. L. Hodgkin and A. F. Huxley, “Action Potentials Recorded from Inside a Nerve Fibre,” Nature 144, 710-711, 1939.

6. E. Neher, and B. Sakman, “Single Channel Currents Recorded from Membrane of Deervated Frog Muscle Fibers,” Nature 260, 799-- ‑ -802, 1976.

7. B. Englitz, S. V. David, M. D. Sorenson, and S. A. Shamma, “MANTA – An Open-Source, High Density Electrophysiology Recording Suite for MATLAB,” Frontiers in Neural Circuits 7, 69, 2013.

8. M. E. Spira and A. Hai, “Multi-electrode Array Technologies for Neuroscience and Cardiology,” Nature Nanotechnol. 8, 83–94 (2013).

9. S. Takeuchi, T. Suzuki, K. Mabuchi, and H. Fujita. "3D flexible multichannel neural probe array." J. Micromech. Microeng. 14 104–107, 2004

10. L. Gallentoft, L. M. E. Pettersson, N. Danielsen, J. Schouenborg, C. N. Prinz, and C. E. Linsmeier, “Size-Dependent Long-Term Tissue Response to Biostable Nanowires in the Brain,” Biomaterials 42, 172, 2015.

11. Z. C. Lin, C. Xie, Y. Osakada, Y. Cui, and B. Cui, “Iridium Oxide Nanotube Electrodes for Sensitive and Prolonged Intracellular Measurement of Action Potentials,” Nature Comm. 5, 3206, 2013.

12. X. Duan, R. Gao, P. Xie, T. Cohen-Karni, Q. Qing, H. Sung Choe, B. Tian, X. Jiang, and C. M. Lieber, “Intracellular Recordings of Action Potentials by an Extracellular Nanoscale Field-Effect Transistors,” Nat. Nano 7, 174-179, 2012.

13. C. Xie, Z. Lin, L. Hanson, Y. Cui, and B. Cui, “Intracellular Recording of Action Potentials by Nanopillar Electroporation,” Nature Nanotech. 7, 185-190, 2012.

14. J. T. Robinson, M. Jorgolli, A. K. Shalek, M. H. Yoon, R. S. Gertner, and H. Park, “Vertical nanowire Electrode Arrays as Scalable Platform for Intracellular Interfacing to Neuronal Circuits,” Nature Nanotech. 7,180-184, 2012.

15. H.-C. Yeh, J. Sharma, J. J. Han, J. S. Martinez, and J. H. Werner. "A DNA− Silver nanocluster probe that fluoresces upon hybridization." Nano letters 10, 8, 3106-3110, 2010

16. H.-C. Yeh, J. Sharma, Ie-M. Shih, D. M. Vu, J. S. Martinez, and J. H. Werner. "A fluorescence light-up Ag nanocluster probe that discriminates single-nucleotide variants by emission color."JACS 134, no. 28 (2012): 11550-11558.

17. M. L. Neidig, J. Sharma, H.-C. Yeh, J. S. Martinez, S. D. Conradson, and A. P. Shreve. "Ag K-edge EXAFS analysis of DNA-templated fluorescent silver nanoclusters: insight into the structural origins of emission tuning by DNA sequence variations." JACS 133, no. 31 (2011): 11837-11839.

18. S. A. Dayeh, R. Chen, R. Liu, A. T. E. Youssef, S. Heon Lee, S. Hinckley, M. L. Khraiche, J. Scott, Y.Hwang, A. Tanaka, Y. G. Ro, A. K. Matsushita, X. Dai, C. Soci, S. Biesmans, A. James, J. Nogan, K. L. Jungjohann, D. V. Pete, Y. Zou, and A. Bang, “Intracellular Recordings of Sub-threshold Potentials by Nanowire Arrays in Human Stem Cell Derived Neurons,” submitted for publication, 2016.

Appendix

MATLAB Scripts for Neuronal Signal Process

A.1 Neuronal Activity Plot

```
% Run read_Intan_RHS2000_file.m and load the saved rhs file before run this
% code


time = t.'; % for time plot
rearrange = [NaN 30 31 15 14 NaN;2 1 0 16 17 18;NaN 28 29 13 12 19;4 27 26 10 11 20; 5 25 24
8 9 21;NaN 6 7 23 22 NaN];
% information of electrode locations

FS = amplifier_data.'; % for easy data handling
FS_rearrange = NaN(length(amplifier_data),36); % for easy data handling
FS_rearrange_title = NaN(1,36); % to lable each curve

for i = 1:6
   for j = 1:6
      if (isnan(rearrange(i,j)) == 0)
         FS_rearrange(:,i+(j-1)*6) = FS(:,33+rearrange(i,j)); % rearrange data for stacked plot
         FS_rearrange_title(1,i+(j-1)*6) = rearrange(i,j); % assign lables
      else
         continue;
      end
   end
end


FS_movie = NaN(length(amplifier_data),6,6); % generate a frame array
for k = 1:length(amplifier_data)
   for i = 1:6
      for j = 1:6
         if (isnan(rearrange(i,j)) == 0)
```

```
            FS_movie(k,i,j) = FS(k,33+rearrange(i,j));
        else
            continue;
        end
    end
  end
end


fig1 = figure; % line plot with actual electrode locations
for i = 1:6
  subplot(1,6,i);
  stackedplot(time,FS_rearrange(:,(i-1)*6+1:(i-
1)*6+6),'DisplayLabels',num2cell(FS_rearrange_title(:,(i-1)*6+1:(i-1)*6+6)));
end

fig2 = figure; % two-column plot with columns in series
for i = 1:2
  subplot(1,2,i);
  stackedplot(time,FS_rearrange(:,(i-1)*18+1:(i-
1)*18+18),'DisplayLabels',num2cell(FS_rearrange_title(:,(i-1)*18+1:(i-1)*18+18)));
end

% for two-column plot with rows in series
for i = 1:6
  for j = 1:6
    newindex(1,(i-1)*6+j) = (j-1)*6+i;
  end
end

fig3 = figure; % two-column plot with rows in series
for i = 1:2
  subplot(1,2,i);
  stackedplot(time,FS_rearrange(:,[newindex(1,(i-1)*18+1:(i-
1)*18+18)]),'DisplayLabels',num2cell(FS_rearrange_title(:,[newindex(1,(i-1)*18+1:(i-
1)*18+18)])));
end

% change colormap to paint same color at every 6 curves
co = [  0   0.4470   0.7410;  0.8500   0.3250   0.0980;  0.9290   0.6940   0.1250;  0.4940
0.1840   0.5560;  0.4660   0.6740   0.1880;  0.3010   0.7450   0.9330];
set(groot,'defaultAxesColorOrder',co)

% assign offset
for i = 1:36
  FS_rearrange_offset(:,i) = FS_rearrange(:,newindex(i))+(i-1)*5000;
```

```
end

% single column plot with offset
fig4 = figure;
plot(time, FS_rearrange_offset(:,1:36));
xlim([time(1,1) time(end,1)]);
ylim([0 175000]);


% Run until here to avoid delay from video
%--------------------------------------------------------------------------


% for contour animation
x = [-2.5:1:2.5];
y = [2.5:-1:-2.5];
[X,Y] = meshgrid(x,y);

% down sample frames for faster video play
downsamplerate = 1000;

for i = 1:6
   for j = 1:6
      FS_movie_normal(:,i,j) = normalize(FS_movie(:,i,j))*5000;
   end
end


FS_movie_downsampled = FS_movie_normal([1:downsamplerate:length(amplifier_data)],:,:);
levels = [-5000:200:5000]; % assign values for contour lines

% Contour plot video
fig5 = figure;
[C, h] = contourf(X,Y,squeeze(FS_movie_downsampled(i,:,:)), levels);
set(h,'LineColor','none');
caxis([-5000 5000]);
colormap(jet)
colorbar;
pause(10); % delay to prepare video capture
for i = 1:round(length(amplifier_data)/downsamplerate)
   h.ZData = squeeze(FS_movie_downsampled(i,:,:))
   refreshdata
   pause(0.00001);
end
% the video will run until it reaches the end of the data
% to force stop the video press ctrl + c multiple times
```

```
% Contour plot video end
% ------------------------------------------------------------------

% Contour plot video with higher interpolation(10 times higher)
% calculate the high resolution interpolated matrix
xq = [-2.5:0.1:2.5];
yq = [2.5:-0.1:-2.5];
[XQ, YQ] = meshgrid(xq, yq);

%
for i = 1:round(length(amplifier_data)/downsamplerate)
   FSQ(i,:,:) = interp2(X,Y,(squeeze(FS_movie_downsampled(i,:,:))),XQ,YQ,'linear');
end
%

%Play video with higher interpolation (smooth curves)
fig6 = figure;
[C, h] = contourf(XQ,YQ,squeeze(FSQ(1,:,:)),levels);
set(h,'LineColor','none');
caxis([-5000 5000]);
colormap(jet)
colorbar;
pause(10); % delay to prepare video capture
for i = 1:round(length(amplifier_data)/downsamplerate)
   h.ZData = squeeze(FSQ(i,:,:));
   refreshdata;
   pause(0.00001);
end

% Contour plot video with high resolution end
% ------------------------------------------------------------------
```

A.2 Deconvolution of Neuronal Signal

```
% 1) GIVEN input, TF --> output
% 2) GIVEN input, output --> TF* (estimated)
% 3) GIVEN output, TF* --> input* (estimated) = DECONVOLUTION
% 4) GIVEN compare input vs input*

%% 1) input, TF --> output
%=================================================================
=======
```

```
% sampling time (time between samples)
Fs=24414.06;
dt=1/Fs;

% Reading data from TDT
% res= sev_quick_read('C:\Path\file.sev','single');
% time=[0:dt:(length(res)-1)*dt];
% plot(time,res)

% TF = Transfer Function Calcualtion
% time constant
RC=0.2;
% expresstion in frequency domain
H=tf([1/RC],[1 1/RC]);

% INPUT = Generate square test signal
[u,t] = gensig('square',3,10,dt);

% get OUTPUT = Simulate the system response to the test signal
lsim(H,u,t)
% save the ouput response into a vector
y=lsim(H,u,t);

%% 2) input, output --> TF* (estimated)
%=================================================================
% Transfer Function (system response) Estimation [given input&output time vectors]
% create "iddata" object for a time-series data containing both in/out data
data=iddata(double(y),u,dt);
sys_est = tfest(data,1)

% convert the resulted/estimated expression into "mathimatical" expression
% define symbols of the expression
syms s t1
TF = (1/RC)/(s + (1/RC)); % Example for Low Pass Filter transfer function
% evalute the time expression by performing inverse laplace transform (s-domian to time-domain
conversion)
ilaplace(TF, t1)
%% 3) output, TF* --> input* (estimated) = DECONVOLUTION
%=================================================================
% tf=2*exp(-2*t);
% this step needs to be written MANUALLY (upon evaluting "ilaplace")
tf=5*exp(-5*t);
% perform the deconvoltuion process in time domain
x=deconv([y; zeros(length(y)-1,1)],tf)*sum(tf);
%% 4) compare input vs input*
%=================================================================
```

```
figure
plot(t,u,'b','LineWidth',2.0)
hold all
plot(t,x,'--r','LineWidth',2.0)
xlabel 'time'
ylabel 'amplitude'
title 'results comparsion'
legend 'input' 'estimated input'
set(gca,'fontsize', 15)
%% END ========================================================
```